Effect of clogged drainage pipes on the stability of railway embankments

Shuyue Wang

A Thesis

In

The Department

of

Building, Civil, and Environmental Engineering

Presented in Partial Fulfillment of the Requirements

for the Degree of Master of Applied Science (Geotechnical Engineering) at

Concordia University

Montréal, Québec, Canada

June 2022

© Shuyue Wang, 2022

CONCORDIA UNIVERSITY

School of Graduate Studies

This is to certify that the thesis prepared

By: Shuyue Wang

Entitled: Effect of clogged drainage pipes on the stability of railway embankments

and submitted in partial fulfillment of the requirements for the degree of

Master of Applied Science (Geotechnical Engineering)

complies with the regulations of the University and meets the accepted standards with respect to originality and quality.

Signed by the final Examining Committee:

Chair and Examiner

Dr. C. Alecsandru

Examiner

Dr. C. Alecsandru

Examiner

Dr. B. Li

Supervisor

Dr. A. M. Zsaki

Approved by: _____

Dr. A. Bagchi Chair of the Department

_____ 2022 _____

Dr. M. Debbabi Dean of Faculty

ABSTRACT

Effect of clogged drainage pipes on the stability of railway embankments

Shuyue Wang

The rising water level caused by clogged drainage pipes results in instability in railway embankments and creates dangerous riding conditions for passing trains. As such, it is crucial to identify the factors that influence the slope stability of railway embankments subjected to rising water levels and exposed to train traffic. The purpose of this thesis is to study the slope stability of railway embankments by using a coupled Biot model where pore water pressure and stresses are considered simultaneously. Slope stability analyses are performed using two-dimensional finite element shear strength reduction (FE-SSR) models in which the control variable method is employed to study the effect of key parameters (e.g., embankment geometry, water level, and train speed) on the stability of railway embankments. Maximum safe train speeds are calculated for various slope geometries and water levels to maintain a minimum factor of safety of 1.3.

The simulation results illustrate that a flatter slope with a slope ratio of 1V:3H, 3m railway embankment and the 1m natural slope presents the best result in maximum safe train speed. Consequently, a model is developed to evaluate the influence of compromised drainage on the slope stability of a railway embankment under stationary or moving train loads. The findings of this study are then used to determine desirable slope geometry parameters and maximum safe train speeds for railway embankments subjected to rising water levels.

ACKNOWLEDGEMENT

First and foremost, I would like to express my gratitude to my supervisor, Dr. Attila Michael Zsaki, for providing me this opportunity to join his group. His inspiring guidance and consistent support helped me to become an independent researcher.

I also want to record my deepest appreciation to my parents, who always love me unselfishly and support me consistently and encourage me through many difficult times. My gratitude also extends to my friends, who helped me with their encouragement and company.

Finally, I would like to acknowledge the financial support from my supervisor through the GCS FRS funds to help complete my research work.

Table of Contents

List of Tables

List of Figures

List of Symbols

A	=	bearing area of cross ties (mm^2)
ABP	=	average ballast pressure (psi) or (MPa)
D	=	diameter of wheel (in.) or (mm)
DF	=	distribution factor of axle load carried by a single tie (%)
E	=	Young's modulus (MPa)
E', υ'	=	effective elastic parameters (MPa)
F	=	wheel load (kN)
F_r	=	resultant wheel load (kN)
G	=	shear modulus (MPa)
H	=	initial total head (m)
H_F	=	height of the soil element (m)
H_n, x	=	natural slope height (m)
H_r	=	railway embankment height (m)
H_W	=	depth of water over the soil element (m)
IF	=	impact factor (%)
K	=	stiffness of the spring (N/m)
$[K_E]$	=	element stiffness matrix
$[K_G]$	=	global stiffness matrix
L	=	change in water level or drawdown depth (m)
L_O	=	overall length of railroad car measured over the pulling face of the coupler (m)
N	=	resultant (total) normal force (kN)
N'	=	resultant effective normal force (kN)
P	=	applied load (kN)
R	=	drawdown rate (m/day)
R_F	=	rate of FS change
S	=	degree of saturation (%)
S_I	=	inboard axle spacing (m)
S_O	=	outboard axle spacing (m)
S_T	=	truck axle spacing (m)

T	=	resultant shear force (kN)
TC	=	length between the center pin on the trucks (m)
U	=	displacement (m)
V	=	train speed (km/h) or (mi/h)
X	=	width of the soil element (m)
c	=	cohesion (kPa)
c_h	=	coefficient of consolidation in the horizontal direction (cm^2/s)
c_v	=	coefficient of consolidation in the vertical direction (cm^2/s)
h	=	total head (m)
i	=	angle formed by a horizontal line and the base of the soil element (°)
k_h, k_x	=	horizontal hydraulic conductivity (cm/s)
k_v, k_y	=	vertical hydraulic conductivity (cm/s)
m_v	=	coefficient of compressibility (m^2/kN)
n	=	porosity
γ	=	unit weight of material (kN/m^3) or (kg/ m^3)
γ_1	=	shear strain
γ_b	=	effective unit weight (kN/m^3)
γ_t	=	total unit weight (kN/m^3)
γ_w	=	unit weight of water (kN/m^3)
s, t	=	subgroup number
t_p	=	time duration of loading pulse (h)
u, u_w	=	pore pressure (kPa)
u^*	=	displacement in x direction (m)
v	=	Poisson's ratio
v^*	=	displacement in y direction (m)
w	=	weight of track substructure per unit area (kg/m^2)
z	=	depth of track substructure (m)
ε	=	strain (m/m)
τ	=	shear strength (kPa)
ϕ	=	angle of internal friction (°)

σ	=	normal stress (kPa)
σ'	=	effective stress (kPa)
σ_{ij}	=	state of stress (kPa)
$\{\Delta d_E\}$	=	vector of incremental element nodal displacements (m)
$\{\Delta d_G\}$	=	vector of all incremental element nodal displacements (m)
$\{\Delta R_E\}$	=	vector of incremental element nodal forces (N)
$\{\Delta R_G\}$	=	vector of all incremental element nodal forces (N)

Chapter 1 Introduction

1.1 Background

The Canadian rail network is a key player in the transportation of goods across the country that is being increasingly strained as a result of an increase in the demand for rail freight transport, lack of expansion of the rail network, and climate change (Transport Canada 2018). The growing volume of goods transported by rail is particularly challenging for the Canadian rail infrastructure given that it was built many decades ago. The Canadian railway system consisted of 42,274 kilometers of track in 2019, as shown in Figure 1.1 (Transport Canada 2019). With more fluctuations in weather patterns and increased mixed precipitation in the winter, adequate drainage of railway tracks is of the utmost importance in ensuring railway embankment stability.

Figure 1.1 The Canadian railway network in 2019 (Transport Canada 2019)

According to the Transportation Safety Board of Canada (TSB), 1244 railway incidents were reported in 2019, up about 6.4% from 2018. These accidents resulted in 72 deaths, which was somewhat lower than the ten-year average (Transport Canada 2019). To enhance transportation

safety, the Transportation Safety Board of Canada (TSB) investigated and reported several accidents involving embankment/roadbed failures, including the following two cases:

1. On April 28, 2013, at around 18:40 Central Standard Time, VIA Rail northbound passenger train No. P69341-28 met a roadbed collapse near Togo, Saskatchewan, at Mile 83.55 on the Canadian National Railway Togo Subdivision. Two locomotives and two lead cars derailed in this collision, and no one got injured. According to a thorough study, the embankment collapsed due to water saturation and pore water pressure build-up in moisture-sensitive fills due to fast snowmelt and poor water drainage due to an ice clog at the culvert outlet. In addition, the excess water head on the leaky drop structure and culvert rivet holes caused an enhanced piezometric surface condition in the embankment, making it more prone to collapse. The ice obstructing the culvert outflow is seen in Figure 1.2.

Figure 1.2 Ice blocking culvert outlet (TSB 2013)

2. At Mile 89.7 of the Kinghorn Subdivision in Orient Bay, Ontario, CN North America's (CN) eastbound freight train No. 336-KP-24 hit a severe roadbed washout and derailed two locomotives and 15 laden cars. As a result of the mishap, three employees were injured. The roadbed of the accident site was built on glaciolacustrine silt and clay layers that become unstable when wet. Water penetration of the glaciolacustrine silts and clays subgrade triggered the derailment, causing the subgrade to become saturated to a greater height than previously

seen. As a result, the track bed became unstable and sank, leaving a wide depression beneath it. Water invaded the subgrade due to a build-up produced by a partially obstructed culvert, as well as possible subsurface low-pressure sources.

Meanwhile, points and signalling equipment rely on intricate wiring and power supplies and are extremely prone to failure when the equipment in the railway embankment might be inundated if water cannot flow out of the track and must be replaced before services can run again. A short circuit can occur if there is a live conductor rail on the track (Palin et al. 2021).

1.2 Research Objectives

Unusual groundwater conditions caused by inadequate drainage can trigger railway embankment failures, and interfere with the signal equipment of railway operations. These events can potentially pose a threat to the structural integrity of railway tracks as well as to the safety of passing trains and their passengers. Therefore, this research aims to identify the effect of the following parameters on the slope stability of railway embankments:

1. embankment geometry,
2. groundwater conditions caused by blocked drainage pipes, and
3. the train velocity.

After performing a parametric study, the results generated in this study are then analyzed to obtain a set of railway embankment geometries as well as maximum allowable train speeds for a given railway slope required to maintain safe riding conditions.

The slope stability of railway embankments is investigated by developing finite element-based Biot coupled models that simultaneously consider pore water pressure and stress.

The detailed objectives of this research project are as follows:

- Determine which of the studied factors affect the stability of railway embankments when the drainage is compromised.
- Investigate how sensitive the embankment stability is to these factors.
- Examine how train speed affects the stability of a railway embankment.
- Identify a set of embankment slope geometric parameters and maximum train speeds to ensure railway embankments remain under stable operational conditions.

1.3 Research Methodology

The methodology devised to conduct this research project consists of the following three steps:

1. Modeling using the Finite element method (FEM) via coupled Biot model simulation, using RS2 (Rocscience Inc., 2019): a basic model is defined by key model variables (such as slope and embankment geometries, groundwater conditions, loads due to different train speeds). Then, using RS2, a parametric analysis of these characteristics impacting slope stability was carried out.

2. Parametric study: The effect of the parameters considered in this study on the slope stability of railway embankments is investigated using finite element modeling. The control variable method is employed in this work. Three sets of models are developed, including:

    1. Set I: Models with Functioning Pipe Drains
    2. Set II: Models under Rising Water Level conditions
    3. Set III: Model under Rising Water Level condition and Locomotive Loading

    The parameters considered in these three model types are composed of:

    a) Variable slope and embankment geometries: embankment height, slope inclination, subgrade height.
    b) Different water level rising ratios (L/H, water level or rising depth is L, and the initial total height is H).
    c) Different train speeds.

3. Data analysis and conclusion drawn: the results obtained in the parametric study for the three model classes are represented graphically to provide insight into the evolution of embankment slope stability under different conditions. A chart relating the maximum allowable train speed to the studied parameters is also developed, which can be used by railway agencies in assessing field conditions.

1.4 Thesis Outline

This thesis consists of five chapters. The current chapter introduces the motivations, scope, and objectives of this project while also describing the methodology used in this study. Chapter 2 provides a thorough review of relevant research works and presents the various numerical methods used in geomechanics to analyze slope stability problems. In Chapter 3, a mesh convergence analysis and validation are conducted to ascertain the accuracy of FEM models and analysis. The three sets of models developed to examine the effect of different water and train loading conditions as well as the results of the parametric study are discussed at length in Chapter 4. Finally, the salient features of this research work, its limitations, and recommendations for future work are outlined in Chapter 5.

1.5 Summary of Contributions

By analyzing the results of the parametric study, this research endeavor provides insight into the stability of railway embankments suffering from inadequate drainage and aims to contribute to safer design practices by providing a set of desirable embankment geometric properties and train speeds to ensure embankment stability.

Chapter 2 Literature Review

2.1 Introduction

The effect of rising water levels on the stability of slopes and dams has received considerable research attention. However, few published works have attempted to study the combined effect of rising water levels and train loading on the slope stability of railway embankments.

This chapter describes how models are developed and how the analysis is performed, which consists of five sections:

- Section 2.2 provides an overview of railway track components, the methods used to calculate moving train loads on the railway track, and the load transmission mechanism.
- Section 2.3 describe how rising water levels impact slope and presents the FEM-based Biot theory.
- Section 2.4 illustrates the process of collecting the main parameters of this model.
- Section 2.5 summarizes several numerical methods used to solve the slope stability problems and details the reasons why the FEM has been selected for this study.
- Section 2.6 describes typical soil constitutive models used in FEM.

2.2 Railway Embankment and Moving Loading on Track

Excess pore water pressures are generated in a railway embankment when it is subjected to moving train loads and may affect the embankment's slope stability. When water cannot flow out of the embankment immediately, excess pore water pressure is induced, which reduces soil strength (Li et al. 2002). Under such conditions, track foundation failure may occur if dynamic train loading is applied to the embankment (Li et al. 2002). This section provides a description of a typical railway embankment and its components and then discusses the nature of railway loading and its associated load transfer mechanisms.

2.2.1 Railway Track Structure

The track is the most fundamental component of the railway infrastructure, and the track supports the rolling stock by distributing wheel loads from track superstructure to track substructure (Figure 2.1) (Li et al. 2002). Two types of rail tracks are commonly used: conventional ballasted track and slab track, as shown in Figure 2.2 (Indraratna et al. 2011; Esveld 2001).

Indraratna et al. (2011) indicated that the slab track is a better option for high-speed and high-intensity traffic lines, has a longer service life, and does not need much maintenance. Ballasted tracks are the most common type of railway embankment structure in North America, and they are easy to design and construct (Lichtberger 2005). Furthermore, the construction material can be obtained from domestic sources (timber) (Li et al. 2016). In comparison, the initial construction cost of a ballasted track is much lower than that of a slab track, which is the main reason why slab tracks are not as widely used. However, a ballasted track tends to deteriorate with the increasing passage of train traffic (Esveld 2001). Ballasted railway tracks are considered in this study since they are commonly used in North America.

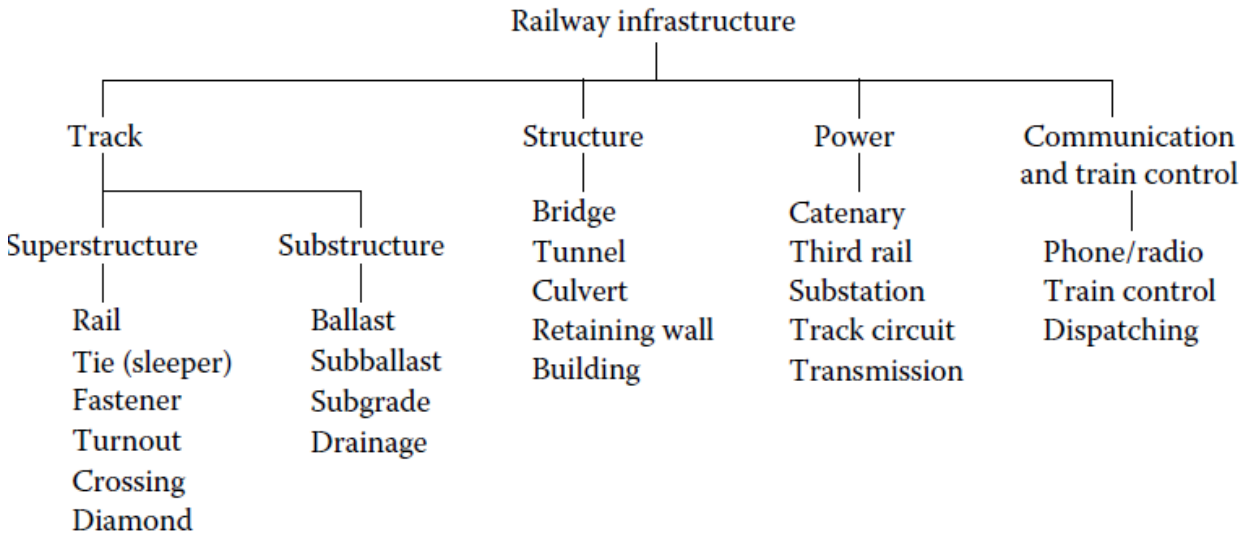

Figure 2.1 Elements of railway infrastructure (Li e al. 2002)

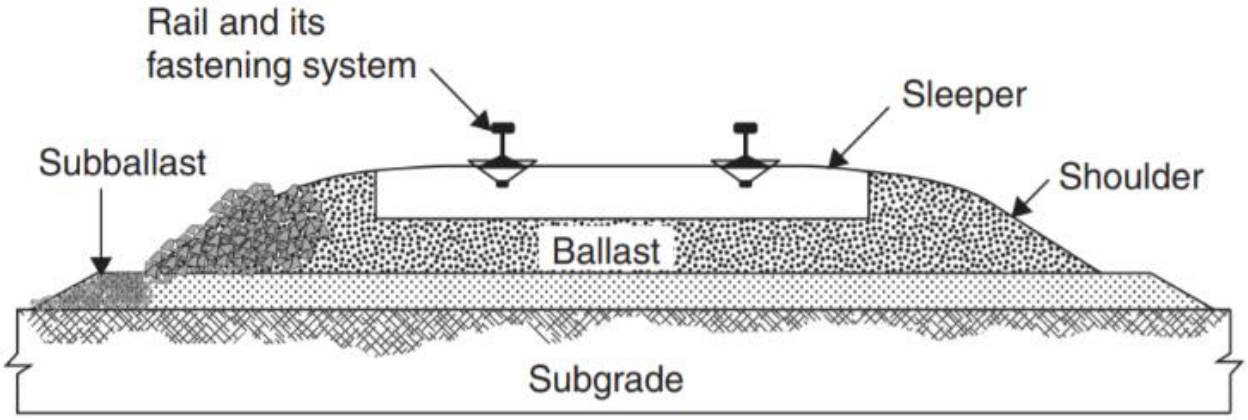

(a) Cross-section of a ballasted rail track (Indraratna et al. 2011)

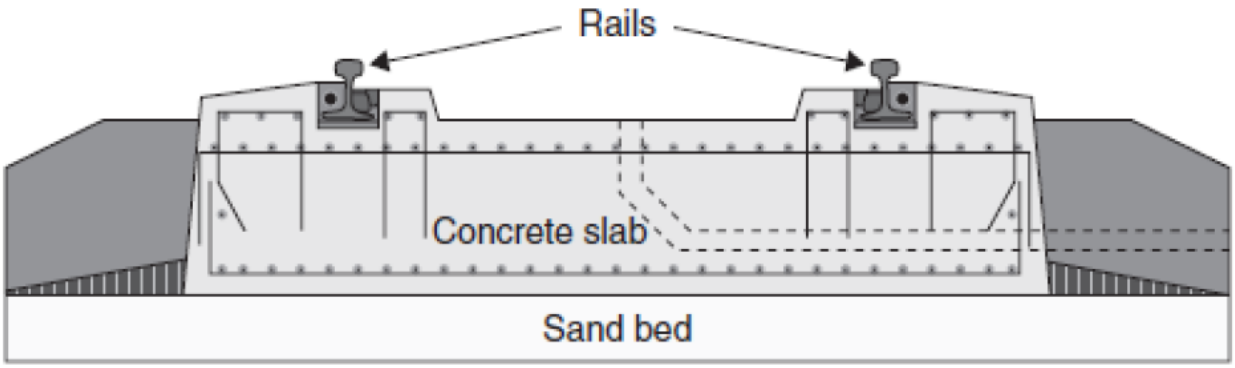

(b) Cross-section of a slab track (Esveld 2001)

Figure 2.2 Two types of commonly used rail tracks

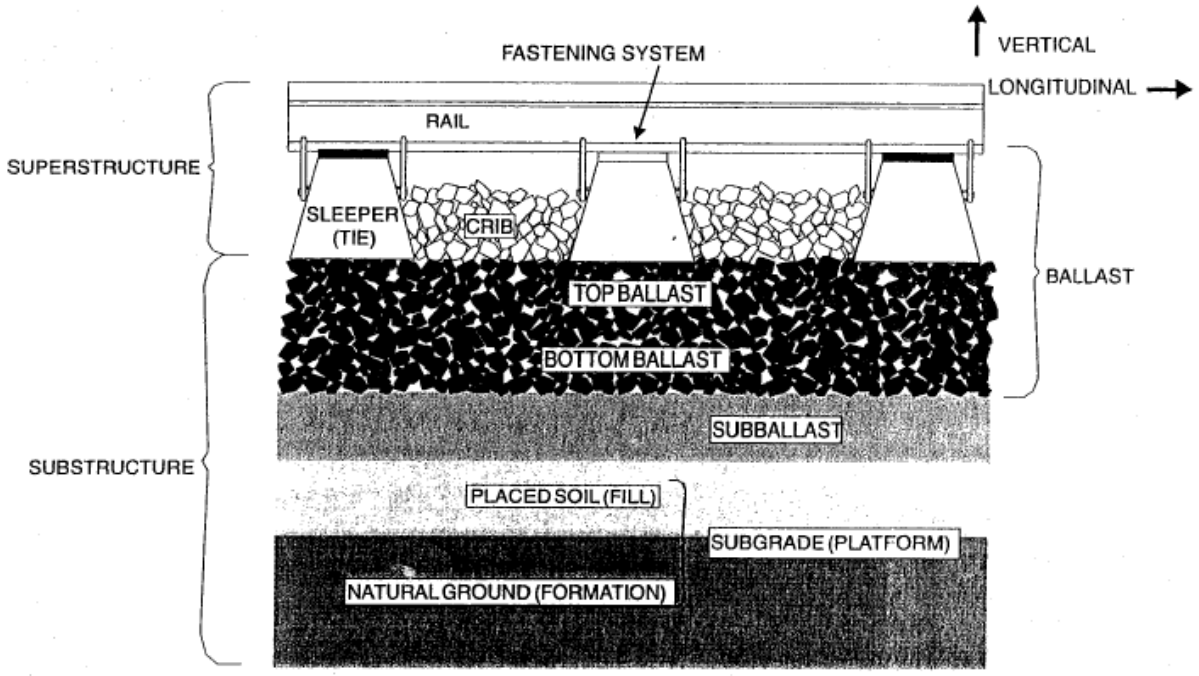

Figure 2.3 Ballasted track structure components (Selig and Waters 1994)

Figure 2.3 shows a typical ballasted track section and its key components in the longitudinal direction, dividing them into the superstructure and substructure (Selig and Waters 1994). The superstructure consists of the rail, fasteners, and ties. On the other hand, the substructure contains the ballast, subballast, and subgrade. The subgrade includes a layer of soil fill and natural ground. The sleeper-ballast interface separating the superstructure from the substructure is the most important part of the track since it distributes the loads to the railway track foundation. In this study, this interface is used to distribute train loads.

2.2.2 Moving Loads on a Railway Track Structure

There are three types of loads transmitted to the railway track foundation: static, cyclic, and dynamic loads (Li et al. 2002). Under moving train loads, shear stresses grow on horizontal and vertical planes since the principal stresses rotate to withstand the applied load (Wong et al. 2006).

Static loading on the track foundation contains two components: live load and dead load, which depend on the weight of the train, track, and subgrade. The weight of a train is transferred to the tracks and subgrade at the wheel and rail contact points. The stresses due to the weight of track and subgrade are mainly determined by 1) rail weight that depends on the size of the rail and its cross-section, 2) sleeper weight which is governed by the type of material and the size of the tie, and 3) the weight of track substructure (ballast, subballast, and subgrade) which relies on the material type and can be estimated by Equation (2.1) (Li et al. 2002).

$$w = \gamma * z \tag{2.1}$$

where w is the weight of track substructure per unit area (kg/m^2), γ is the unit weight of the material (kg/m^3), and z is the depth of track substructure (m).

According to Li et al. (2016), cyclic loading is a type of repeated loading generated by passing trains. Cyclic loads are characterized by their shape, duration, magnitude of loading pulse, time interval between consecutive pulses, and the total number of loading pulses. The duration of the loading pulse depends on the operating speed of the train and the depth of consideration and can be calculated by Equation (2.2):

$$t = \frac{L}{V} \tag{2.2}$$

Where t is the time duration of loading pulse, V is the train speed, L is the influence length of an axle load or adjacent axle loads for a given depth of ballast or subgrade.

Dynamic loading, also called impact loading, is either a short duration force with no reaction time for the vehicle suspension and track foundation or a longer duration load with enough time for the dynamic wheel loads to be transmitted into the track substructure (Li et al. 2002). The short duration forces are due to the discontinuities of wheel or rail in a limited track length, which lead to a short duration pulse, are illustrated in Figure 2.4. The long duration forces are caused by track geometry irregularities (Indraratna et al. 2011).

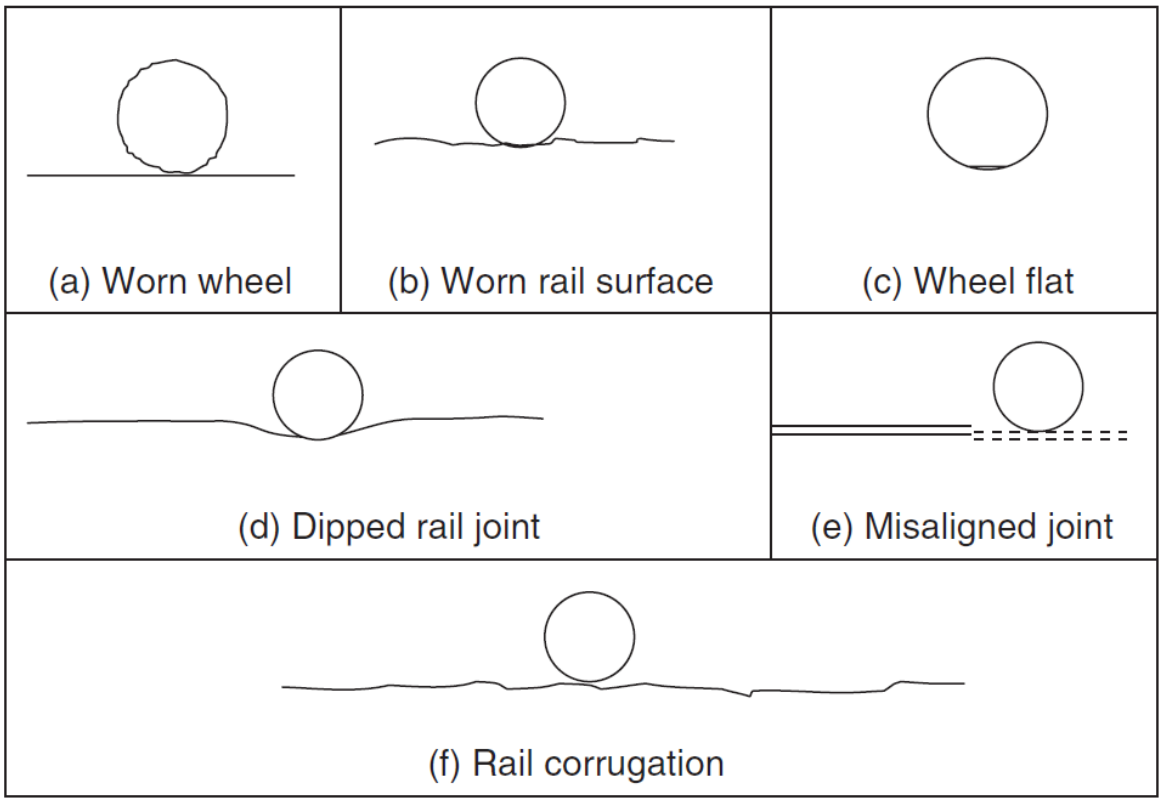

Figure 2.4 Different sources of impact loading in rail track (Indraratna et al. 2011)

2.2.3 Load Transfer Mechanism

Figure 2.5 shows the typical distribution of wheel loads to the rails, sleeper, ballast, subballast, and subgrade (Indraratna et al. 2011). The superstructure and substructure are separated by the sleeper-ballast interface. In the simulations performed in this thesis, the train loads are distributed to the substructure through the aforementioned interface.

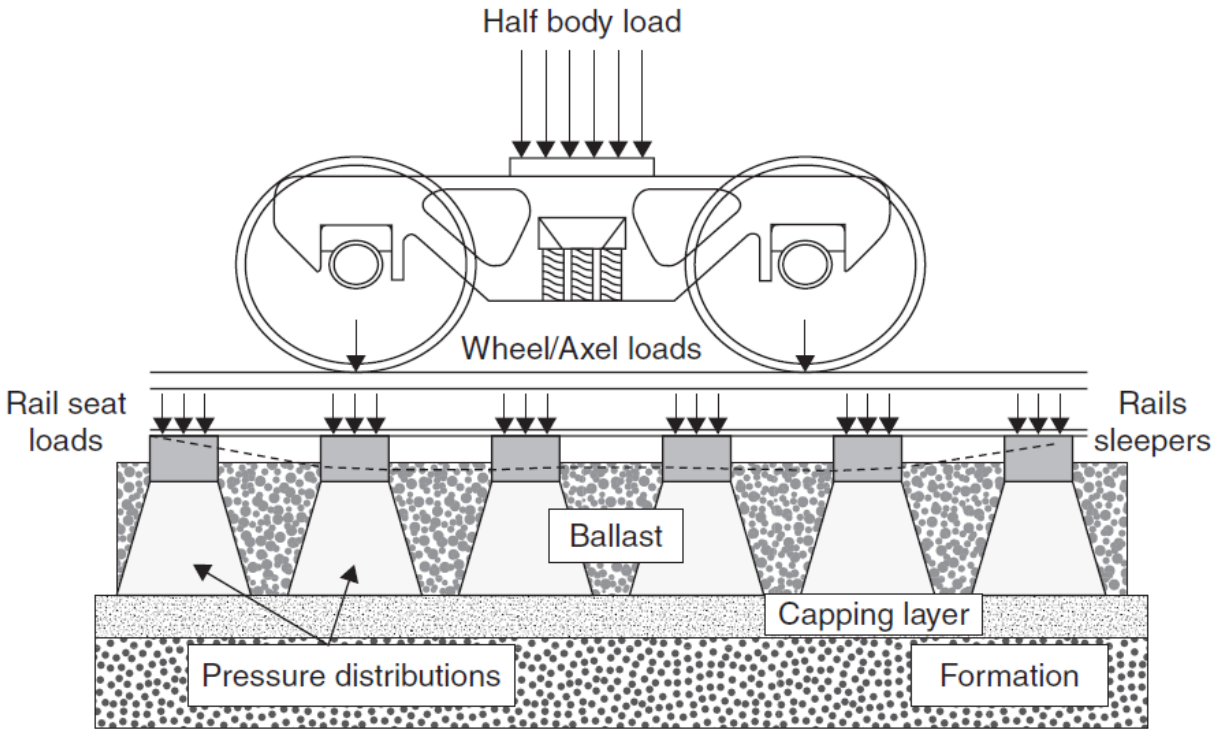

Figure 2.5 Typical wheel load distribution in track (Indraratna et al. 2011)

In the current load transfer mechanism, the vertical static wheel load is transferred to the rail and then distributed to the ties through the rail seat (Sadeghi and Barati 2010). Rail seat loads vary with different sleepers located away from the application of the load. As shown in Figure 2.6, the maximum rail seat load is 50% of the wheel load on the sleeper, and the adjacent sleepers each carry 25% of the wheel load (Zhang et al. 2016).

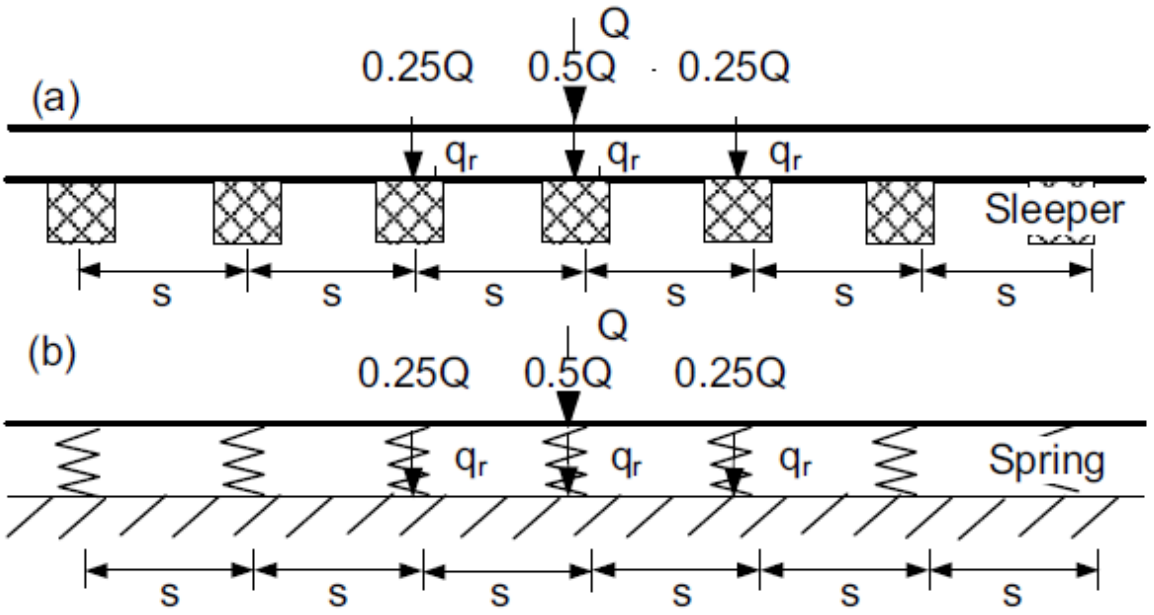

Figure 2.6 Rail seat load determination (Zhang et al. 2016), where Q is the wheel loading, s is the crosstie spacing

Although various methods have been developed to calculate the maximum vertical stress for a plane strain situation on the subgrade, the load distribution method proposed by AREMA (2010) is adopted in this thesis. AREMA, the American Railway Engineering and Maintenance-of-Way Association, is a North American railway industry group. It provides recommended practices for railway infrastructure design, construction and maintenance, which is the main standard used by North American railways. The force due to the rolling stock and rails on the timber sleepers need to be determined manually and applied as an external load. The equation to calculate the tie-to-ballast pressure includes (AREMA 2010):

a) Impact factor

The design dynamic wheel load is determined by multiplying the static wheel load by a dynamic load factor (DIF), also known as impact factor (IF). Since the stress caused by the wheel load on a sleeper (cross tie) is affected by the train speed, the impact factor (IF) for the track can be calculated by Equation (2.3):

$$IF = \frac{33V}{100D} \tag{2.3}$$

Where V is velocity (mi/h), and D is the diameter of the wheel (in).

b) Distribution factor

The distribution of the load is a function of the tie and axle spacing, and the percentage of the wheel-to-tie load carried by an individual tie depends on the tie's location. Figure 2.7 shows the percentage of the axle load carried by a single tie as a function of the center-to-center tie spacing.

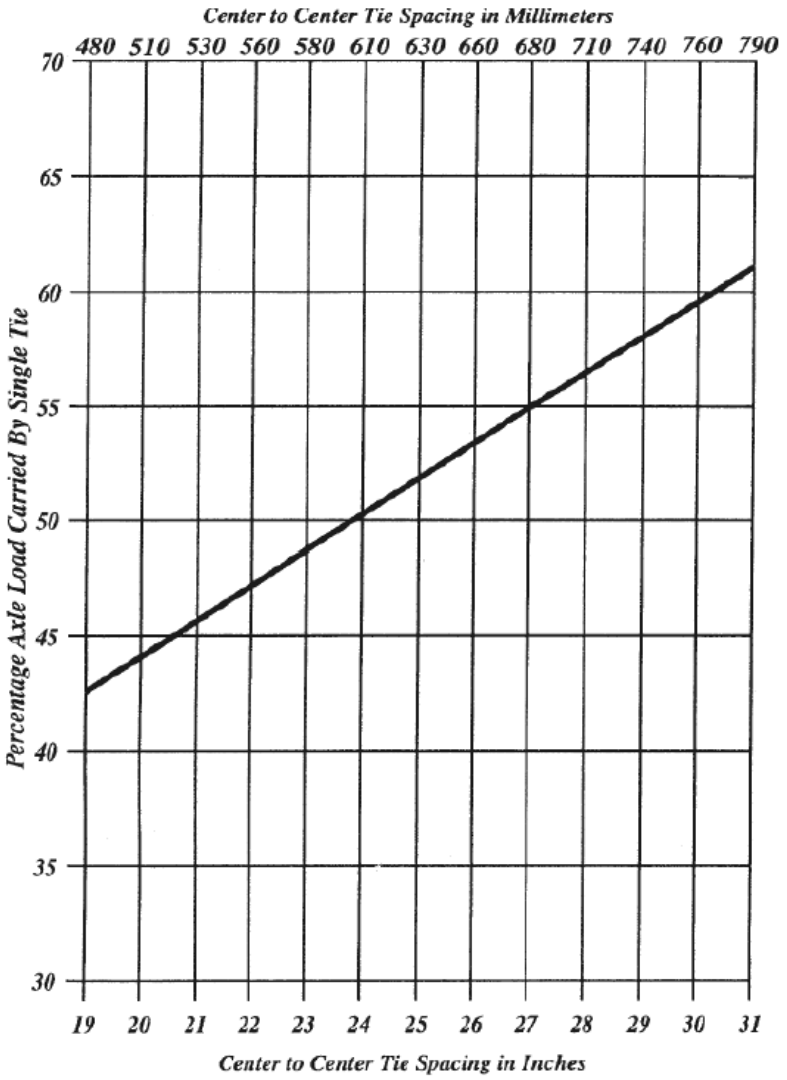

Figure 2.7 Estimated distribution of load (AREMA 2013)

c) AREMA formula for average ballast pressure (psi) at tie face

While the actual tie-to-ballast pressure is not uniformly distributed along the base of the tie, the AREMA method makes a simplifying assumption by computing the average pressure at the bottom of the tie. This average pressure is related to the axle load modified by distribution factor, the impact factor, and the bearing area of the tie. The equation of Average Ballast Pressure (ABP) is expressed as:

$$ABP = \frac{(2F)[1+\frac{IF}{100}](\frac{DF}{100})}{A} \tag{2.4}$$

where F is wheel load in pounds (or kN), IF is impact factor in percent, DF is distribution factor in percent, and A is bearing area of cross ties in square inches (or square millimeters). The resulting ABP is given in psi (or MPa).

2.3 Analysis of a Slope with Rising Groundwater Levels

Drainage paths under or within a railway embankment may become clogged due to their obstruction by debris, plugs of ice, or ballast pockets. Congested drainage paths may lead to a rise in groundwater levels under and within an embankment, potentially creating conditions conducive to slope instability.

This section discusses the means by which water levels may rise in an embankment slope and then describes how transient seepage and solid-fluid interaction are considered in FEM.

2.3.1 Rising Water Level

Rising groundwater levels have been the root cause of a large number of subgrade failures (Jiang et al. 2016). The Canadian Transportation Safety Board (TSB) established that despite the fact that the railway track remained intact and suspended over the deteriorated substructure, the embankment has lost its capability to support the train loads due to the build-up of water pore pressure caused by frequent rains, rapid melting of snow, and inadequate drainage system (Gitirana 2005). Fines will migrate from the subgrade into the ballast and fill the void space due to the generation of excess pore water pressure and the upward migration of water.

Excessive moisture in the track substructure layers results in higher rates and magnitudes of deformation, lower resilient modulus, higher plastic strain, and lower strength. These phenomena are true for both granular (usually used in ballast, subballast layer) and cohesive soils (subgrade layer) (Li et al. 2002).

a) Granular soil

The following equations define the effective stress and shear strength of a granular soil:

$$\sigma' = \sigma_T - u \tag{2.5a}$$

$$s = \sigma' tan\emptyset \tag{2.5b}$$

where effective stress σ', total stress σ_T, the effective pore water pressure u; the shear strength s, internal angle of friction $\emptyset$.

Equation 2.5 shows that pore water pressure weakens a granular soil by reducing the effective stress. The greater is the pore water pressure, the smaller is the effective stress, and consequently, lower is the soil strength. Under saturated conditions, pore water pressure can develop. When certain soils are subjected to cyclic loading, they may experience an increase in pore water pressure that exceeds the total stress, resulting in a severe loss of strength and large deformations. Figure 2.8 shows liquefaction of a poorly draining subballast layer causing track geometry degradation (Read and Li 1995).

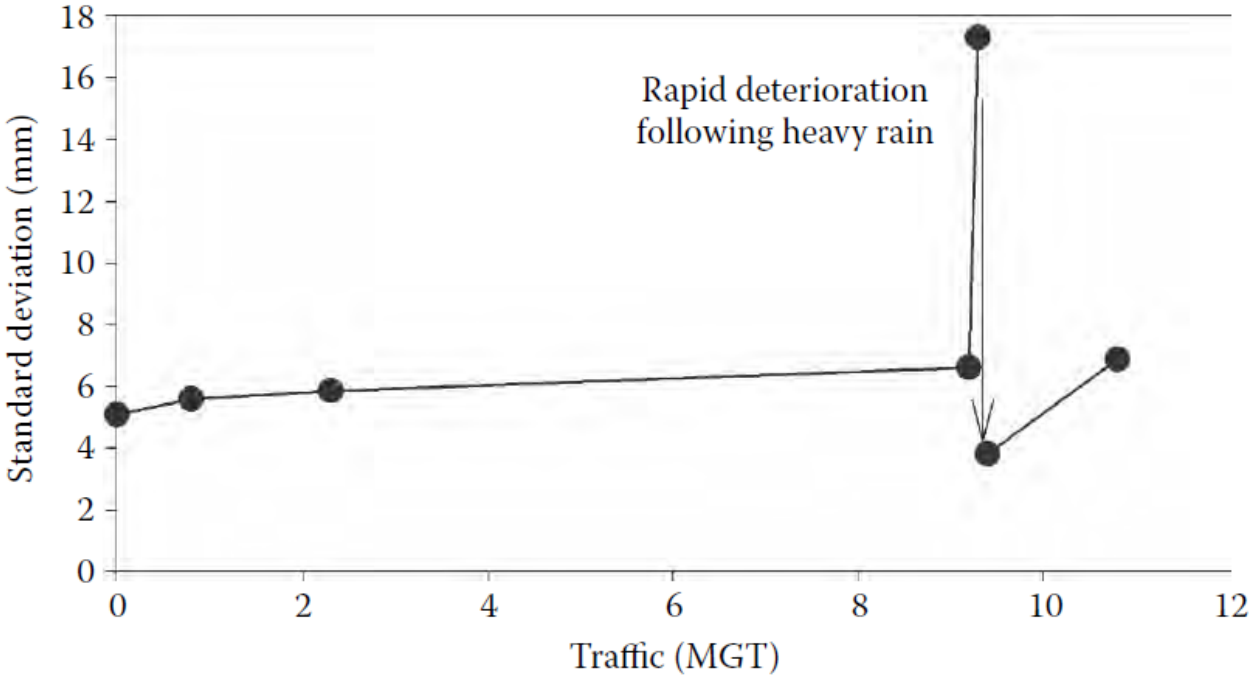

Figure 2.8 Track vertical profile degradation from liquefaction of thick subballast layer (Read and Li 1995)

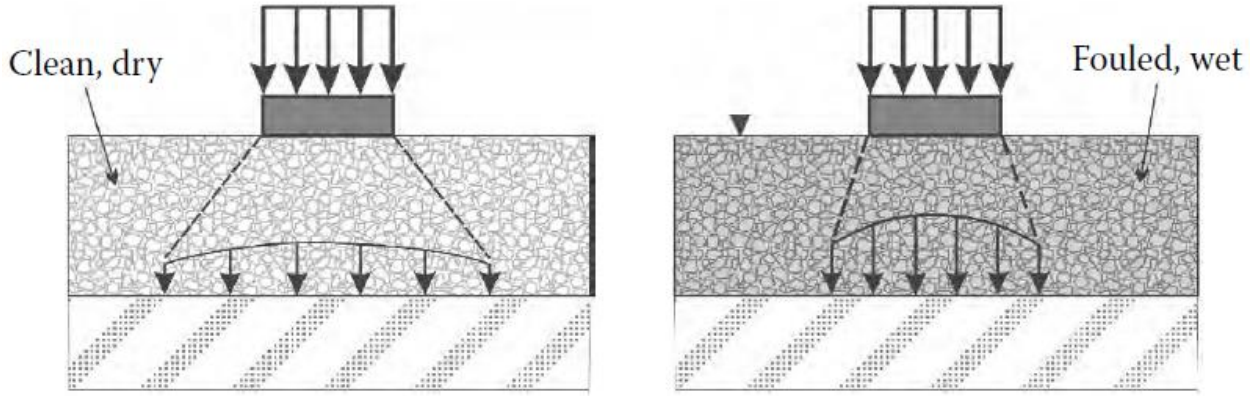

Figure 2.9 Idealized concept of stress transmission from well-drained (a) and saturated granular (b) layers (Cedergren 1989)

Figure 2.9 compares how the stress from train loading is transmitted vertically through two different water conditions within the ballast. Figure 2.9 (a) indicates that when stresses are solely transmitted at the ballast particle contacts, the ballast layer stiffness significantly decreases the stress in the underlying layer. However, when the ballast is wet and fouled, i.e., filled with fine saturated material, the granular layer loses some of its stiffness and experiences a reduction in its load spreading ability, resulting in greater stresses being transmitted to the underlying stratum (see Figure 2.9 (b)) (Cedergren 1989).

b) Cohesive soil

The strength and deformation characteristics of fine-grained cohesive soils are governed by the effective stress, similar to granular soils. However, cohesion is influenced by the mineralogical composition of clay soils, which controls how clay particles interact with water (Li et al. 2002).

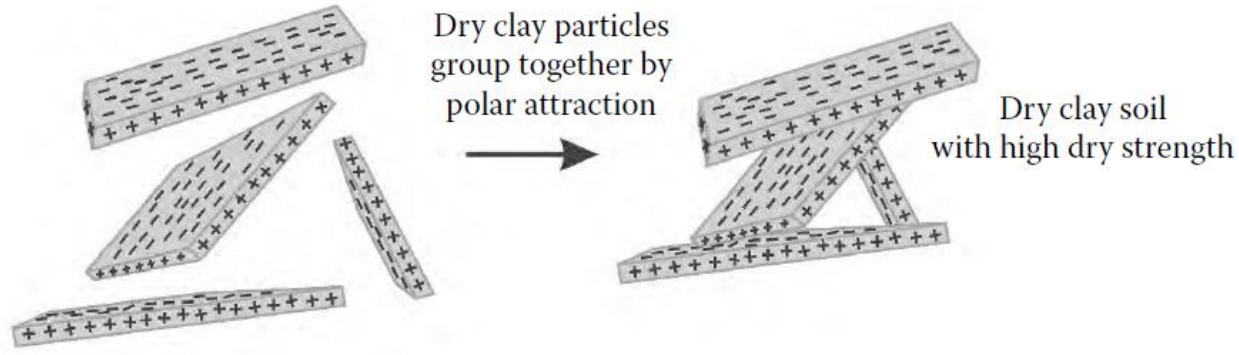

(a)

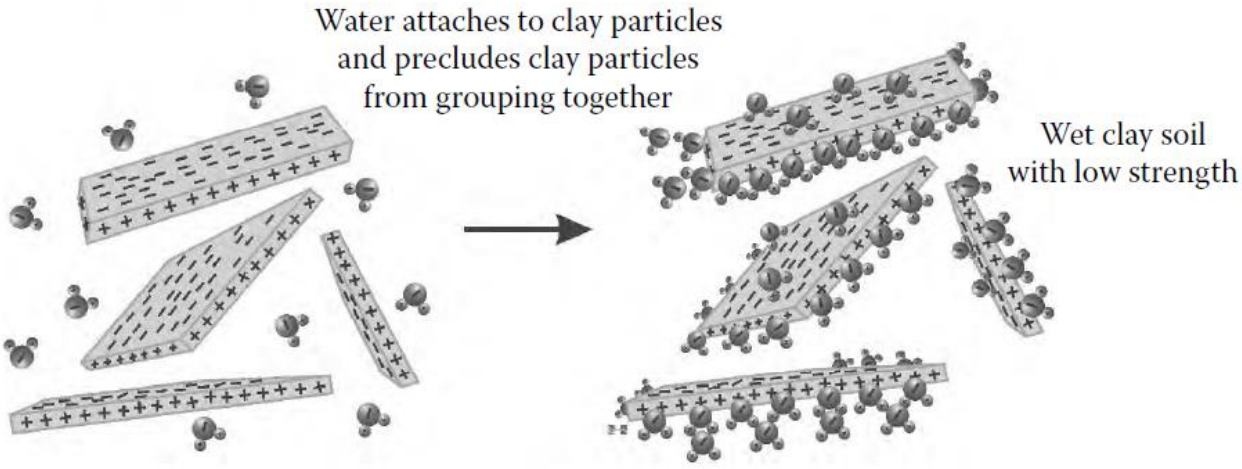

(b)

Figure 2.10 Illustration of clay's affinity for water: (a) is dry clay, (b) is wet clay (Li et al. 2002)

Figure 2.10 illustrates clay's affinity for water. When the clay is dry, the cohesive particles are attracted closely to one another, resulting in a relatively strong attractive force, and subsequently, a high dry strength. In Figure 2.10 (b), water attaches to clay particles, creating a layer between them, which inhibits the clay particles from bonding to each other, resulting in a low strength of the clay soil mass.

2.3.2 Consolidation Theory and the Biot Model

Consolidation is a critical problem in geotechnical engineering. In practice, the consolidation theories can be used to forecast the amount and rate of consolidation settlement. Terzaghi (1925) first proposed the one-dimensional consolidation theory. Subsequently, Rendulic (1936) expanded

Terzaghi's theory to adapt for three-dimensional consolidation conditions (Baqersad et al. 2016). Biot (1941) studied the relationship between the excess pore pressure dissipation and the soil skeleton's deformation and introduced the coupled consolidation theory. From then on, Biot's consolidation theory and its modification have been widely used since they are more accurate (Baqersad et al. 2016).

To minimize the computing time and simplify equations for porous media, another form of the Biot model was proposed by Zienkiewicz and Shiomi (1984). Panneton and Atalla (1997) solved the three-dimensional poroelasticity problem in acoustics using the FEM based on Biot's theory (Albers et al. 2012).

The Biot model is used to simulate the subsoil (Albers et al. 2012). The Biot consolidation equations have been implemented in many numerical modeling packages to model coupled consolidation. In the Biot theory, the mechanical behavior of a soil skeleton is treated as a porous elastic solid with laminar pore fluid flow coupled with the solid by the conditions of equilibrium and continuity. The coupled Biot equations for a 2D poroelastic material can be derived in two steps. First, the 2D equilibrium equations are defined as follows (Smith et al. 2013):

$$\frac{\partial \sigma_x'}{\partial x} + \frac{\partial \tau_{xy}}{\partial y} + \frac{\partial u_w}{\partial x} = 0 \tag{2.6a}$$

$$\frac{\partial \tau_{xy}}{\partial x} + \frac{\partial \sigma_y'}{\partial y} + \frac{\partial u_w}{\partial y} = 0 \tag{2.6b}$$

Where σ_x' and σ_y' are the effective stresses $(\sigma - u_w)$, and u_w is the fluid pressure.

Equation (2.6) can be simplified by expressing the stress terms in terms of the displacements (Griffiths 1994). This simplification is made based on the assumptions that strains are in-plane and small, as follows:

$$\frac{E\prime(1-v')}{(1+v')(1-2v')}\left[\frac{\partial^2 u^*}{\partial x^2} + \frac{(1-2v')}{2(1-v')}\frac{\partial^2 u^*}{\partial y^2} + \frac{1}{2(1-v')}\frac{\partial^2 v^*}{\partial x \partial y}\right] + \frac{\partial u_w}{\partial x} = 0 \tag{2.7a}$$

$$\frac{E\prime(1-v')}{(1+v')(1-2v')}\left[\frac{1}{2(1-v')}\frac{\partial^2 u^*}{\partial x \partial y} + \frac{\partial^2 v^*}{\partial y^2} + \frac{(1-2v')}{2(1-v')}\frac{\partial^2 v^*}{\partial x^2}\right] + \frac{\partial u_w}{\partial y} = 0 \tag{2.7b}$$

where E' and v' are the effective elastic parameters, and u^* and v^* are the components of displacement in the x and y direction respectively.

Then, considering 2D continuity, if the net flow rate is equivalent to the volume rate of change of the soil element, then (Smith et al. 2013):

$$\frac{\partial}{\partial t}\left(\frac{\partial u^*}{\partial x} + \frac{\partial v^*}{\partial y}\right) + \frac{k_x}{\gamma_w}\frac{\partial^2 u_w}{\partial x^2} + \frac{k_y}{\gamma_w}\frac{\partial^2 u_w}{\partial y^2} = 0 \tag{2.8}$$

Where k_x and k_y are the material permeabilities in the x and y directions, respectively.

Equation (2.7) and (2.8) are the coupled Biot equations, which can be interpreted that at a spatial location (x, y) at any time t, the displacements u^*, v^* and excess pore water pressure u_w can be predicted. However, seepage patterns may not reach a steady-state during the simulation due to the dynamic boundary conditions.

2.3.3 Transient Seepage Analysis

In a water level rising condition, the variable of pore water pressure is dependent on the total stress acting against the slope and the increasing pressure heads (Collins et al. 2004). When analyzing the pore pressure induced by transient flow, the time-dependent boundary condition is dynamic and different from a steady-state seepage condition.

The governing equation for transient fluid flow in the soil can be defined as a mass balance such that the mass of water flow in or out of a reference volume of soil is equal to the change in water mass within the reference volume. Thus, assuming incompressible water, homogeneous soil, and direction of permeability with the coordinate system, this equation takes following form (Bear 2012):

$$k_h \frac{\partial^2 h}{\partial x^2} + k_v \frac{\partial^2 h}{\partial y^2} = n \frac{ds}{dt} + S\gamma_w m_v \frac{dh}{dt} \tag{2.9}$$

where k_h is the horizontal hydraulic conductivity, k_v is the vertical hydraulic conductivity, h is the total head, n is porosity, S is the degree of saturation, γ_w is the unit weight of water, and m_v is the coefficient of compressibility.

For saturated conditions (S=1.0), Equation (2.9) can be simplified as:

$$\frac{k_h}{\gamma_w m_v} \frac{\partial^2 h}{\partial x^2} + \frac{k_v}{\gamma_w m_v} \frac{\partial^2 h}{\partial y^2} = \frac{dh}{dt} \tag{2.10}$$

or

$$C_h \frac{\partial^2 h}{\partial x^2} + C_v \frac{\partial^2 h}{\partial y^2} = \frac{dh}{dt} \tag{2.11}$$

Where C_h is the coefficient of consolidation in horizontal x direction, and C_v is the coefficient of consolidation in the vertical y direction.

Equation (2.11) shows that the coefficients of consolidation determine the rate of change in the head in a saturated zone. Therefore, in transient seepage analysis, the total heads and pore pressures are dependent on the values of k and m_v, with an important effect on the coefficients of consolidation.

There are two methods to predict the pore water pressures due to a rise in water level: uncoupled transient seepage analysis and coupled transient seepage analysis. In the 1980s, uncoupled transient analysis based on the FEM was developed to analyze slope stability (Li and Desai 1983; Lam et al. 1987). Pore pressures are associated with the changes in total stress and head boundary conditions. However, the uncoupled transient analysis only considers the influence of hydraulic boundary conditions when used to predict pore pressure in the slope after the water table has risen. Unlike the uncoupled method, the coupled transient analysis considers changes in both stress and pore pressure simultaneously (Pinyol et al. 2008).

In the coupled analysis, several complex constitutive models have been used to couple changes in pore pressure and total stress boundary conditions while solving the transient seepage equation. In this equation, the transient seepage analysis was coupled with the Biot consolidation theory. An elastic-plastic constitutive model (Mohr-Coulomb model) was adopted and is discussed in detail in Section 2.6.

2.4 Key Parameters of the Model

It is important to collect key parameters of a model to create a reasonable representation of the physical reality. In this section, to present a reliable model, some key parameters need to be set within a reasonable range or as specific values. There are three parts in the proposed model: 1) the railway system, 2) the foundation condition, 3) the freight train. These parameters are discussed in detail, including the size of a freight train, the magnitude of moving loads, the dimension of railway embankments, the inclination ratio of the slope, and soil or material properties.

2.4.1 Railway Track Structure

This section discusses the parameters of the superstructure (e.g., track gauge, sleeper (cross-tie) dimensions, sleeper spacing, and their material properties) and substructure (e.g., the thickness of each layer, the slope geometry, and material properties of each layer).

a) Superstructure

The track gauge is the spacing between the inner sides of the rails, which is measured 14 mm below the rolling surface, as shown in Figure 2.11 (Profillidis 2014). Table 2.1 lists typical values of track gauges in different countries. The most common track gauge is the standard gauge, measuring 1,435mm (Selig and Waters 1994).

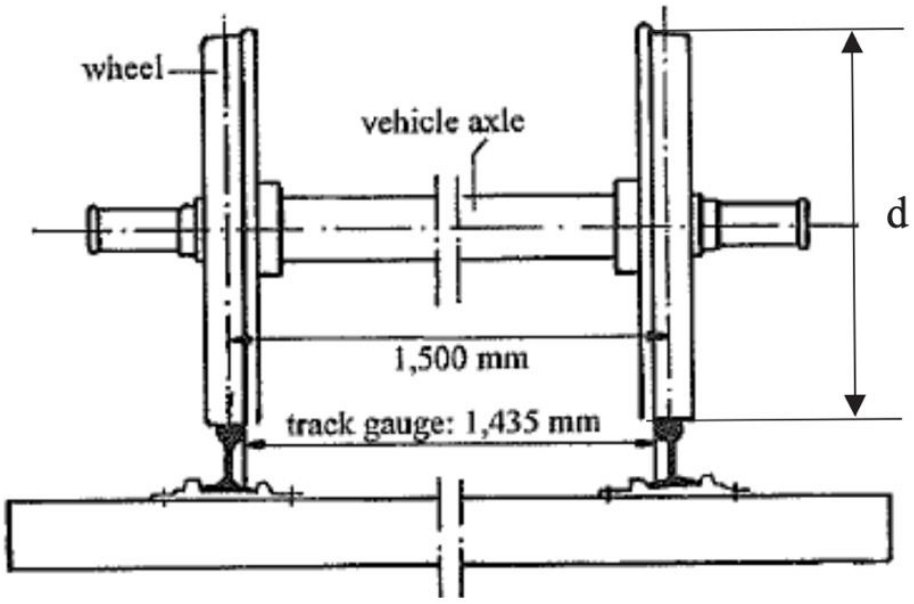

Figure 2.11 Wheel of the railway freight car with a standard gauge track (Profillidis 2014)

Table 2.1 Rail gauge value in different countries (Selig and Waters 1994)

Location	Gauge (mm)	Gauge (in.)
North America	1435	56.5
Europe	1435-1668	56.5-65.7
South America	1065	41.9
Australia	1524-1676	42-63
China	1435	56.5

The sleeper (crosstie) is commonly made of timber, concrete, or steel. Wood is easier to obtain than concrete and steel, and timber ties are not as expensive as concrete and steel. Concrete sleepers are very good at resisting movement but may fracture when exposed to high cyclic and impact loads (Indraratna et al. 2011).

Common sleeper dimensions and spacings are shown in Table 2.2. The standard size of a timber sleeper supporting heavy axle freight train loading in North America is 2.59m in length, 0.229m in width, and 0.152m or 0.178m in height. In this study, a tie spacing of 0.495m is used (Selig and Waters 1994).

Figure 2.12 illustrates the geometric characteristics of wooden sleepers with standard track gauges in Europe, and Figure 2.13 shows a diagram of a timber sleeper layout (Profillidis 2014).

Table 2.2 Typical sleeper dimensions (Selig and Waters 1994)

Location	Material	Width (mm)	Length (mm)	Spacing (mm)
Australia	Wood	210-260	2000-2743	610-760
	Concrete	/	/	600-685
China	Wood	190-220	2500	543-568
	Concrete	240-290	2500	568
Europe	Wood	250	2600	630-700
	Concrete	250-300	2300-2600	692
North America	Wood	229	2590	495
	Concrete	286	2629	610
South Africa	Wood	250	2100	700
	Concrete	203-254	2057	700
		230-300	2200	600

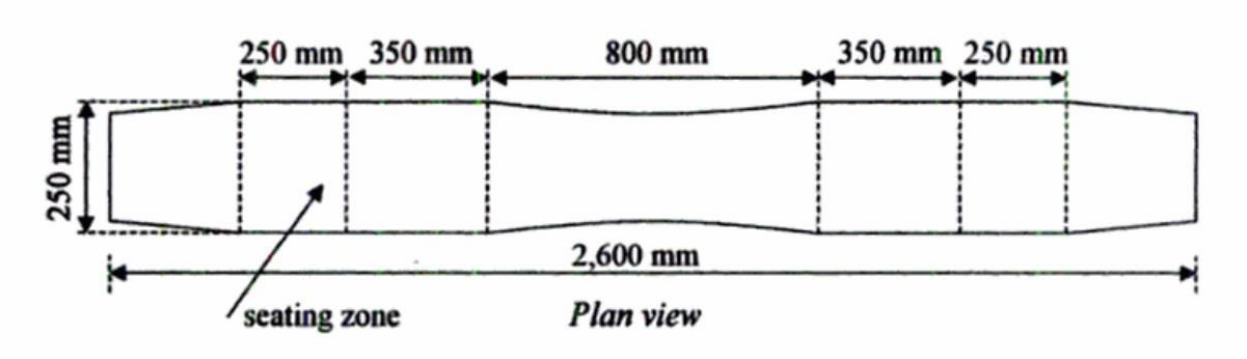

Figure 2.12 Geometrical characteristics of timber sleepers in the standard track gauge (Profillidis 2014)

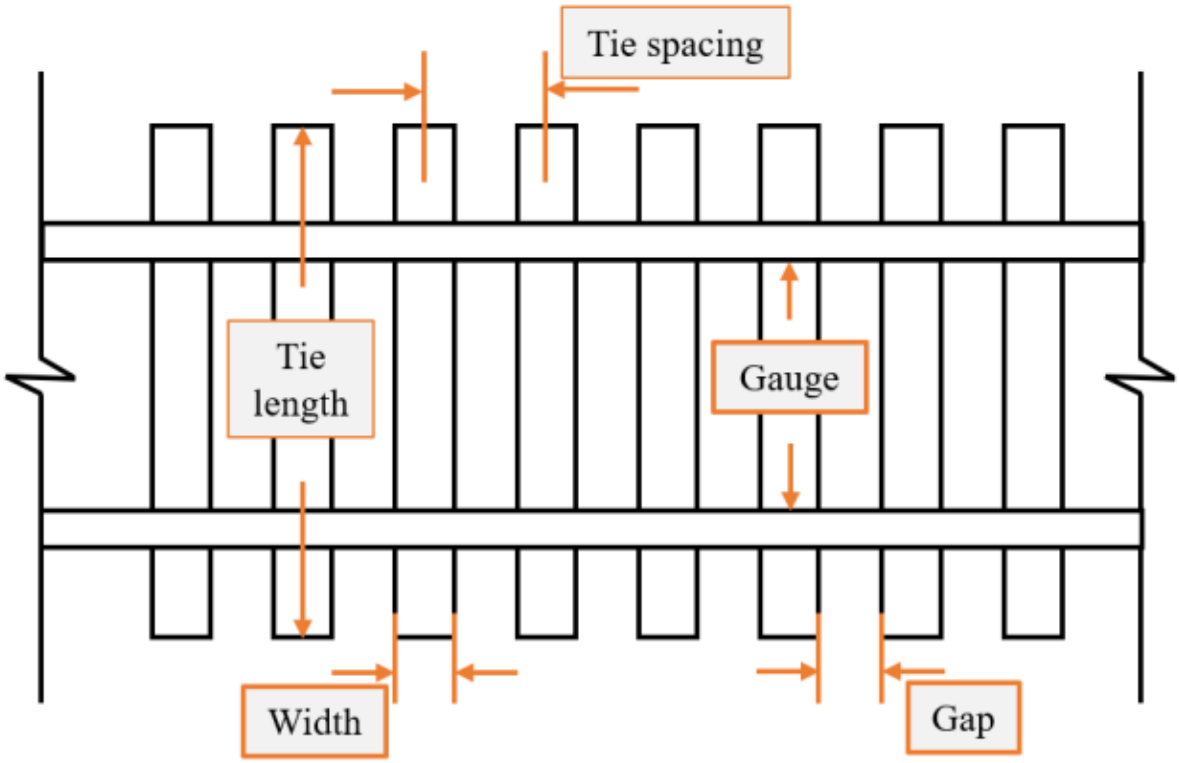

Figure 2.13 Diagram of timber sleeper layout. (Profillidis 2014)

In addition to geometric parameters, material properties are also important factors that need to be considered. Table 2.3 shows that a timber sleeper has better tensile (R_T) and compressive (R_C) strengths than a concrete sleeper (Profillidis 2014).

Table 2.3 Values of mechanical characteristics of sleeper materials (Profillidis 2014)

Material	Elasticity modulus (MPa)	Poisson's ratio	Tensile strength R_T (MPa)	Compressive strength R_c (MPa)
Reinforced-concrete sleeper	2.94×10^4	0.25	2.94	29.42
Prestressed-concrete sleeper	4.9×10^4	0.25	5.88	8.83
Tropical timber sleeper	2.45×10^4	0.25	9.81	98.07
Rail (steel)	2.06×10^5	0.30	686.47	588.40

The following superstructure geometrical parameters are selected for this study:

- Rail gauge: 1,435mm
- Timber sleepers: 229mm wide, 2,950mm long spaced at 495mm
- The material properties of the timber sleepers correspond to those shown in Table 2.3

b) Substructure

A railway embankment's substructure consists of the ballast, subballast, and subgrade. AREMA's Manual for Railway Engineering (AREMA 2010) recommends a range of substructure geometrical parameters. For a standard gauge (1435 mm), a minimum ballast thickness of 12 inches (304 mm) is recommended. The subballast depth varies from 100 mm to 150 mm (Indraratna et al. 2011). The subgrade may be the natural soil with a thickness usually over 2,000 mm (Egeli and Usun 2012). A minimum ballast shoulder width of 12" (304mm) is recommended. Every country or railway organization has its own criterion for embankment materials. The ballast is normally made of locally available geomaterials, like angular or uniformly graded materials which can support the train load and resist harsh environmental conditions (Indraratna et al. 2011). The nominal ballast size is 60mm, hard rock, such as granite, quartzite, and carbonate stone, can also be used as an alternative (AREMA 2010). The subballast is typically a granular material, such as crushed stone, natural or crushed gravel, crushed slag, or a homogeneous mixture of these materials. Material properties and mechanical characteristics of railway embankments are shown in Table 2.4 and Table 2.5. At the same time, the different types of subgrade properties are also shown in Table 2.5.

Table 2.4 Mechanical characters of railway embankment (Li et al. 2016)

Name	Density (Mg/m^3)	Poisson's ratio	Modulus (MPa)	Thickness (m)
Ballast	1.76	0.3	276	0.3
Subballast	1.92	0.35	138	0.15
Subgrade	1.92	0.35	41	infinite

Table 2.5 Values of mechanical characteristics of subgrade materials (Profillidis 2014)

Material	Elasticity modulus (kp/cm^2)	Elasticity modulus (MPa)	Poisson's ratio	Cohesion (kp/cm^2)	Cohesion (kPa)	Friction angle (°)
Poor quality subgrade	125	12.26	0.4	0.15	14.71	10
Medium quality subgrade	250	24.52	0.3	0.1	9.81	20
Good quality subgrade	800	78.45	0.3	0	0.00	35
Rock subgrade	30000	2942.00	0.2	15	1471.00	20
Ballast	1300	127.49	0.2	0	0.00	45
Gravel subballast	2000	196.13	0.3	0	0.00	35
Sand	1000	98.07	0.3	0	0.00	30

Note: 1 kp/cm^2 = 98.067 kPa=0.098 MPa

Typical values of the hydraulic conductivity of saturated soils are discussed in Table 2.6 which shows the drainage performance of various soils used in railway embankments.

Table 2.6 Typical values of hydraulic conductivity of saturated soils (Budhu 2010)

Soil type	k (cm/s)
Clean gravel	>1.0
Clean sands, clean sand, and gravel mixtures	1.0 to 10^{-3}
Fine sands, silts, mixtures comprising sands, silts, and clays	10^{-3} to 10^{-7}
Homogeneous clays	$<10^{-7}$

AREMA's Manual for Railway Engineering recommends a typical slope inclination of 1V:2H (AREMA 2010). But other ratios (e.g., 1V:3H) are also accepted. The inclination of a ballast slope may differ from that of the subballast and subgrade slopes, which are summarized in Table 2.7.

Table 2.7 Values of slope inclination (Calamak and Yanmaz 2016; Egeli and Usun 2012; Profillidis 2014)

Name	Horizontal	:	Vertical
Ballast slope	3	:	1
	2	:	1
Subballast and subgrade slope	3	:	1
	2	:	1

2.4.2 Soil Properties of the Foundation Soil

For the foundation soil mass, soil properties include the unit weight, cohesion, internal friction angle, Young's modulus, and Poisson's ratio. The unit weight is a basic soil property. The cohesion and internal friction angle are used to define the soil's behavior in the Mohr-Coulomb constitutive model. The soil's elastic deformation is expressed by the Young's modulus and Poisson's ratio. Typical values of these parameters for common embankment materials are summarized in Table 2.8. Table 2.9 also lists the range of common soil properties (Xie et al. 2016; Zhang et al. 2014; Chakeri and Ünver 2014; Ercelebi et al. 2011).

Table 2.8 The base of embankment material (Brzeziński, Rybicki, and Józefiak. 2018)

Material	Bulk density (g/cm^3)	Friction angle (°)	Cohesion (kPa)	Young's modulus (MPa)	Poisson's ratio
Coarse aggregate	1.85	45	1.0	200	0.2
Coarse sand	1.80	49	2.0	100	0.25
Sandy clay	2.20	18.3	31.5	21.1	0.29

Table 2.9 The credible range of soil functional parameters (Xie et al. 2014; Zhang et al. 2014; Chakeri and Ünver 2014; Ercelebi et al. 2011)

Name	Unit weight (kN/m^3)	Poisson's ratio	Friction angle (°)	Cohesion (kPa)	Young's modulus (MPa)
Clay	16.5	0.35	14.0	20.0	20.0
Silty clay	17.7-19.4	0.28-0.38	13.5-30.0	14.0-18.0	5.27-25.0
Hard clay	17.2	0.4	20.0	25.0	28.0
Clay-silt	19.0	0.35	27.0	40.0	30.0
Sandy silt	18.2	0.24	30.3	3.0	45.0
Dense sand	19.0	/	35.0	/	24.0
Very dense sand	19.5	/	35.0	/	

The typical values of E (modulus of elasticity), G (shear modulus), and Poisson's ratio for different soils under drained conditions are shown in Table 2.10 and Table 2.11, respectively.

Table 2.10 Typical values of E and G (Budhu 2010)

Soil type		E (MPa)	G (MPa)
Clay	Soft	1-15	0.5-5
	Medium	15-30	5-15
	Stiff	30-100	15-40
Sand	Loose	10-20	5-10
	Medium	20-40	10-15
	Dense	40-80	15-35

Table 2.11 Approximate values of Poisson's ratio of soils (Rowe 2012)

Soil	Poisson's ratio
Saturated soil, undrained loading	0.5
Clay, drained loading	0.2-0.4
Dense sand, drained loading	0.3-0.4
Loose sand, drained loading	0.1-0.3
Peat, drained loading	0-0.1

2.4.3 Freight Trains

A freight train consists of a locomotive and several freight cars. The train loading is a function of different variables, including the train weight, related axle load, and the reasonable operating speed. Each variable is described as follows:

- Table 2.12 summarizes the typical axle load of freight cars worldwide (Li et al. 2016).
- Table 2.13 shows the number of axles for different train types as well as their corresponding empty and loaded wheel loads (Esveld 2001).

Moreover, the train dimension is also required to identify the location of each axle load along a longitudinal section. The typical diameter of a freight car's wheel is 920 mm (Johansson 2006). Figure 2.14 shows the typical railcar dimensions for a standard freight car used in North America (Dick et al. 2011).

Table 2.12 Typical heavy axle loads of freight cars around the world (Li et al. 2016)

Country	Axle load (Tonnes)
United States and Canada	33
Australia	33-35
South Africa	26-30
Brazil	27.5-32.5
Sweden	30
China	25-27

Table 2.13 Number of axles and weight per axle of several types of rolling stock (Esveld 2001)

	Number of axles	Empty	Loaded
Trams	4	50kN	70kN
Light-rail	4	80kN	100kN
Passenger coach	4	100kN	120kN
Passenger motor coach	4	150kN	170kN
Locomotive	4 or 6	215kN	/
Freight wagon	2	120kN	225kN
Heavy haul (USA, Australia)	2	120kN	250-350kN

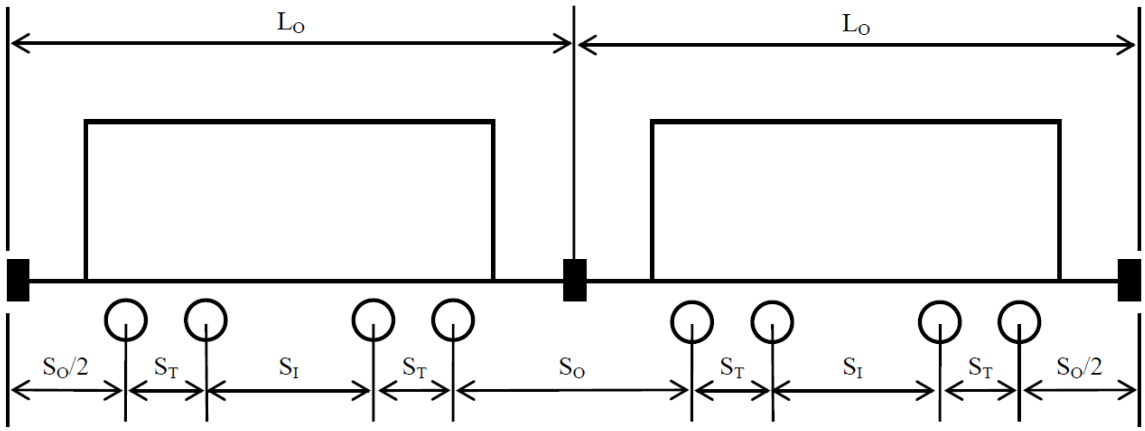

L_O - Overall length of railcar measured over the pulling face of the coupler
S_I - Inboard Axle Spacing, the distance between the inside axles of the railcar
S_O - Outboard Axle Spacing, the distance between the outside axles of the railcar
S_T - Truck Axle Spacing, the distance between the adjacent axles of a truck.

Figure 2.14 Typical railcar dimension for a standard freight car used in North America (Dick et al. 2011)

As shown in Table 2.14, the speed of a typical freight train varies from 30 km/h to 120 km/h. Thus, the most unfavorable condition of train loading is when the train speed is 120 km/h, and zero train speed means stationary.

Table 2.14 Maximum speed for different type of railway lines (Esveld 2001)

Type of railway lines	Passenger trains (km/h)	Freight trains (km/h)
Branch lines	/	30-40
Secondary lines	80-120	60-80
Main lines	160-200	100-120
High-speed lines	250-300	/

2.5 Review of Slope Stability Analysis Methods

Stability analysis and deformation analysis are two critical calculations in geotechnical designs (Terzaghi 1951). Stability analysis aims to determine if geotechnical structures are safe and stable. The stability of a slope can be analyzed by using methods such as the limit equilibrium method or other numerical methods, including the finite element method, discrete element method, or others (Cheng and Lau 2014). In this section, these methods are briefly described.

2.5.1 Numerical Methods

Numerical methods have been widely used in geomechanics. They can solve complex models that capture the behavior of geomaterials that would otherwise be unsolvable. For slope stability analysis, one of these numerical methods is extensively used. Currently, there are several popular numerical methods to study the behavior of a slope. In this section, frequently used numerical methods in geomechanics are briefly reviewed, including Limit Equilibrium Method (LEM), Discrete Element Method (DEM), Boundary Element Method (BEM), Finite Difference Method (FDM), and Finite Element Method (FEM).

a) Limit Equilibrium Method (LEM)

For slope stability analysis, the limit equilibrium method (LEM) is common and well-established. Fredlund and Krahn (1977) and Chen and Chameau (1983) stated that a simple theoretical approach, the ability to consider major effective factors on the shearing resistance, and reliable results are among the reasons for the popularity of LEM. The most common limit equilibrium methods are based on slices and allow for the calculation of stresses along the failure plane that is useful when analyzing slopes with nonuniform soil and pore water pressures. There are various refinements to these basic methods of analysis (Bishop 1955; Morgenstern and Price 1965; Spencer 1967; Janbu 1954; Li et al. 2002).

Duncan et al. (1996) found that the factor of safety (FS), the strength parameters of sliding surfaces, and the results obtained with limit equilibrium methods are accurate and reliable comparable with actual measurements and forecasted behavior of the slope material. The FS can be represented by the ratio of shear strength and shear stress within a soil (Equation (2.12) (Cheng and Lau 2014).

$$FS = \frac{shear\ strength\ of\ the\ soil}{shear\ stress\ of\ the\ soil\ mass} \tag{2.12}$$

LEMs rely on the following:

1) assume a slip surface exists
2) the static equilibrium for the entire failing soil mass (e.g., Swedish circle ($\emptyset_u = 0$) method (Fellenius 1922)) or the slices which are smaller blocks of failing soil mass (e.g., ordinary method of slices (Fellenius 1927)).

Krahn (2003) discussed the limitations of limit equilibrium analyses, such as convergence issues and difficulties with applying external forces, and suggested that the latter flaw can be best addressed by using a hybrid finite element-limit equilibrium analysis. Compared to LE methods, the FEM provides a framework to define soil properties such as stress-strain relationship. As a result, complex geotechnical problems can easily be studied with FEM (Putu Tantri and Lastiasih, 2015).

b) Discrete Element Method (DEM)

The discrete element method (DEM) was originally developed by Cundall and Strack (1979) to solve rock mechanics problems. It has been used extensively to study physical (powders in the pharmaceutical industry) and geotechnical phenomena such as deformation mechanisms, constitutive relations for soil, stability of rock masses, flow of granular media, ground collapse, and other types of geotechnical phenomena. This method is designed to deal with contact conditions for a mass of irregular particles (Munjiza 2004).

c) Boundary Element Method (BEM)

In comparison with the DEM, all the remaining methods (BEM, FDM, and FEM) discussed in this section are continuum methods. Moreover, the discretization of the BEM is different from both the FDM and the FEM. The BEM solves an integral boundary equation only related to the boundary values (Hall 1994). Thus, with the BEM, only the boundaries of the continuum need to be discretized, as shown in Figure 2.15. The entire medium and boundaries must be discretized for both the FDM and FEM (Bobet 2010).

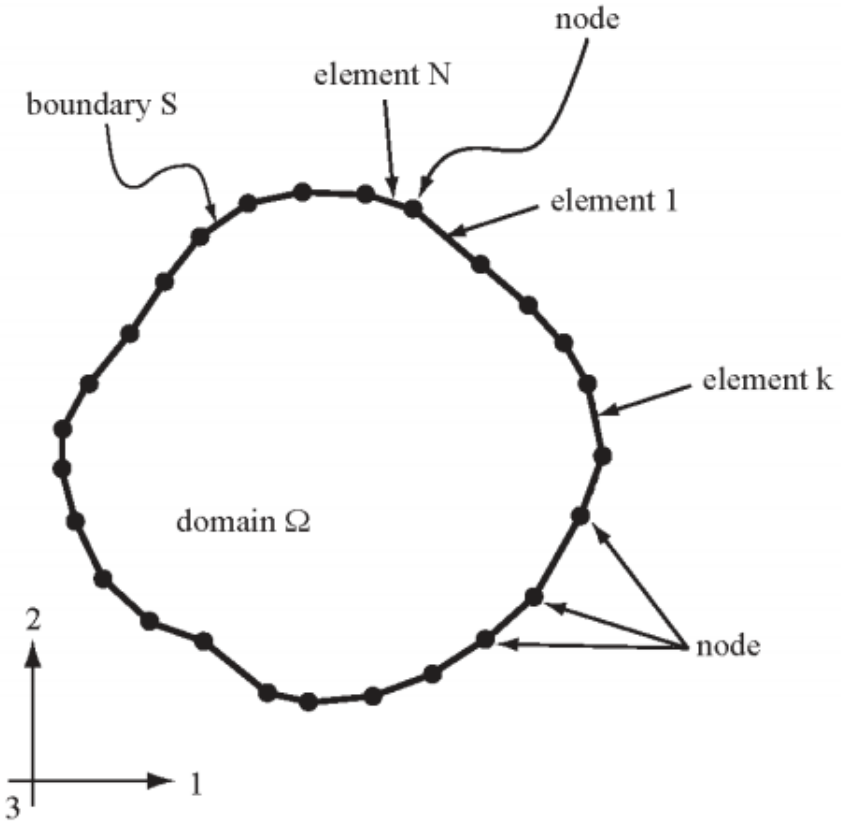

Figure 2.15 Example of discretization with boundary elements in 2D (Bobet 2010)

BEM formulations are particularly well-suited to address static continuum problems with small boundary-to-volume ratios, elastic behavior, and stresses or displacements applied to the boundaries. Challenges associated with BEM include representing angular boundaries and appropriate boundary integral equations which cause large and dense matrices to be solved (Costabel 1987).

d) Finite Difference Methods (FDM)

The FDM is generally based on the premise in which finite differences can adequately represent governing differential equations. According to Timoshenko and Goodier, the FDM was first developed by Runge in 1908 for torsion problems in solid mechanics (Timoshenko and Goodier 1982). In 1964, Southwell developed the relaxation method to solve the system of equations faster which promoted the use of the FDM. As an example, Figure 2.16 shows how the FDM is used to solve a problem on a grid superimposed on a domain (Bobet 2010).

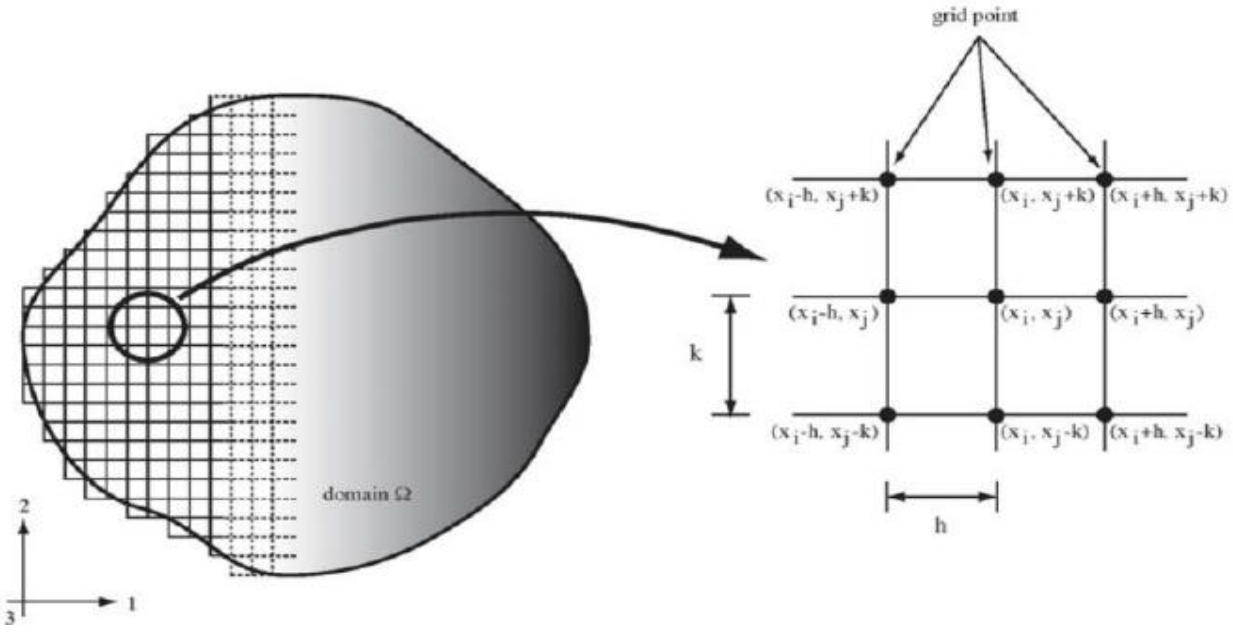

Figure 2.16 Finite difference grid in 2D (Bobet 2010)

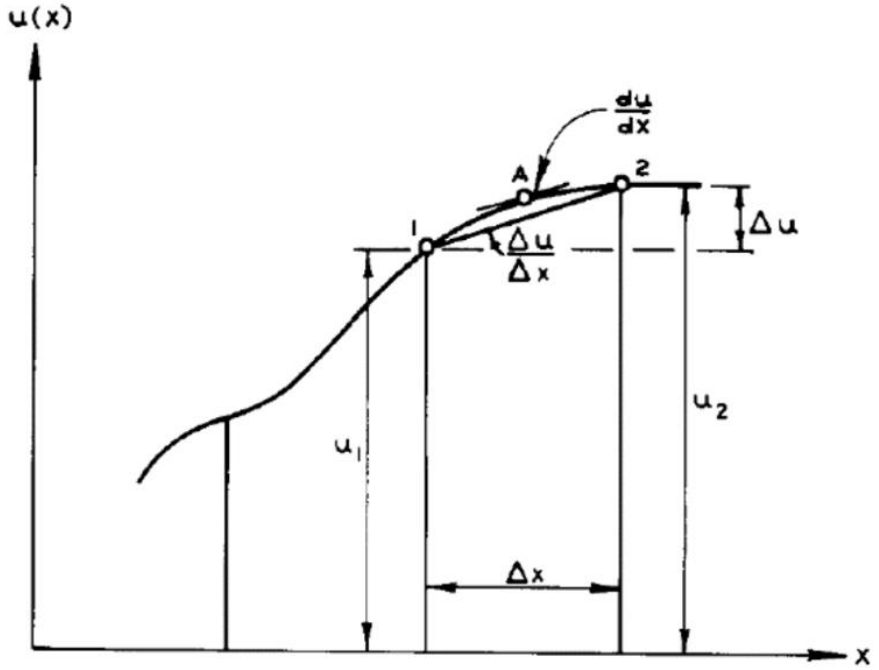

Figure 2.17 Finite difference approximation to the first derivative (Desai and Christina 1979)

Figure 2.17 illustrates how the FDM can be represented by Equation (2.13), in which the differential equation $\frac{du}{dx}$ is converted to the difference equation $\frac{\Delta u}{\Delta x}$ (Desai and Christian 1979).

$$\frac{du}{dx} = \lim_{\Delta x \to 0} \frac{\Delta u}{\Delta x} \approx \frac{\Delta u}{\Delta x} \tag{2.13}$$

After the replacement, three basic approximations to the first derivative can express the differentials of a function u(x):

$$\text{Forward difference: } \frac{du}{dx} = \frac{u_{i+1,j} - u_{i,j}}{\Delta x} + O(\Delta x) \tag{2.14}$$

$$\text{Backward difference: } \frac{du}{dx} = \frac{u_{i,j} - u_{i+1,j}}{\Delta x} + O(\Delta x) \tag{2.15}$$

$$\text{Central difference: } \frac{du}{dx} = \frac{u_{i+1,j} - u_{i-1,j}}{2\Delta x} + O(\Delta x)^2 \tag{2.16}$$

The FDM can efficiently handle complex nonlinear material behavior such as laterally loaded piles, one-dimensional consolidation, two and three-dimensional seepage (Bobet 2010; Desai and Christian 1979) and solve time-dependent problems (Nikolić et al. 2016). However, it is difficult to model arbitrarily shaped domains with the FDM (Desai and Christian 1979). When the configuration of a domain is simple (e.g., rectangular), the mesh points can be adjusted to coincide with the boundaries. For an irregular boundary, the mesh points may not fall on the boundary. Therefore, it is necessary to improve the FDM to remedy these shortcomings.

e) Finite Element Method (FEM)

The FEM has been used in many fields in geotechnics and is widely applied in electromagnetics, mechanical, and aerospace engineering. The FEM represents a body or a structure by an assemblage of subdivisions called finite elements (Potts and Zdravković 1999). These elements are connected at nodes. Currently, the FEM is the most commonly used method to analyze continuous or quasi-continuous media. Figure 2.18 shows that both the boundary and interior region are discretized into small finite elements that are connected by lines at the nodes.

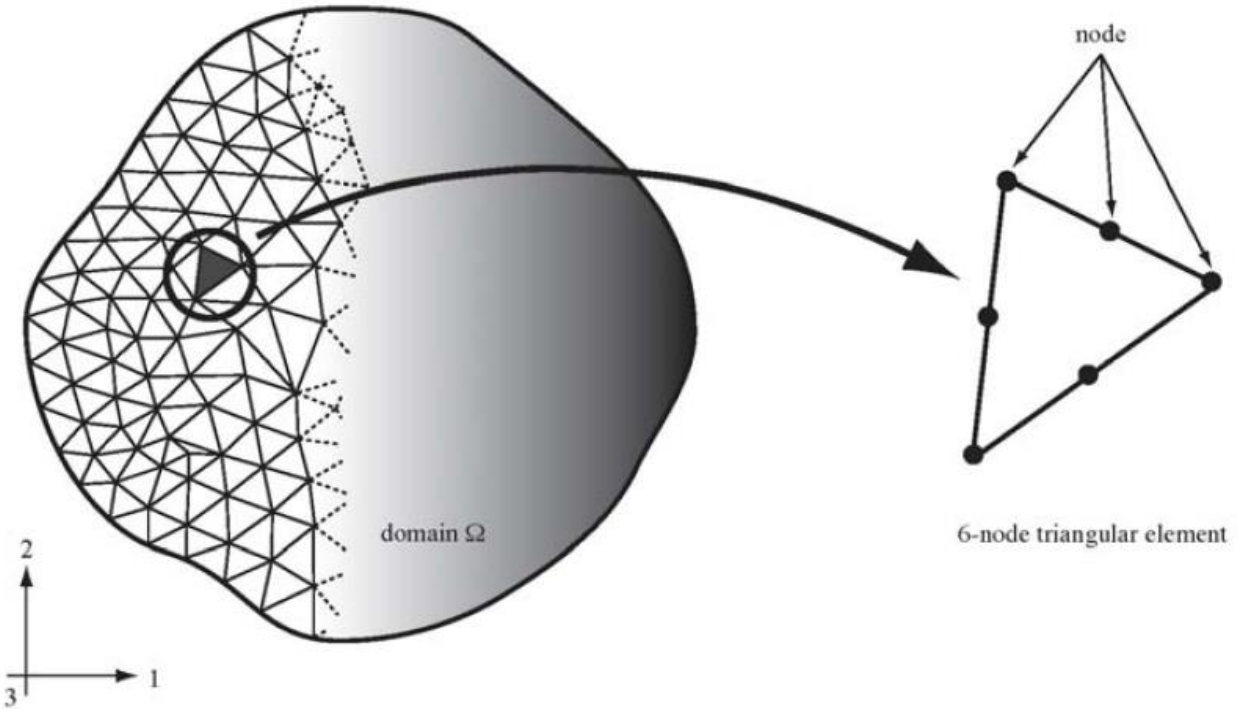

Figure 2.18 Finite element discretization in 2D (Bobet 2010)

The FEM can be formulated using the following six basic steps, as introduced by Desai and Christian (1979):

1) Discretizing the domain. The discretization divides the domain into smaller finite elements, including nodes on element boundaries or within an element. These finite elements assemble into an equivalent mesh, which represents the geometry of a problem. As shown in Figure 2.19, in two-dimensional finite element analysis, the triangular and quadrilateral elements are commonly used.

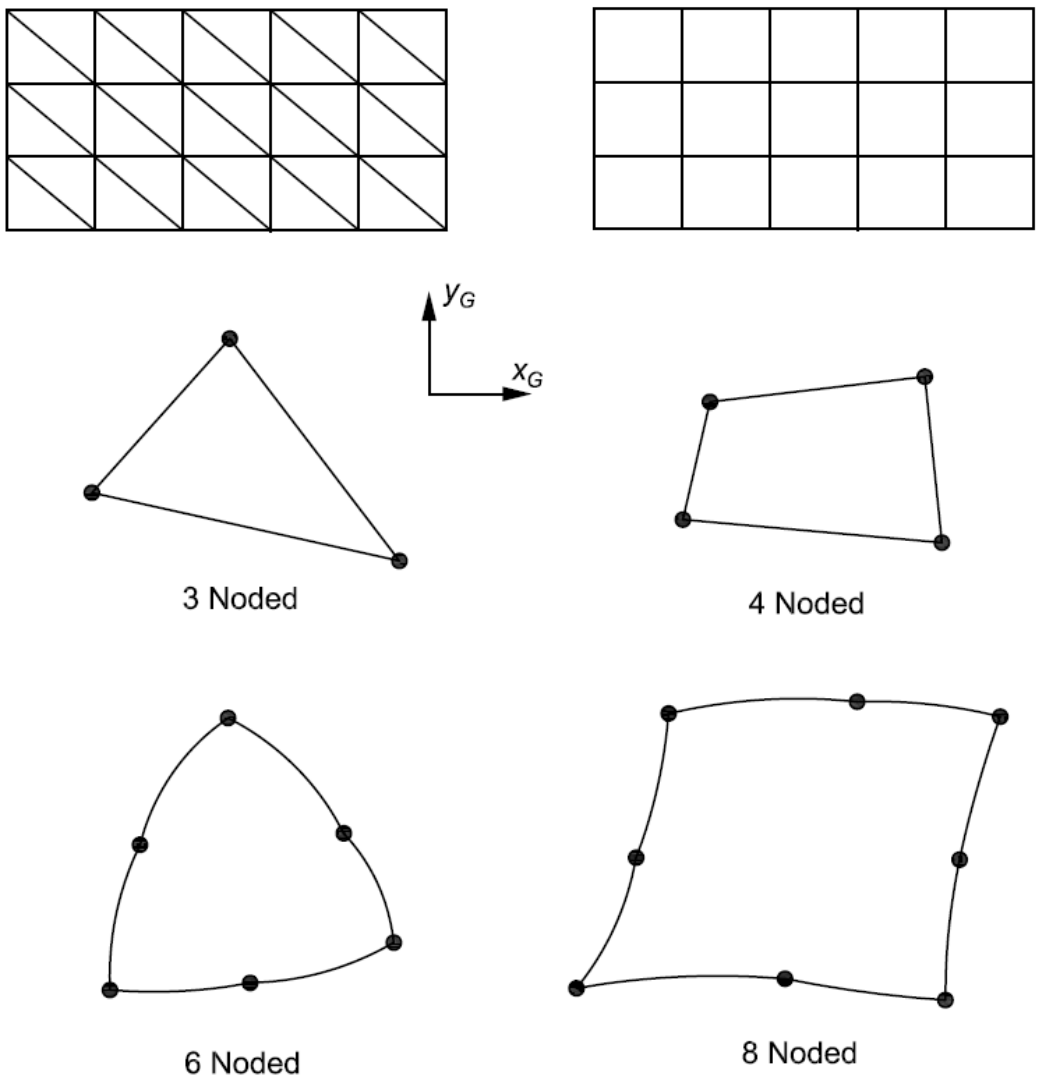

Figure 2.19 Typical two-dimensional finite elements (Desai and Christian 1979)

2) Primary variable approximation (displacement approximation): the primary unknown quantity in displacement-based FEM is the displacement field, which varies over the model domain. Select a primary variable (e.g., displacement, stress, etc.) and express it with approximation functions (such as interpolation functions, displacement functions, etc.)
3) Deriving element equations. Element equations govern the deformation behavior of each element. These equations define the properties of a finite element by using variational principles as shown in Equation (2.17)

$$[K_E] * \{\Delta d_E\} = \{\Delta R_E\} \tag{2.17}$$

where $[K_E]$ is the element stiffness matrix; $\{\Delta d_E\}$ is the vector of incremental element nodal displacements, and $\{\Delta R_E\}$ is the vector of incremental element nodal forces.

4) Assembling the element properties to form global equations. After defining the elements in a structure, the element properties are combined to get a stiffness relationship for the entire system. The stiffness relation for the entire body is expressed as:

$$[KG] * \{r\} = \{R\} \tag{2.18}$$

where $[K]$ is global, or assembled, stiffness matrix; $\{r\}$ is global nodal displacement vector; $\{R\}$ is global nodal force (forcing-parameter) vector.

5) Modifying boundary conditions: applying boundary conditions defined by load and displacement conditions helps set up the global system.
6) Computing the primary and secondary quantities. This is achieved in two steps:
    - Determining the nodal displacements by solving simultaneous linear algebraic equations.
    - Obtaining element strains through nodal displacements and the element displacement field interpolation, then stress and strains as the secondary quantities can be evaluated.

2.5.2 Advantages of FEM in Slope Stability Analysis

Slope stability represents an area of geotechnical analysis in which a nonlinear FEM offers real benefits over the existing methods, particularly when compared to LEM. Compared with traditional LEM, the advantages of FEM can be written as (Griffiths and Lane 1999):

- The location or shape of the failure surface is not assumed.
- FEM does not use slices and eliminates the need to assume the slice's side.
- More information can be provided in practical soil compressibility analysis, such as deformations of stress levels.
- FEM can monitor progressive failure up to and including overall shear failure.

The application of FEM in geotechnical analysis has become more widespread with the recent improvements in computer performance. The FEM possesses several benefits compared to other numerical methods:

1) Model with slopes with a high degree of fidelity owing to its ability to capture complex geometry, sequences of loading, presence of material or reinforcement, the action of water, and constitutive laws for complex soil behavior.
2) Easily observe the deformations of soils (Matthews et al. 2014).

In light of the aforementioned advantages, the FEM is chosen to conduct slope stability analyses in this thesis. The factor of safety (FS) plays an important role in slope stability analysis since it indicates how likely a slope is to fail. The Shear Strength Reduction (SSR) technique enables the FEM to calculate FS for slopes. Finite element analysis is used to compute stresses and displacements, which cannot directly be used to determine the stability of the slope. The SSR technique makes it possible for users to visualize of how a given slope fails and predict the stresses and deformations of support elements (such as piles, anchors, and geotextiles at failure) (Hammah et al. 2005a).

2.5.3 Finite Element Shear Strength Reduction Method

This section describes the finite element shear strength reduction (FE-SSR) method and how it is used to calculate the factor of safety (FS) of a given slope.

The finite element shear strength reduction (FE-SSR) method is frequently employed to solve slope stability problems, such as stability problems in blocky rock masses (Hammah et al. 2007a) and the determination of serviceability-based slope FS (Hammah et al. 2007b).

The SSR method was first introduced by Zienkiewicz et al. (1975). Since then, several researchers used the SSR (shear strength reduction) method in their study, such as Naylor (1982), Donald and Giam (1988), Matsui and San (1992), Ugai and Leshchinsky (1995), Dawson et al. (1999), Griffiths and Lane (1999), Song (1997), Zheng et al. (2005) and others. Among these works, Matsui and San (1992) validated the SSR (shear strength reduction) method in the finite element slope stability study.

FE-SSR methods assess the factor of safety (FS) by systematically reducing the shear strength of the soil and solving FEM models of the slope until deformations are unacceptably large or a non-converge situation occurs (Matsui 1988). The FS does not have a single definition (Abramson et al. 2001). In two-dimensional finite element slope stability analysis, the FS generally defined as follows (Kainthola et al. 2013):

1) the strength reserving definition, which defines the FS as the factor by which the soil's shear strength would have to be divided in order to put the slope into critical equilibrium (Duncan 1996),
2) the overloading is defined as the ratio of total resisting forces to total driving forces along a specific slip line, with FS being the result (Farias and Naylor 1998).

In the SSR, the FS is determined by looking for the stress reduction factors (SRFs) which are calculated using finite element analysis and bringing the slope to the brink of failure. Additionally, this method usually relies on the Mohr-Coulomb model to define the strength of the materials. As such, the factored shear strength parameters are defined as (Cheng and Lau 2014):

$$c^* = \frac{c}{F} \; ; \; \emptyset^* = \arctan\left(\frac{tan\emptyset'}{F}\right) \tag{2.19}$$

where $c^*$and $\emptyset^*$ are the shear strength parameters, and F is the SRF.

The following equation describes the reduced shear strength of a Mohr-Coulomb material:

$$\frac{\tau}{F} = \frac{c'}{F} + \frac{\sigma tan\emptyset'}{F} \tag{2.20}$$

where τ is the shear strength, and σ is the normal stress, which can be written as:

$$\frac{\tau}{F} = c^* + \sigma tan\emptyset^* \tag{2.21}$$

The main steps for determining the FS (or the critical SRF) of a slope by using the FE-SSR method are (Hammah et al. 2007a):

1. Create a finite element model of a slope using strength properties. Then analyze the model and record the maximum total deformation.

2. Repeat the previous step to calculate factored Mohr-Coulomb material parameters by increasing the value of F (SRF) in Equation (2.19). Input the new strength properties into the model, rerun the analysis, and record the maximum total deformation.
3. Repeat step 2 until the finite element model cannot converge to a solution. Terminate the calculation if one of the following situations occurs (Cheng and Lau 2014):
   - The non-linear equation solver does not converge after a pre-defined maximum number of iterations.
   - The change rate of displacement in the system shows a sudden increase.
   - A failure mechanism has developed.

Cheng and Lau (2014) found that the failure mechanism of a slope can be identified by the contour of the maximum shear strain or the maximum shear strain rate. Figure 2.20 (a) shows the contours of maximum shear strain for a failed slope, and (b) the location of a critical failure surface in a slope analyzed with the FE-SSR method.

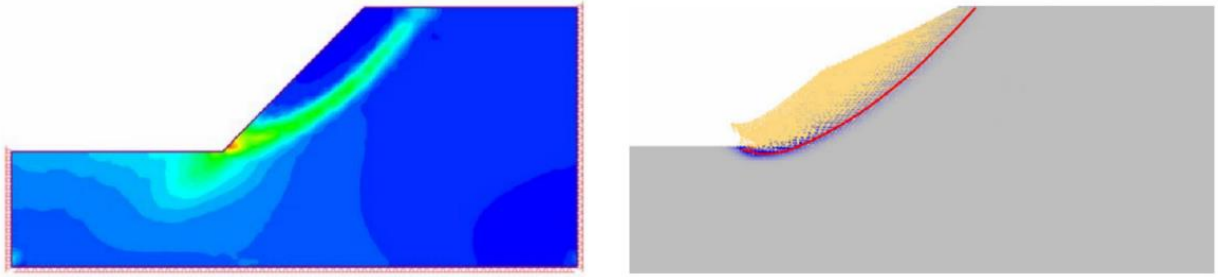

(a) (b)

Figure 2.20 (a) Contour of the maximum shear strain (Hammah et al. 2005b), and (b) the failure mechanism by FE-SSR method (Cheng et al. 2007)

2.5.4 Convergence Criteria

There are various criteria used to evaluate the convergence of the finite element analysis, for example, limiting the shear stress on the potential slip surface (Duncan and Dunlop 1969), tests of bulging of the slope (Snitbhan and Chen 1976), and the non-convergence of a solution (Zienkiewicz et al. 1977). Non-convergence is an appropriate indicator of slope failure. In this thesis, the RS2 software is used. RS2 uses a non-linear spring subjected to a single force to represent the finite element solution process, the convergence criteria, and the iteration stopping criterion (Rocscience Inc. 2019). The relationship between the applied load P and displacement U is:

$$K * U = P \tag{2.22}$$

where $K = K(U)$ is the non-linear stiffness of the spring, which is also a function of displacement.

Figure 2.21 shows the non-linear response of a spring to loads.

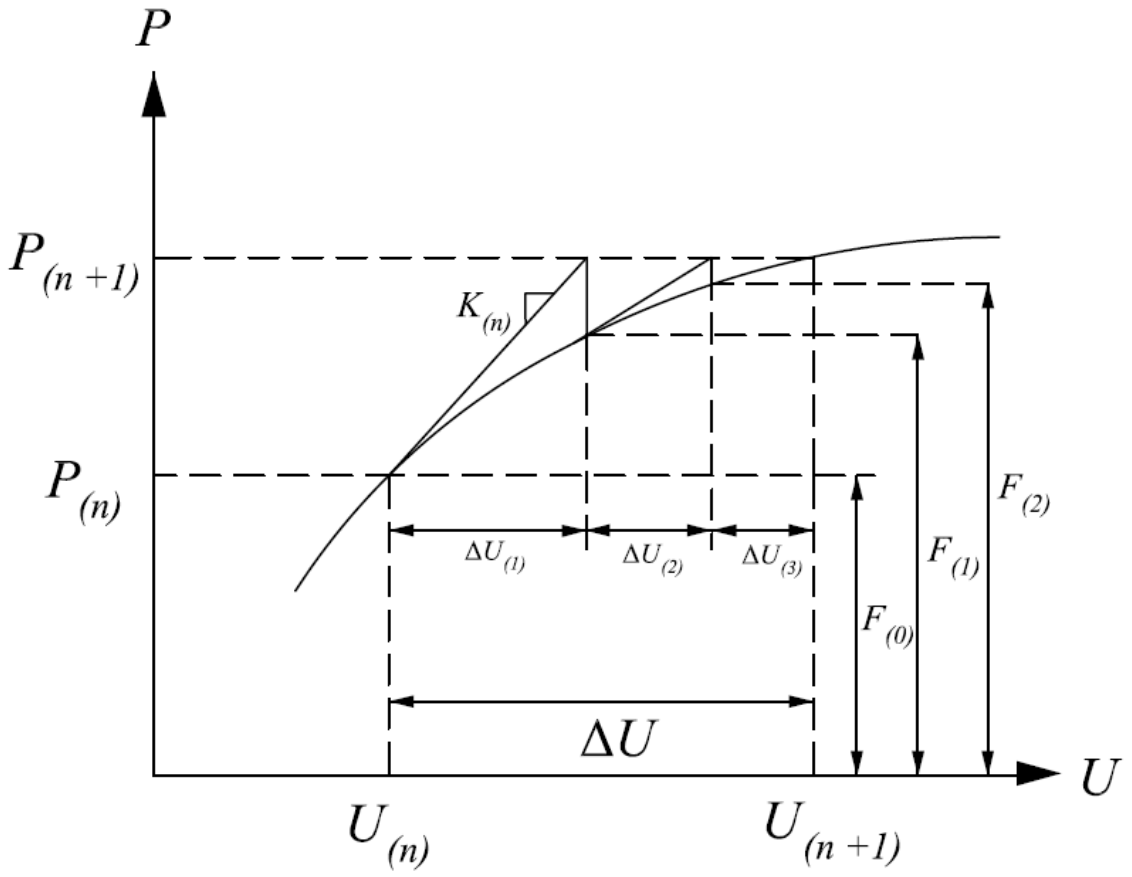

Figure 2.21 The non-linear response of a spring to applied load (Rocscience Inc. 2019)

According to Figure 2.21, the process of finite element solution can be expressed as follows: The first assumption is that the displacement $U_{(n)}$ is set after applying the load step $P_{(n)}$ to the spring. The internal force or resisting force of the spring is $\mathrm{F}(0)$, which is in equilibrium with $P_{(n)}$. The displacement increment ΔU occurs in response to a new load $P_{(n+1)}$. The key is to update displacement $\mathrm{U(n+1)}$ to approach the real solution. To do so, the tangent stiffness $K_{(0)}$ at the initial point ($U(n)$, $P(n)$) of the curve is evaluated. Then, the first displacement increment $\Delta U_{(1)}$ can be determined and $F_{(1)}$,i.e., the internal force of the spring, is obtained at the point $\Delta U_{(n+1)} = U_{(n)} + \Delta U_{(1)}$. At this stage, the load imbalance (or the current force error) $P_{(n+1)} - F_{(1)}$ is quite large, as displayed in Figure 2.21. The main goal of all iterations in FEM analysis is to reduce the load imbalance to zero. So, for the next iteration, starting at the updated displacement $U_{(n+1)}$, apply the same load $P_{(n+1)}$ and obtain the displacement increment $U_{(2)}$ and internal force $F_{(2)}$to update the point to $\Delta U_{(n+1)} = U_{(n+1)} + \Delta U_{(2)}$. The load imbalance $P_{(n+1)} - F_{(2)}$ becomes smaller than in the first iteration. As the iteration process continues, the displacement increments and load imbalance all approach zero. To avoid unnecessary iterations, stopping criteria need to be implemented to reduce the processing time when the results are sufficiently close to the true solution.

In RS2, absolute force and energy are both considered. Equation (2.23) and Equation (2.24) represent these two criteria and are as follows:

$$\text{The absolute force: } \left\| \frac{(P_{(n+1)} - F_{(i)})}{P_{(n+1)}} \right\| < (\text{specified tolerance}) \tag{2.23}$$

The energy convergence is satisfied when:

$$\left\| \frac{\Delta U_{(i)}^{T} (P_{(n)} - F_{(i)})}{\Delta U_{(0)}^{T} (P_{(n)} - F_{(0)})} \right\| < (\text{specified tolerance}) \tag{2.24}$$

where i=0,1,2…n is the iteration number.

Checking both the force and energy criteria helps avoid false convergence. The physical meaning of the absolute force criterion is the imbalance related to the new load reduced to a certain level. On the other hand, the absolute energy criterion considers the displacement, which means that the iteration will stop when the current displacement increment is sufficiently smaller than the initial displacement.

2.5.5 The Factor of Safety (FS) Determination

The most significant aspect in determining slope stability is the factor of safety. The FS of a slope is defined as the ratio between the shear strength of the slope's soil and the shear stress (Duncan et al. 2014). Theoretically, a FS $<$ 1.0 indicates that the slope is not stable and that failure is imminent. And FS $>$1.0 means the slope is stable. However, for the construction and design of earth or rockfill dams, the factor of safety is normally based on experience since the variables chosen to compute the FS may not be accurate. Table 2.15 summarizes appropriate factors of safety for different types of slopes and analysis conditions.

Table 2.15 Factor of safety for different loading in earth and rockfill dams (Hoek 2007)

Loading condition	S.F.	Remarks
End of construction porewater pressures in the dam and undissipated porewater pressures in the foundation. No reservoir loading.	1.3	
Reservoir at full supply level with steady state seepage in the dam and undissipated end-of-construction porewater pressures in the foundation.	1.3	Possibly the most critical (even if rare) condition.
Reservoir at full supply level with steady state seepage.	1.5	Critical to design.
Reservoir at probable maximum flood level with steady state seepage conditions.	1.2	
Rapid reservoir drawdown from full supply level to minimum supply level.	1.3	Not significant in design. Failures very rare and, if they occur, usually shallow.

With proper design and construction considerations (such as drainage, compaction, and elimination of weak areas), a factor of safety (FS) for a railway embankment ranging from 1.3 to 1.5 is usually acceptable (Li et al. 2016). Therefore, in this study, a minimum FS of 1.3 is used to ensure adequate slope performance.

2.6 Constitutive Models for Soils

This section discusses the background information on elastic and elastic-plastic soil models including the Mohr-Coulomb model.

2.6.1 Elastic Soil Model

The basic physical meaning of stresses and strains for a linear, isotropic, elastic soil is explained by Hooke's law. For a general state of stress (Figure 2.22), The elastic stress-strain constitutive equation (Equation (2.25)) for Hooke's law is as follows (Punmia et al. 2005):

$$\begin{Bmatrix} \varepsilon_x \\ \varepsilon_y \\ \varepsilon_z \\ \gamma_{1xy} \\ \gamma_{1yz} \\ \gamma_{1xz} \end{Bmatrix} = \frac{1}{E} \begin{bmatrix} 1 & -v & -v & 0 & 0 & 0 \\ -v & 1 & -v & 0 & 0 & 0 \\ -v & -v & 1 & 0 & 0 & 0 \\ 0 & 0 & 0 & 2(1+v) & 0 & 0 \\ 0 & 0 & 0 & 0 & 2(1+v) & 0 \\ 0 & 0 & 0 & 0 & 0 & 2(1+v) \end{bmatrix} \begin{Bmatrix} \sigma_x \\ \sigma_y \\ \sigma_z \\ \tau_{xy} \\ \tau_{yz} \\ \tau_{xz} \end{Bmatrix} \tag{2.25}$$

In this matrix, ε and σ are the strains and normal stresses in the X, Y, Z directions respectively, γ_1 and τ are the shear strains and shear stresses in the XY, YZ, and XZ planes, respectively, E is the elastic (or Young's) modulus, and v is Poisson's ratio.

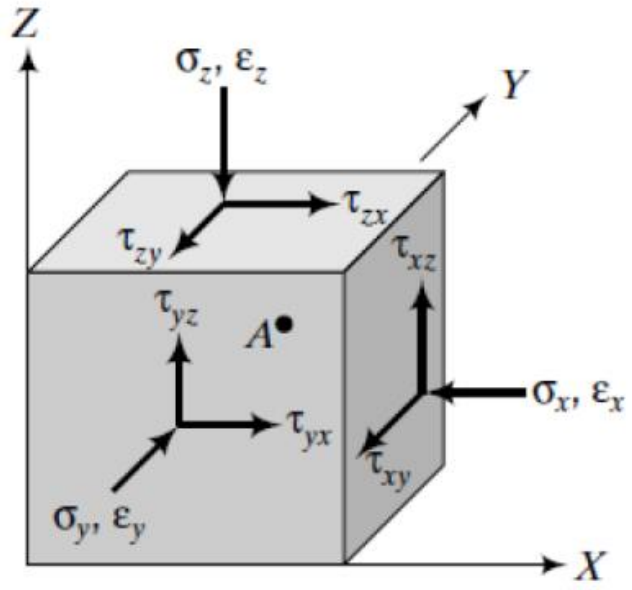

Figure 2.22 General 3D state of stress (Punmia et al. 2005)

Out of these three parameters: Young's modulus, Poisson's ratio, and shear modulus, only two are needed when the problem deals with a linear, isotropic, elastic soil. For example, the shear modulus can be determined from Young's modulus and Poisson's ratio with Equation (2.26).

$$G = \frac{E}{2(1+v)} \tag{2.26}$$

Hooke's law is a basic elastic theory. It is too simplistic for use in high stress and strain conditions where soil non-linearity is likely to occur. As a result, several nonlinear elastic models have been developed, such as Duncan-Chang elastic model, Cauchy elastic model, Green elastic model (hyper-elastic theory), hypo-elasticity model, etc. (Li 2004).

2.6.2 Elastic-plastic Soil Model (Mohr-Coulomb Model)

Although there are elastic and elastic-plastic soil constitutive, in this research, the elastic-plastic model is used to represent soil behavior since it is more physically accurate. Various elastic-plastic models have been developed, including classic elastic-plastic models (e.g., Tresca and von Mises, Mohr-Coulomb, Drucker-Prager models, etc.) and advanced elastic-plastic models (e.g., Lade-Duncan model, Bounding surface models, MIT soil models, Bubble models, etc.) (Chen and Mizuno 1990). Since the advanced models require site-specific parameters from the laboratory, the classic model is adopted in this thesis.

The classical elastic-plastic model is defined by four components (Bertram and Gluge 2013):

1) An elastic law, which defines the soil's elastic behavior prior to yielding. Hooke's law is utilized to model elastic deformation in this study.
2) A yield criterion that characterizes the elastic limit of the soil such as a yielding function and surface. Before yielding, the mechanical behavior of the soil is considered elastic, and after yielding, the soil behavior is determined by several plastic failure criteria, as shown in Figure 2.23. The yield relationship is explained by the following equations (Punmia et al. 2005):

$$f(\sigma_{ij}) = 0 \;\; Yeild \tag{2.27}$$

$$f(\sigma_{ij}) < 0 \;\; Elastic\ State \tag{2.28}$$

where σ_{ij} is the state of stress.

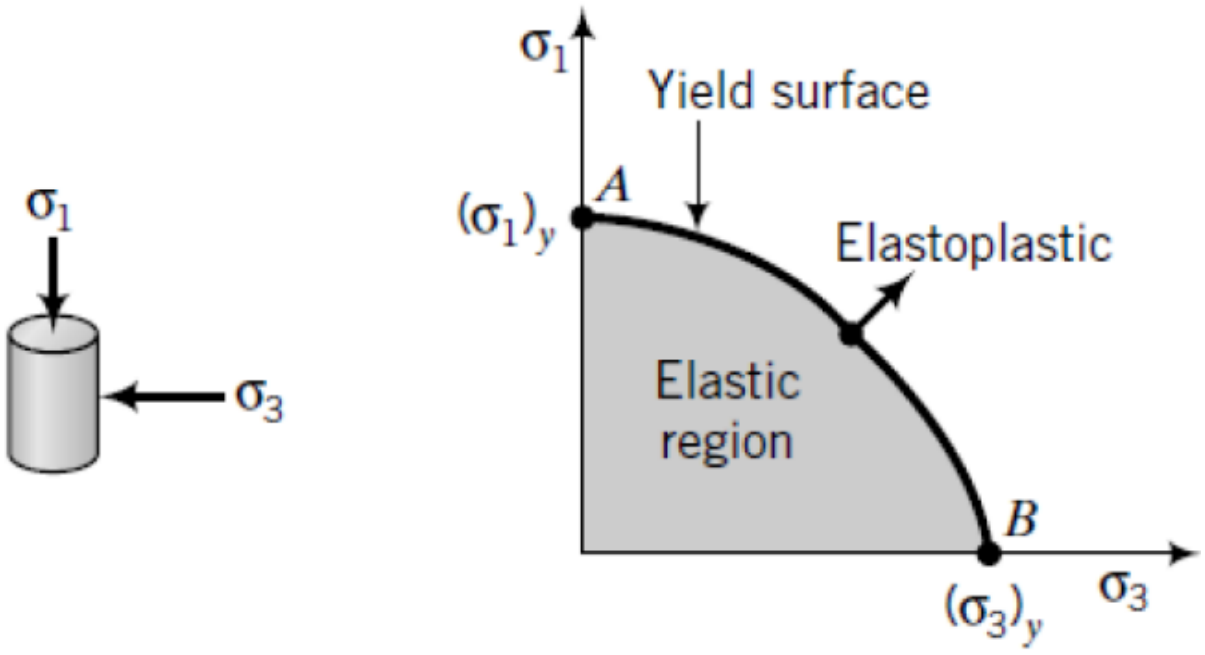

Figure 2.23 Elastic, yield, and elastoplastic stress state (Punmia et al. 2005)

Figure 2.24 shows how stresses respond to straining in an ideal plastic model (elastic-perfectly plastic model). The material yields when the stress reaches the yield stress σ_y. As the strain increases past the yield point, the stress remains σ_y. Overall, the stress state always satisfies $f(\sigma_{ij})$=0 during plastic flow (Pietruszczak 2010).

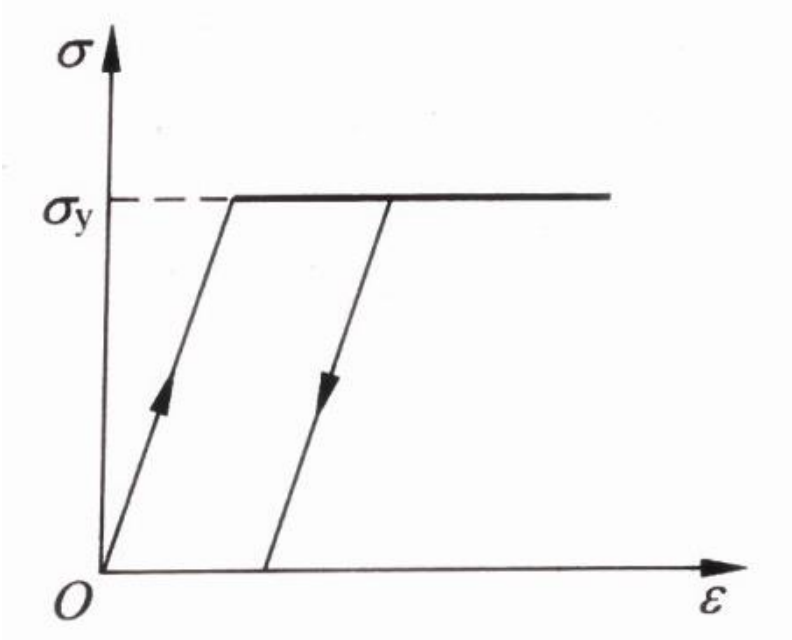

Figure 2.24 Elastic-perfectly plastic stress-strain behavior (Pietruszczak 2010)

This section focuses on the Mohr-Coulomb model which assumes the soil is an ideal plastic material (elastic-perfectly plastic model). Coulomb, in 1773, proposed a linear relationship between the shear strength and the normal stress on a plane. The shear stress is a function of the normal stress (Pietruszczak 2010):

$$\tau = f(\sigma) \tag{2.29}$$

$$\tau = c - \sigma tan\emptyset \tag{2.30}$$

where τ is the shear strength, σ is the normal stress, c is the cohesion, and $\emptyset$ is the friction angle. The Mohr circle representation combines Equation (2.30) to formulate a general mathematical criterion. At the failure state, (see Figure 2.25), the circle becomes tangential to Coulomb's envelope, and the state of shear stress and normal stress at failure can be determined as:

$$\tau = \frac{1}{2}(\sigma_1 - \sigma_3)cos\emptyset \tag{2.31}$$

$$\sigma = \frac{1}{2}(\sigma_1 + \sigma_3) + \frac{1}{2}(\sigma_1 - \sigma_3)sin\emptyset \tag{2.32}$$

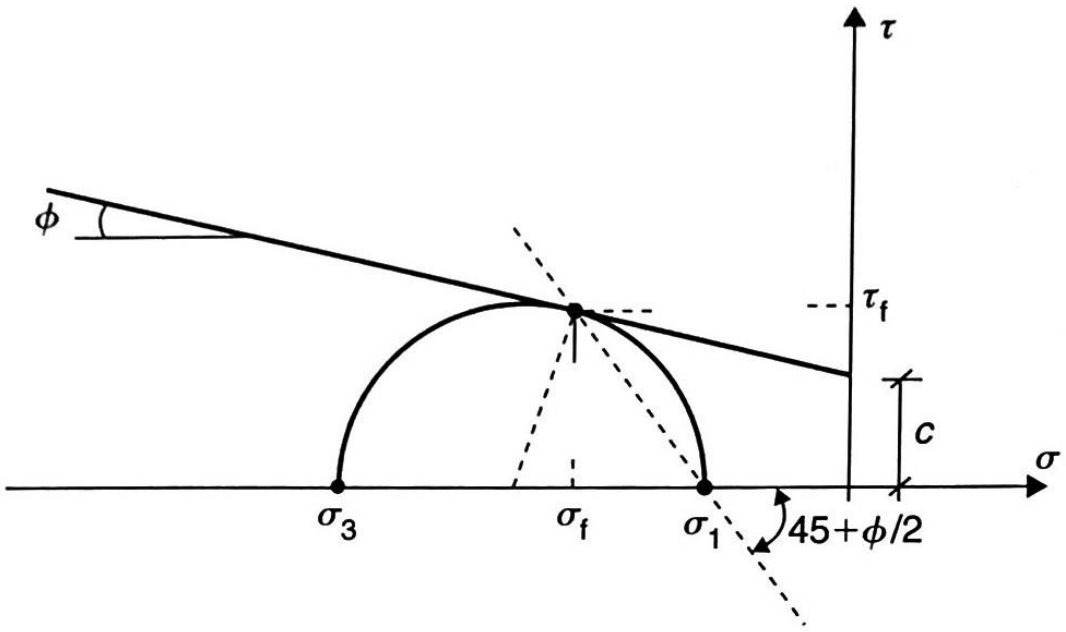

Figure 2.25 Mohr circle defining the failure condition (Pietruszczak 2010)

For an elastic-perfectly plastic material, yield occurs when the material is failing. Combining Equations (2.31) and (2.32), the well-established Mohr-Coulomb yield surface for $\sigma_1 > \sigma_2 > \sigma_3$ can be expressed as (Pietruszczak 2010):

$$F = \frac{1}{2}(\sigma_1 - \sigma_3) + \frac{1}{2}(\sigma_1 - \sigma_3)sin\emptyset - ccos\emptyset \tag{2.33}$$

Figure 2.26 shows the corresponding yield surface of the Mohr-Coulomb criterion in principal stress space.

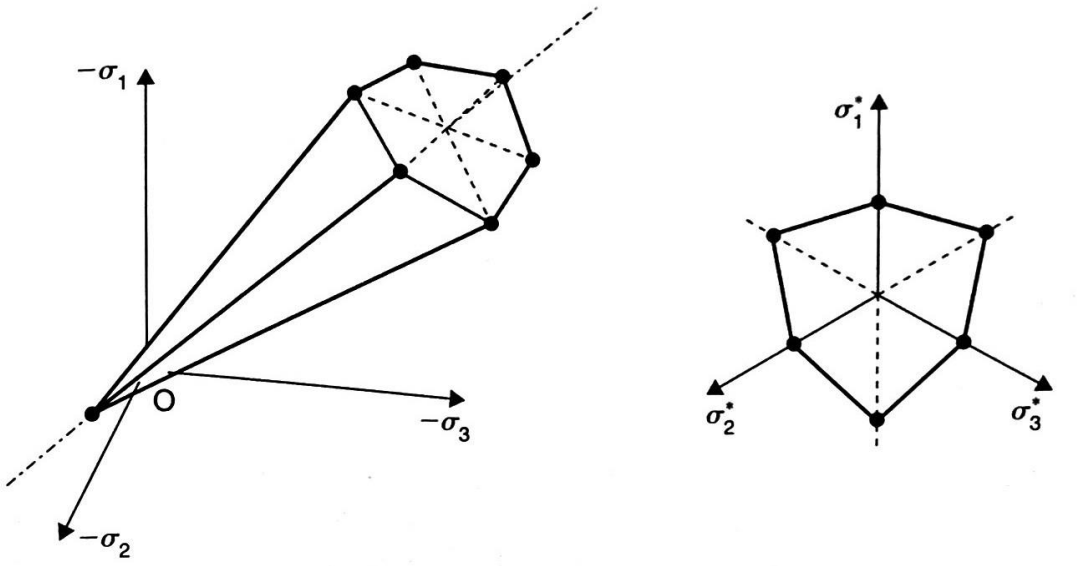

Figure 2.26 Mohr-Coulomb criterion in the principal stress space (Pietruszczak 2010)

3) A flow rule, which defines how plastic deformation develops during yielding. When the plastic potential function is the same as the yield function of a Mohr-Coulomb model, the flow rule said to be an associated flow rule, and on the contrary, it is called a non-associated flow rule.
4) A hardening rule describes the evolution of the hardening or softening during yielding. The yielding surface will expand (hardening) after the initial yielding according to the applied hardening rules until failure occurs. For perfect plasticity, there will be no hardening or softening law influencing the soil.

Chapter 3 Generation of the Slope Stability Numerical Model

3.1 Introduction

This chapter presents the generation of numerical models based on the literature reviewed in the previous chapter. The finite element models are verified by comparing the results of the numerical analysis with data published in the literature. Since the main goal of the research is not to study the rail-tie system or the track superstructure, the train loads on the tie-ballast interaction surface in all models are calculated manually and applied as loading. Section 3.2 shows the process of creating each part of the model, such as external train loading, natural slope and water conditions, and track substructure. Section 3.3 discusses the verification of the numerical model which is achieved by comparing results generated using RS2 with those of a similar case study published in the literature.

3.2 Model Generation

The first step to build a model with RS2 is to calculate the train loads at the tie-ballast interface and select the parameters of the track superstructure (rail type, track dimensions, and axle information). The next step is to determine the dimensions of the track substructure. The applied loads and groundwater conditions are then defined. The completion of the previous steps allows for the model's geometry to be specified which in turns requires the definition and assignment of material properties and boundary conditions as well as the generation of the mesh.

3.2.1 Track Design and Loading Conditions

The train model consists of a typical locomotive since it is heavier than a conventional freight car and is deemed to represent a more critical case. The locomotive has a wheel load of 157.61lbs. (35,432kN) (Esveld 2001), and a wheel diameter of 42 inches (1.07m), which correspond to the most often used type of locomotive in Canada (GE C44-9W) (AREMA 2010). Table 3.1 lists the dimensions of the track and the information about the axle loads, including rail gauge, tie width, length, height, and spacing, the axles number per car, axle load per wheel.

Table 3.1 Parameters of the locomotive and track superstructure

Parameter	Value
Axles number per car	6
Axle load per wheel (kN)	35,432
Wheel diameter (m)	1.07
Rail gauge (m)	1.435
Tie width (m)	0.229
Tie length (m)	2.590
Tie height (m)	0.150
Tie spacing (m)	0.495

In this thesis, the train loads are calculated manually and applied at the bottom of the sleeper (the top of the ballast). The following assumptions are made to simplify the computational procedure used in this thesis:

- The track is assumed to be a straight (tangent) track, and the friction between the rail and wheel is ignored. The model is simplified by treating the embankment as a two-dimensional plane-strain structure.
- The train stops (zero velocity) or runs with a constant speed through the straight track.
- The track, the rail, the wheels are all level and smooth.
- Wind and temperature factors are neglected.

The method for calculating the external force was previously discussed in Section 2.3.3. Figure 3.1 depicts the basic processes in load transmission from wheel to ballast. The axle load is transferred to the wheel load, then from the rail seat to the sleeper and ballast contact surface.

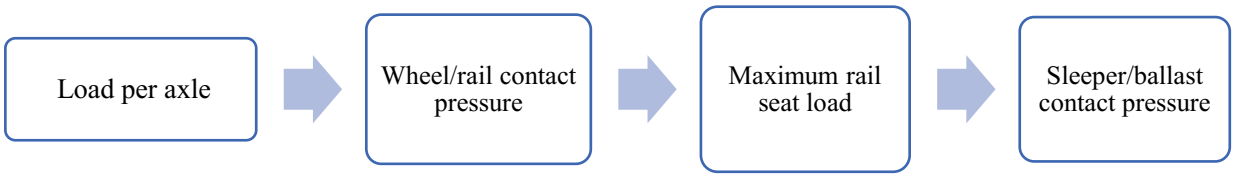

Figure 3.1 The process of load transmission

Based on the parameters listed in Table 3.1, the rest of the parameters (wheel load, impact factor, distribution factor, and average ballast pressure at the tie face) are calculated by the method provided by AREMA (2010). The impact factor and the average ballast contact pressure can easily be calculated by using different train speeds, as shown in Table 3.2. All units are converted to metric units for the sake of consistency.

Table 3.2 Average ballast pressure at tie face at different train speeds

Train speed	km/h	0	30	60	90	120
	mi/h	0	18	37	56	75
Impact factor	%	0	14	29	44	59
Distribution factor	%	44	44	44	44	44
Average ballast pressure at tie face	kPa	233.85	266.92	301.83	336.74	371.65

3.2.2 Geometry of the Numerical Model Including its Boundaries

After defining the track parameters and the load conditions, the next step is to define the model geometry. The embankment structure consists of the ballast, subballast, and subgrade and a pipe designed to provide drainage from the left side of the track to the right side, built on a natural clay layer. All dimensions are shown in Figure 3.2. According to AREMA's Manual for Railway Engineering (AREMA 2010) and the Railway Investigation Report (TSB 2013), the depth of the ballast, subballast, and subgrade layer is set as 0.5, 0.2, and 0.3m, respectively, which are common values for such railways. The diameter of the pipe is set to 0.8m, which is a typical railway drainage culvert diameter (Kitano et al. 2016), the ballast shoulder width (BSW) and roadbed berm width (RBW) are set to 0.45m and 0.7m, which provide the lateral resistance and confinement for the embankment. The side slopes of ballast, subballast, and subgrade have an inclination of 1V:2H (Calamak and Yanmaz 2016; Egeli and Usun 2012; Profillidis 2014). The ballast bearing pressure is applied at the bottom of the tie.

In the parametric study, the subgrade's depth is one of the variables, which makes the height of the railway embankment range from 1m to 5m. In addition, the inclinations of the side slopes of subballast and subgrade are treated as one variable, named the slope ratio, selected as 1V: 2H or 1V: 3H. Moreover, train speeds vary depending on the simulation case, resulting in varying uniform loads at the tie-ballast interface.

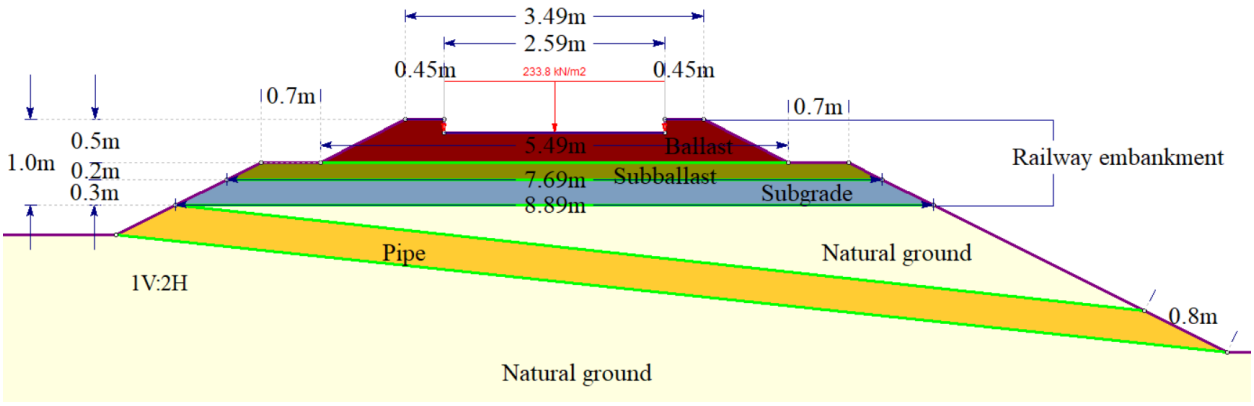

Figure 3.2 Cross-section of the railway embankment with dimensions

The next step is to identify the geometry of the natural ground under the railway embankment. The primary concerns are ensuring that the stress is not reflected in the model's outer boundaries and

the computational time. The cross-section of the numerical model with its dimensions is shown in Figure 3.3. Due to the variability of the subgrade and natural slope height, the dimensions of the natural ground foundation have the following relationships (Xu and Zsáki 2021):

- The length of the left and righthand side of the railway embankment (a, c) is at least the same length as that of the bottom of the whole slope (b) (Equation (3.1)) and greater than 1.5 times that of the bottom of the entire slope (b) (Equation (3.2)):

$$a \geq b \tag{3.1}$$

$$c \geq 1.5b \tag{3.2}$$

- On the righthand side, the natural ground height (f) is set to about four times the total height of both the railway embankment (d) and the natural slope (e), which can be expressed by Equation (3.3):

$$f \approx 4 \times (d + e) \tag{3.3}$$

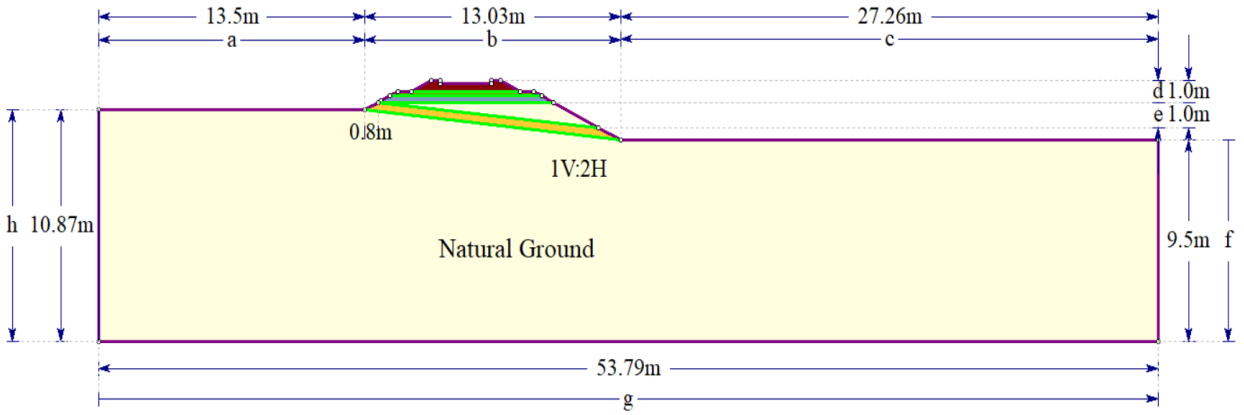

Figure 3.3 Cross-section of the numerical model with dimensions

3.2.3 Material Properties

For the substructure, the ballast layer is made of uniformly crushed stone. The subballast layer prevents intermixing of the ballast and subgrade, and is composed of gravel and sand. The subgrade layer is made of sand. When the pipe functions well, it should be empty. It is simulated by a high permeability material (gravel and sand) considering the numerical stability and continuity of 2D FEM models. When the pipe is clogged, it should be an impervious layer. However, the model is separated into two parts (railway embankment and nature ground foundation). Disjoined models may cause inaccurate results since the Biot theory treats a soil skeleton as an elastic solid with pore fluid flow coupled with the solid by the conditions of equilibrium and continuity. Therefore, a material with very low permeability is used to simulate the clogged pipe in this study. The natural ground consists of clay. Table 3.3 shows the material properties of the railway embankment layers, drainage pipe, and the natural ground soil used in this simulation. The values are taken from the ones presented in Chapter 2. All the layers are modeled as elastic-plastic materials, and the failure criterion is chosen to be Mohr-Coulomb.

Table 3.3 Material properties of the model

Name	Soil type	Unit weight	Porosity	Cohesion	Friction angle	Poisson's ratio	Young's modulus	Permeability
		kN/m^3	\	kPa	°	\	kPa	cm/s
Ballast	Crushed Stone	26	0.2	127,490	0	45	0.5	1.0×10^{-1}
Subballast	Gravel and Sand	24	0.3	196,130	0	35	0.5	1.0×10^{-3}
Subgrade	Sand	22	0.3	78,450	0	38	0.4	1.0×10^{-4}
Pipe	Coarse sand	25	0.3	98,070	0	45	0.5	1.0×10^{2}
Nature Ground	Sandy clay	18	0.3	21,000	31.5	21	0.3	1.0×10^{-6}

3.2.4 Mesh Convergence Study

A mesh convergence study is required to determine the proper mesh element density. For most models in this thesis, triangular elements with six nodes create a well-graded mesh. Six-noded triangles are generally more accurate than three-noded linear interpolation order elements. Although the mesh type is uniform, with triangles of similar size, the boundary discretization and element densities are manually increased in the embankment and in the potential sliding zone within the rectangular dashed box, as illustrated in Figure 3.4.

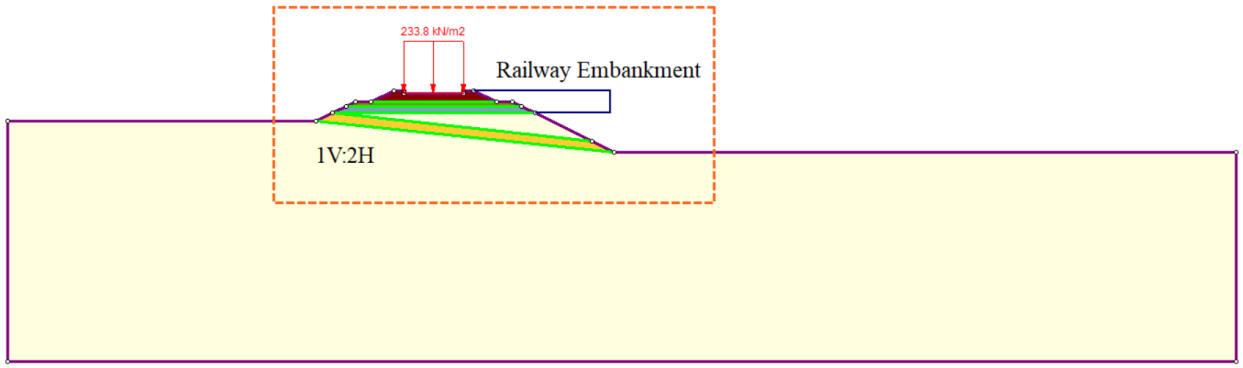

Figure 3.4 Area of the numerical model with higher boundary discretization and element densities

The mesh convergence study is used to compare how the mesh and discretization affect the accuracy of the finite element simulation results. A mesh is deemed adequate if the simulation results remain unchanged following an increase in the number of elements used in the model. This process is known as mesh convergence.

The numerical model shown in Figure 3.5 is discretized with about 500 elements to around 16,000 elements, with the number of elements being increased in each step by $2^n \times N$ ($n = 0, 1, 2 \ldots and\ N = 500$). Table 3.4 lists the corresponding FS value and computational time with a varying number of mesh elements. Table 3.4 also shows that the critical FS of the numerical model is 1.22, which is used as the criterion to calculate the differences in FS, illustrated by Equation (3.4):

$$FS_{error} = \frac{FS-1.22}{1.22} \tag{3.4}$$

Table 3.4 FS value and computation time corresponding to a different number of mesh elements of the numerical model

Number of Elements	FS value	FS difference (%)	Computation Time (min)
312	1.47	20.49%	3.76
476	1.31	7.38%	4.33
695	1.27	4.10%	5.78
982	1.25	2.46%	10.54
2158	1.23	0.82%	15.77
4137	1.22	0.00%	21.07
8213	1.22	0.00%	32.45
16091	1.22	0.00%	45.26

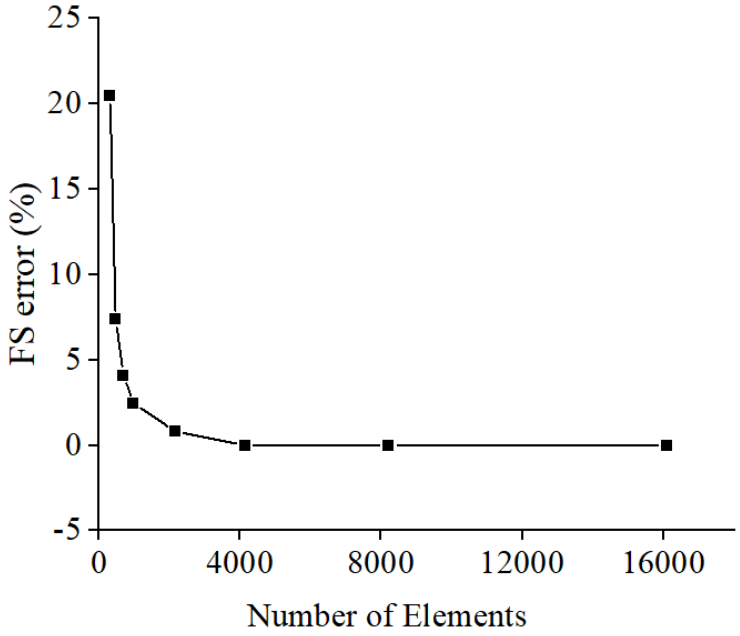

Figure 3.5 Critical mesh elements for the numerical model

The mesh converges at 4,137 mesh elements, where the FS difference curve reaches 0%, as shown in Figure 3.5 and Table 3.4.

3.2.5 Boundary Conditions

The boundaries in this numerical model are assigned to the bottom, left, and right sides. The bottom of the model is restrained in both the X and Y directions. The left and right sides are only restrained in the X direction with roller supports. The boundary conditions remain the same during the entire simulation process. Figure 3.6 shows a model with the appropriate boundary conditions.

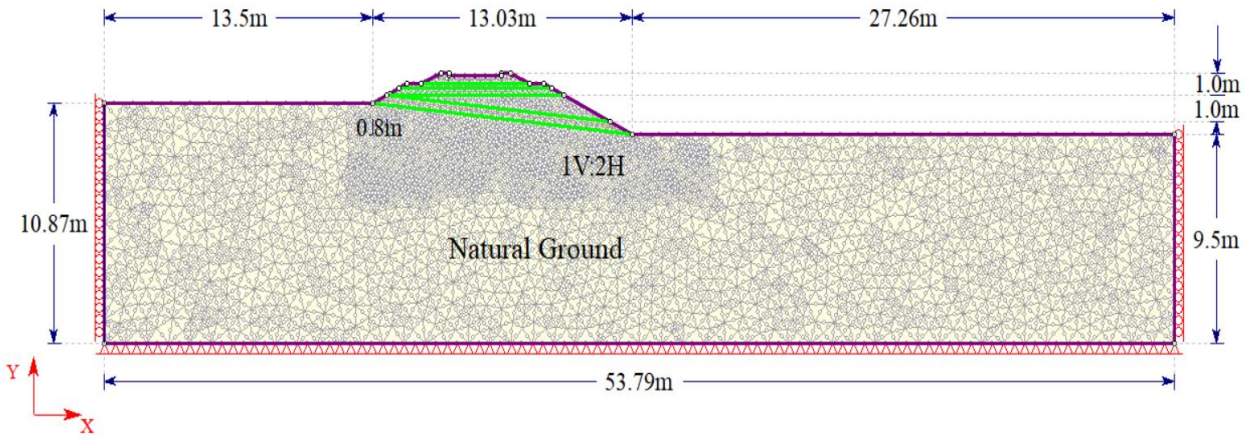

Figure 3.6 Cross-section of the complete model

3.3 Verification of the Numerical Model

The numerical model is first verified by comparing the results generated numerically with those of a case study published in the literature prior to beginning the parametric study. This part plays a significant role in building a foundation for the subsequent analyses. The selected case study for the slope stability analysis with and without water was published by Sazzad et al (2016). The main reason for choosing this reference is that it provides simulation results obtained with SSR-FEM, which is the method used in this thesis. Five different models are investigated, and the corresponding simulation results obtained by RS2 are presented for comparison.

3.3.1 Model Description

A homogeneous and isotropic slope without and with water is shown in Figures 3.7 and 3.8, respectively. All the dimensions of the model slope can also be found on the figures. Table 3.5 lists the material properties of the slope.

Table 3.5 Material properties of the slope

Soil parameters	unit	value
Cohesion	(kN/m^2)	10.0
Friction angle	degrees	20.0
Unit weight	(kN/m^3)	18.0
Modulus of elasticity	(MN/m^2)	8.0
Poisson's ratio	\	0.3

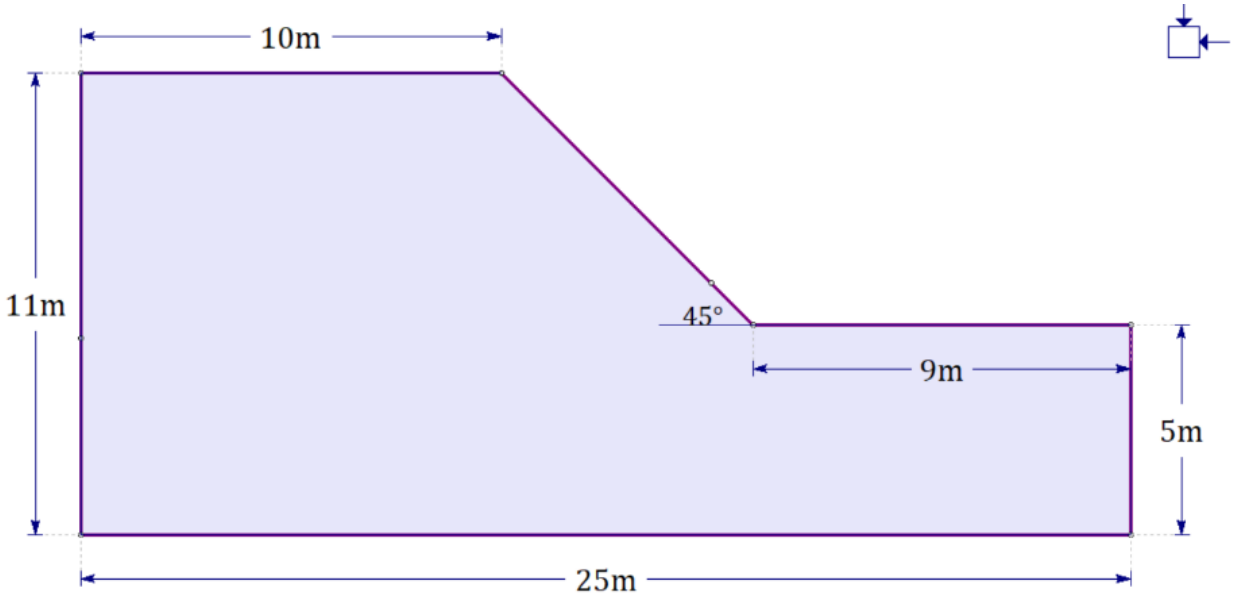

Figure 3.7 Geometry of the model slope without water considered

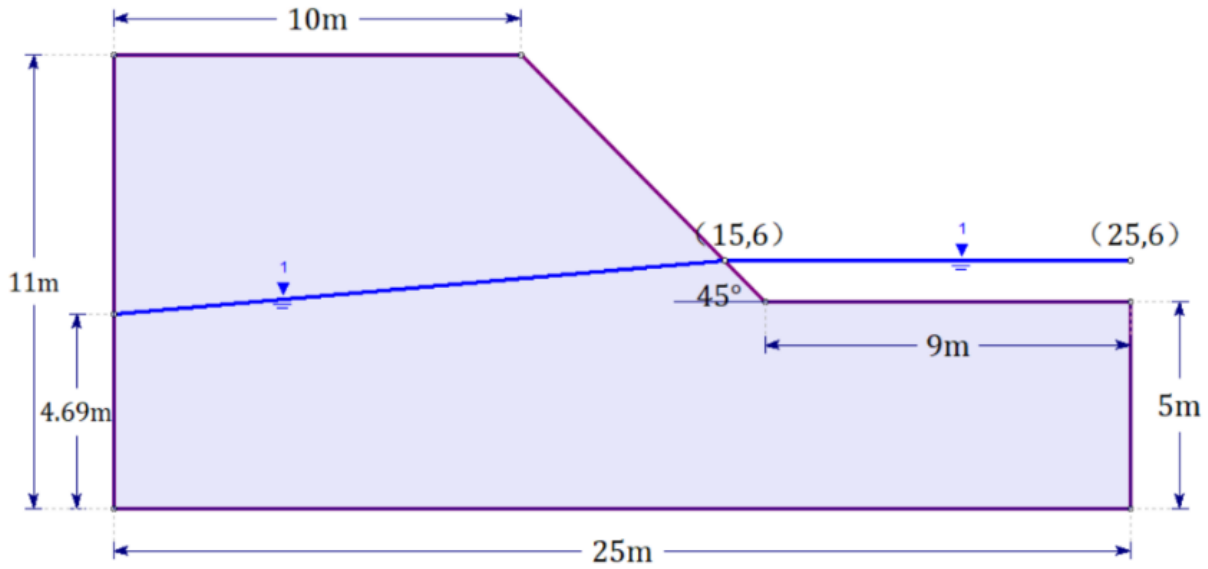

Figure 3.8 Geometry of the model slope with water considered (water level=1.0m)

3.3.2 Result and Discussions

Five conditions are investigated in this section, including a dry slope and slopes with a water level of 0.5m, 1.0m 1.5m, 2.0m from the bottom of the slope (a phreatic line with a 5-degree downward inclination is considered with the water level in all cases of analysis). The slope geometries in this section are the same.

The results calculated by RS2 using the SSR-FEM method are as follows. Figure 3.9 to Figure 3.13 show the critical SRF and failure mechanism. Figure 3.14 illustrates the comparison of the critical SRE in Sazzad et al. (2016) and RS2.

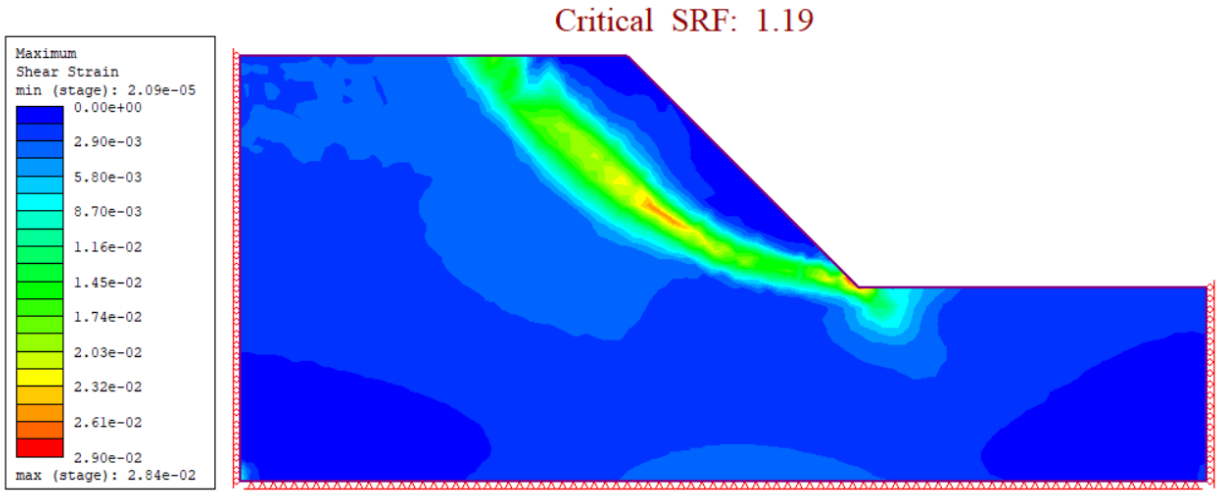

Figure 3.9 Critical SRF and failure mechanism for the dry slope

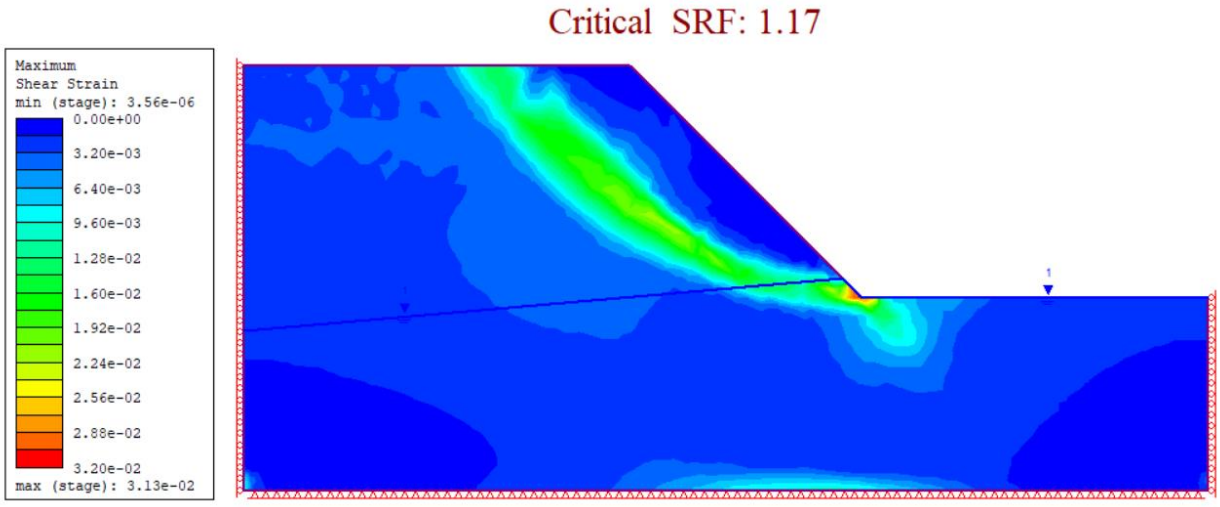

Figure 3.10 Critical SRF and failure mechanism at water level=0.5m from the bottom of the slope

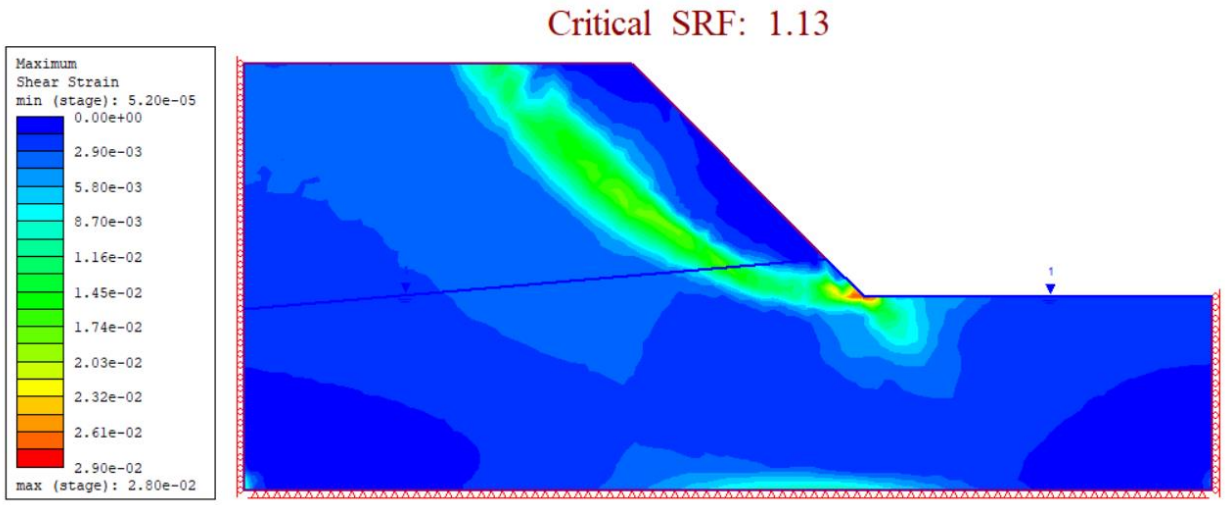

Figure 3.11 Critical SRF and failure mechanism at water level=1.0m from the bottom of the slope

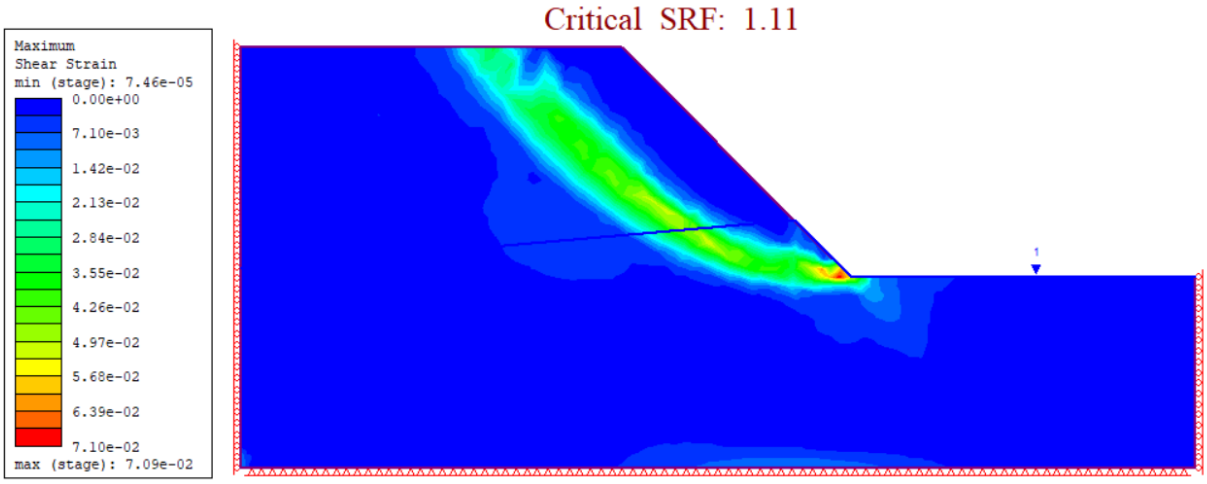

Figure 3.12 Critical SRF and failure mechanism at water level=1.5m from the bottom of the slope

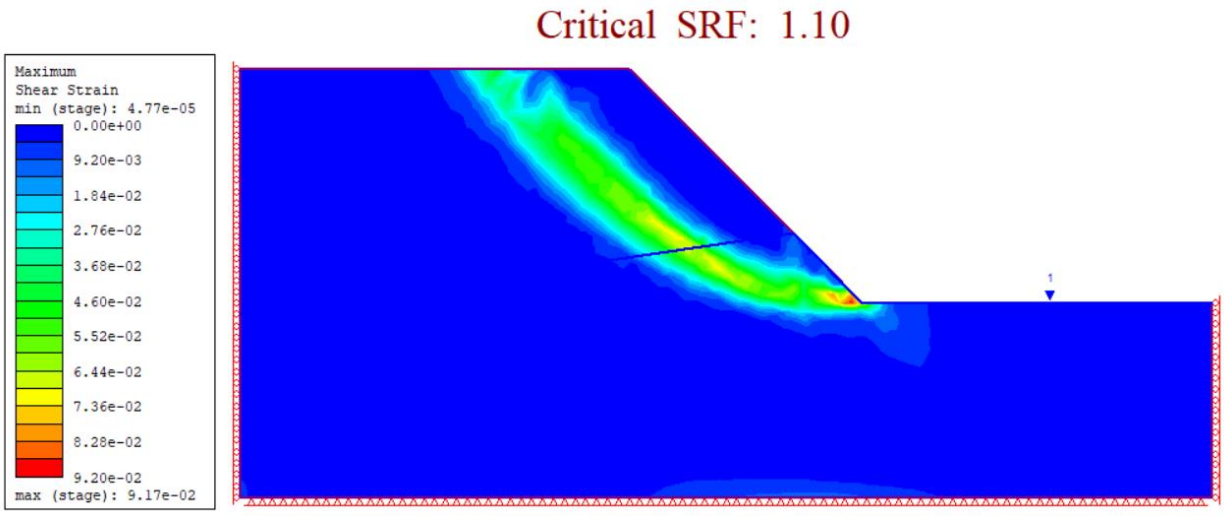

Figure 3.13 Critical SRF and failure mechanism at water level=2.0m from the bottom of the slope

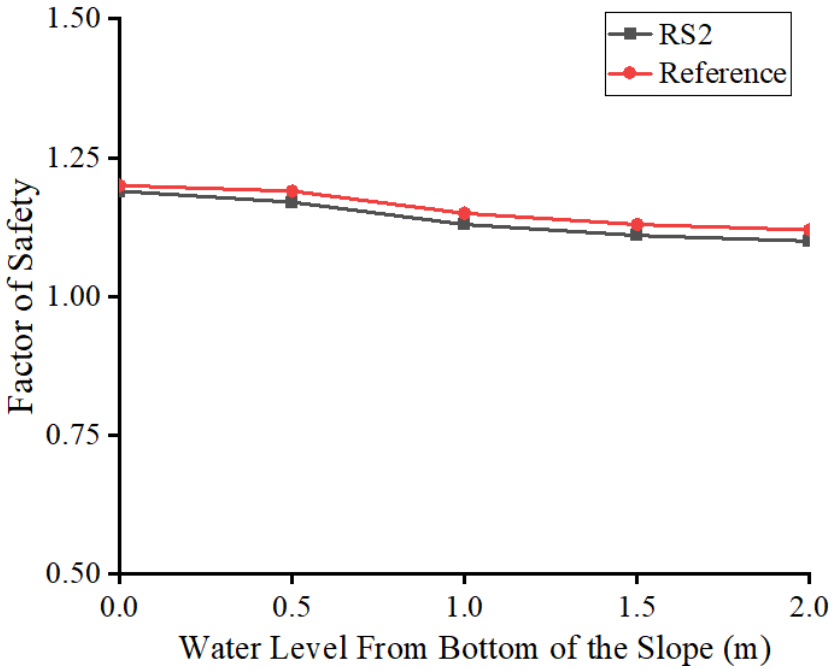

Figure 3.14 Comparison of critical SRF values obtained by RS2 and Sazzad et al. (2016)

Table 3.6 Differences in critical SRF values obtained by RS2 and Sazzad et al. (2016)

	RS2	Reference	
Water level (m)	FS	FS	Differences (as a function of water level)
0	1.19	1.20	0.83%
0.5	1.17	1.19	1.68%
1.0	1.13	1.15	1.74%
1.5	1.11	1.13	1.77%
2.0	1.10	1.12	1.79%
			Error (average)= 1.562%

As shown from Figure 3.12, for each case, the critical SRF values computed by RS2 are very close to those reported by Sazzad et al. (2016). Table 3.6 summarizes the critical SRF values obtained by RS2 and reported by Sazzad et al. (2016) and the differences in the results as a function of water level. The average error of the critical SRF per water level is only 1.562%. Therefore, the simulation results generated by RS2 using SSR-FEM are reliable, demonstrating that RS2 can be used for analyzing the models proposed in this thesis.

Chapter 4 Analysis of Rising Water Level Models and Discussion of Simulation Results

4.1 Introduction

Three sets of analyses are studied in this chapter using the FEM modeling software RS2. These three sets of models represent three different scenarios:

1. a slope with functioning drain pipes (Set I),
2. a slope with a rising water level due to a clogged pipe (Set II), and
3. a slope with both a rising water level and a moving locomotive condition (Set III).

The control variable method has been used to select the model parameters. This chapter consists of four sections. Section 4.2 describes the three sets of models. The parametric studies for Set I and Set II are presented in Section 4.3. Section 4.4 discusses the Set III simulation results, including the relationship between slope geometry, rising water level, and maximum safe locomotive speed. Lastly, Section 4.5 summarizes the salient features of the parametric study.

4.2 Three Sets of Models

4.2.1 Set I: Models with Functioning Drain Pipes

The model of a slope with a functioning pipe represents a slope without train loads. In this Set, three parameters are studied: the slope ratio, the railway embankment height (H_e), and the natural slope height (H_s). Figure 4.1 shows all the combinations for the parameter study of the dry slope model. There is a total of 30 cases in Set I.

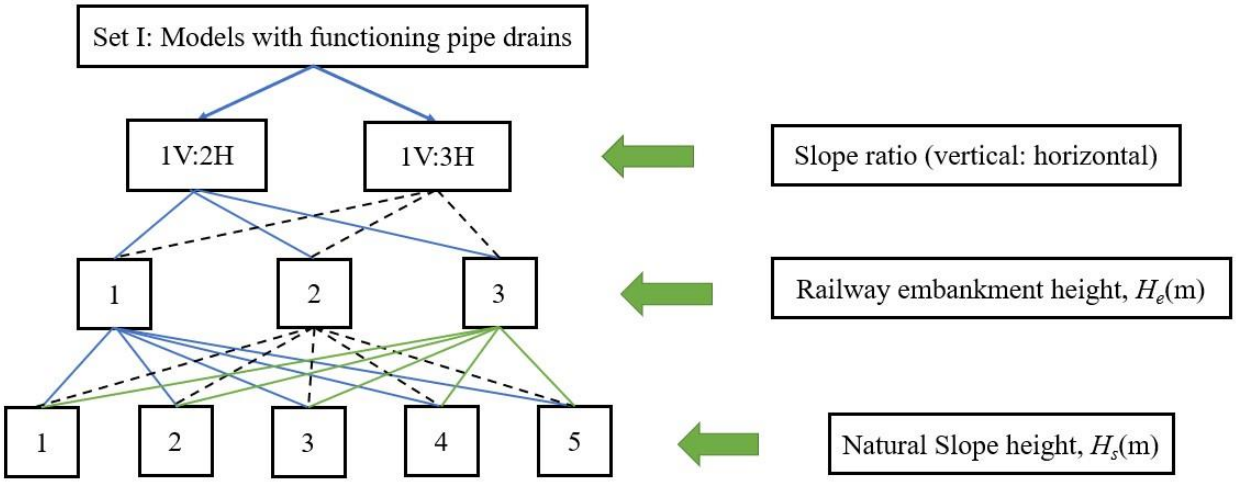

Figure 4.1 Dendrogram of the cases in Set I

To better present the simulation results, Table 4.1 displays all the cases based on the combinations of three parameters, giving a total of two groups and six subgroups with 30 cases.

Table 4.1 All cases in Set I

Groups	Subgroups	Slope ratio	H_e (m)	Number of H_s
Group1	Subgroup1	1V:2H	1	5
	Subgroup2		2	5
	Subgroup3		3	5
Group2	Subgroup4	1V:3H	1	5
	Subgroup5		2	5
	Subgroup6		3	5

Two slope ratios are considered: 1V:2H, and 1V:3H (vertical: horizontal). The railway embankment (H_e) height is set to be 1, 2, and 3m, and the natural slope height (H_s) is set to 1, 2, 3, 4, and 5m. The model dimensions were defined in the previous chapter and remain the same during the analysis. Figure 4.2 (a)-(d) shows models with different parameters. Figure (a) shows the model with a 1V:2H slope ratio, 1m-high railway embankment, and 1m-high natural slope. Figures 4.2 (b)-(d) show models with different parameters. Figure 4.2 (b) illustrates the model with a 1V:2H slope ratio, 3m-high railway embankment, and 1m-high natural slope. Figure 4.2 (c) shows a slope with a ratio of 1V:2H and a railway embankment height and natural slope height of 1m and 5m, respectively. Finally, in Figure 4.2 (d), the model's slope ratio is 1V:3H and the height of both the embankment and the natural slope is set to 1m.

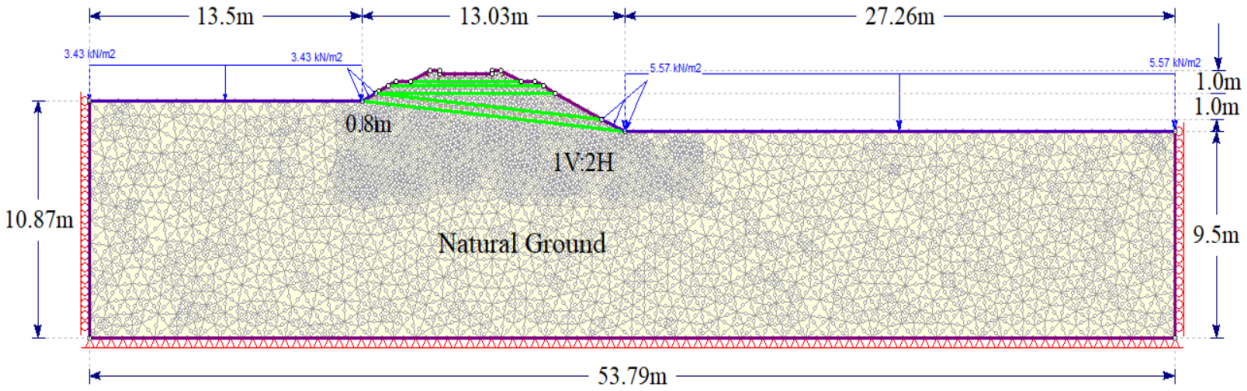

(a) Model geometry: slope ratio=1V:2H, H_e=1m, H_s=1m

Figure 4.2 Several models with different geometry in Set I

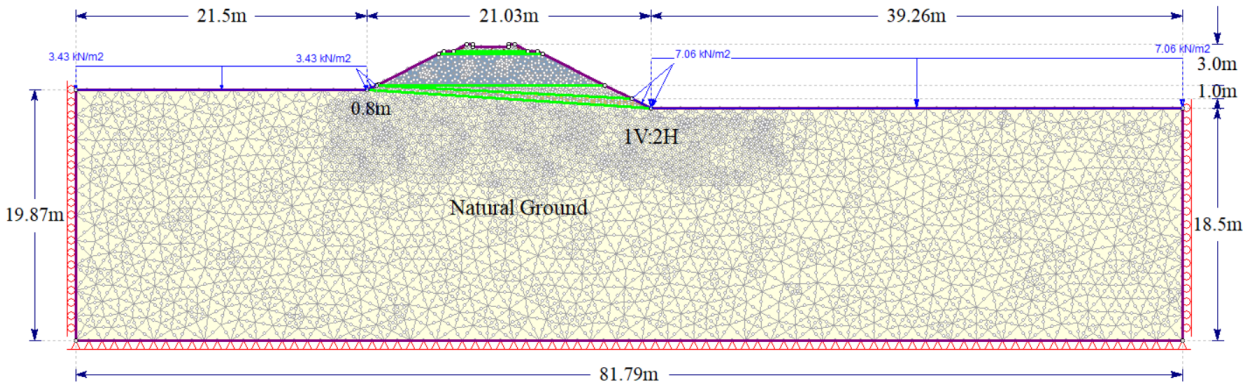

(b) Model geometry: slope ratio=1V:2H, H_e=3m, H_s=1m

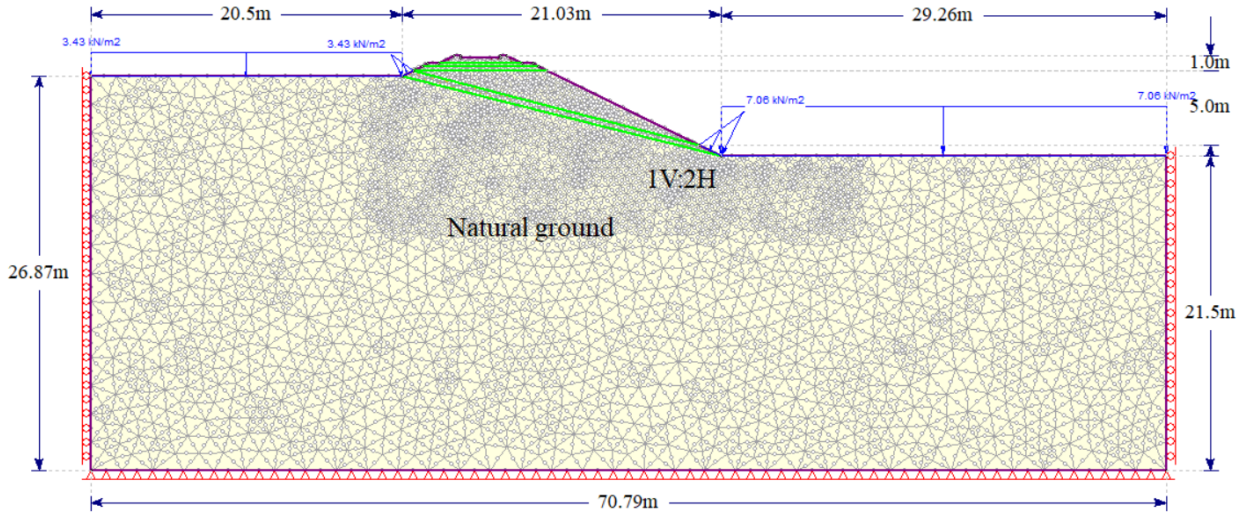

(c) Model geometry: slope ratio=1V:2H, H_e=1m, H_s=5m

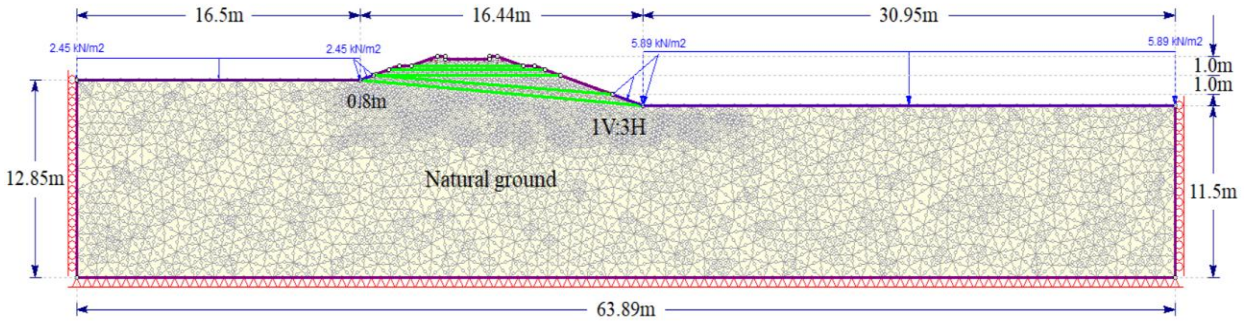

(d) Model geometry: slope ratio=1V:3H, H_e=1m, H_s=1m

Figure 4.2 Several models with different geometry in Set I (continued)

The results of the analyses conducted on the models presented in Figure 4.2 are summarized in Figure 4.3. It is noted that the failure type in Set I is a slope failure with the shape of the failure being a circular slip surface. The maximum shear strain contours and the critical SRF values are

also shown in Figure 4.3. The model in Figure 4.3 (d) (slope ratio=1V:3H, H_e=1m, H_s=1m) has the flattest slope and the highest critical SRF value of 8.98. By contrast, the results of the slope analysis shown in Figure 4.3 (c) (slope ratio=1V:2H, H_e=1m, H_s=5m) yield the lowest critical SRF value, 6.80.

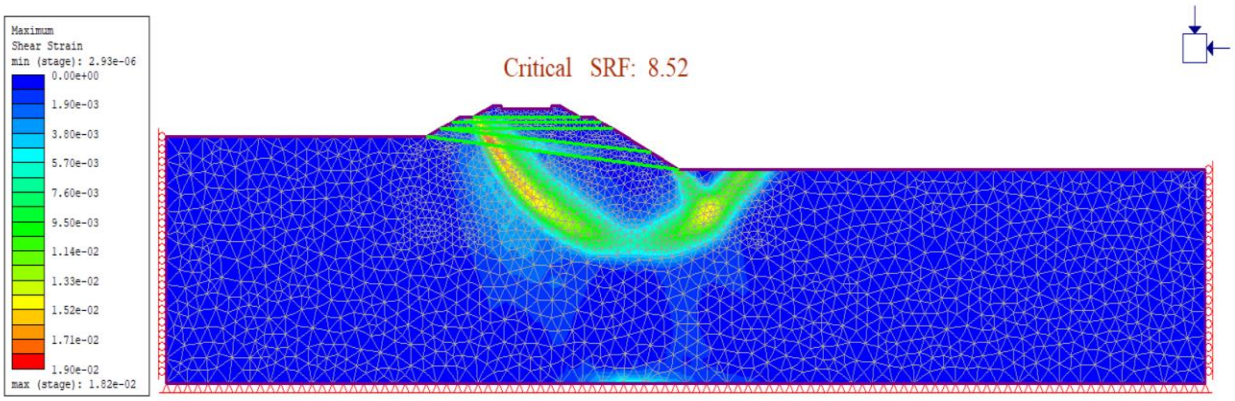

(a) Maximum shear strain contours and critical SRF values for the model: slope ratio= 1V:2H, H_e=1m, H_s=1m

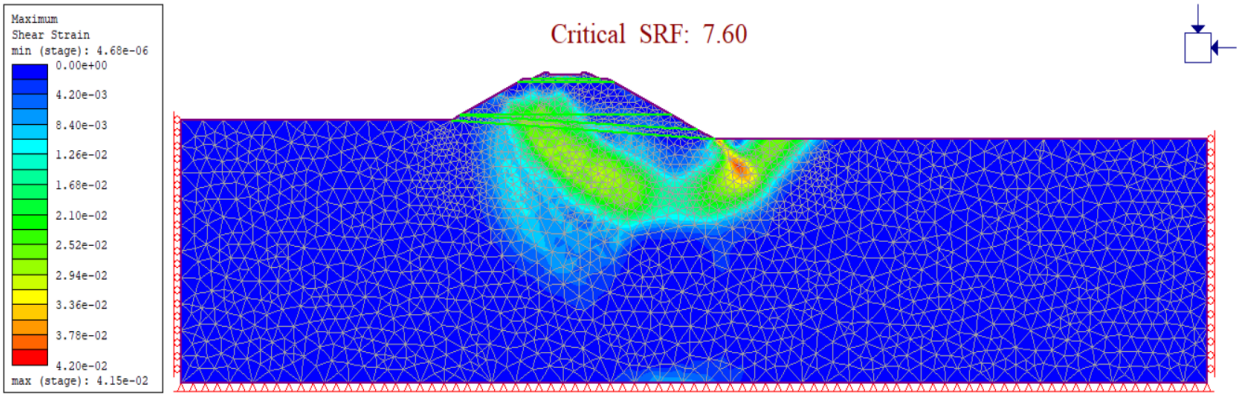

(b) Maximum shear strain contours and critical SRF values for the model: slope ratio= 1V:2H, H_e = 3 m, H_s =1 m

Figure 4.3 Maximum shear strain contours and critical SRF values for several models in Set I

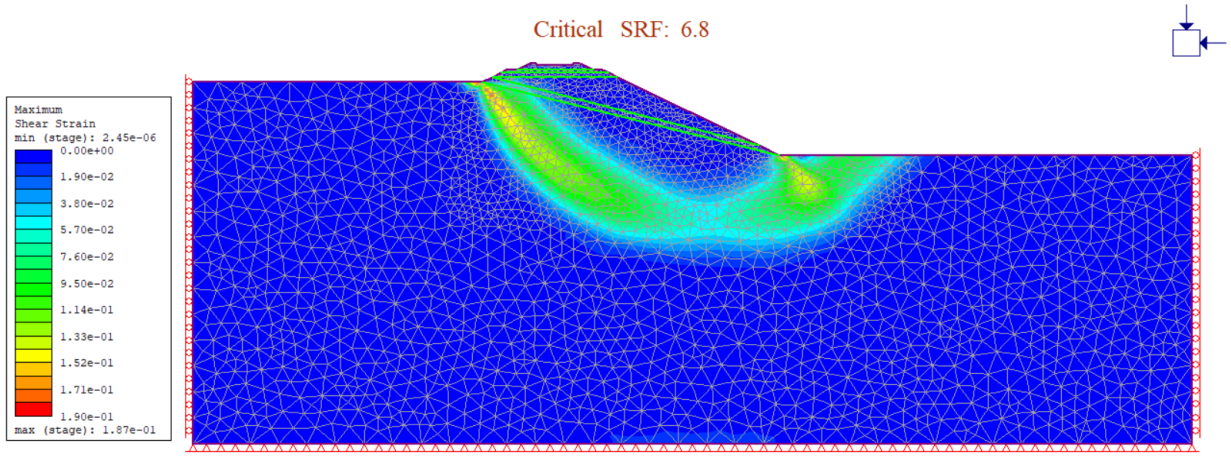

(c) Maximum shear strain contours and critical SRF values for the model: slope ratio= 1V:2H, H_e = 1 m, H_s = 5 m

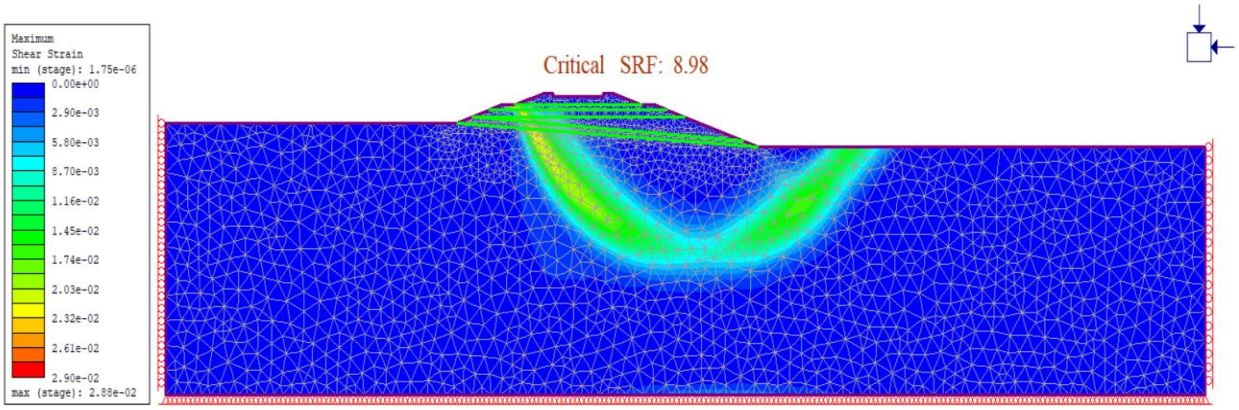

(d) Maximum shear strain contours and critical SRF values for the model: slope ratio= 1V:3H, H_e=1m, H_s=1m

Figure 4.3 Maximum shear strain contours and critical SRF values for Several models in Set I (continued)

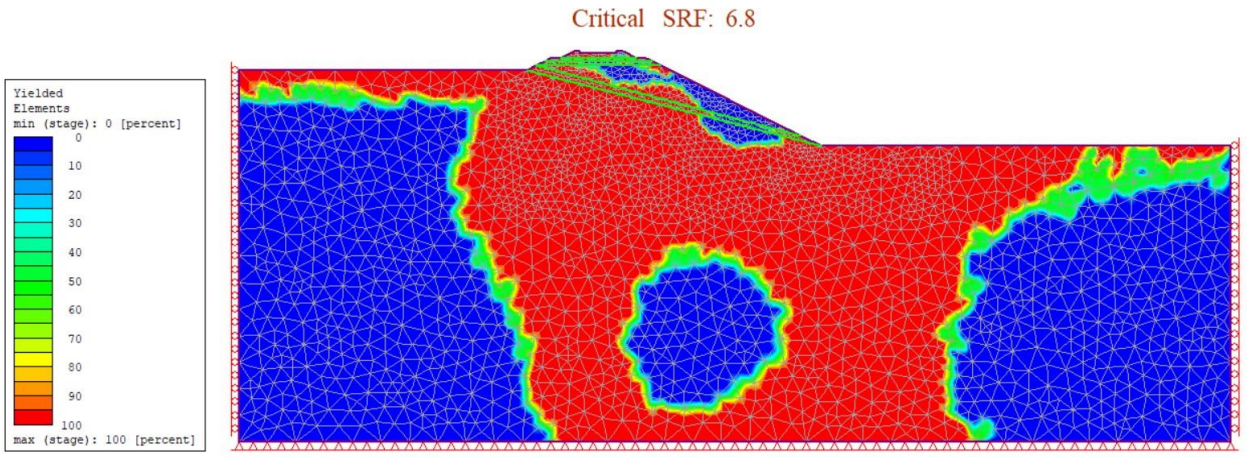

Figure 4.4 Yielded elements contours and critical SRF values for the model: slope ratio= 1V:2H, H_e = 1 m, H_s = 5 m

Figure 4.4 presents the yielded elements for the model (slope ratio= 1V:2H, H_e = 1 m, H_s = 5 m) in Set I. It shows that yielded elements cover the slip surface and extend to the bottom, and most parts of the embankment do not yield.

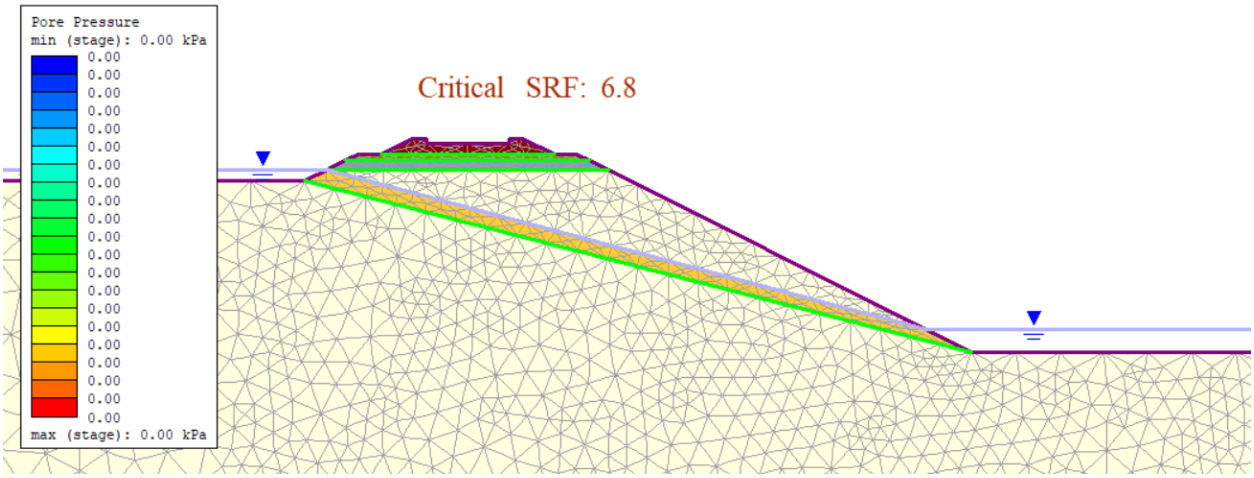

Figure 4.5 Pore pressure contours and critical SRF values for the model: slope ratio = 1V:2H, H_e = 1 m, H_s = 5 m

Figure 4.5 shows pore pressures contours and critical SRF values for the model (slope ratio = 1V:2H, H_e = 1 m, H_s = 5 m). It presents that the pore pressure around the pipe and surroundings are zero when the pipe is functioning well.

The slope is analyzed with the SSR-FEM method. The simulation starts from an initial cohesion and friction angle which are subsequently reduced by FS increments for which the corresponding maximum displacements are calculated. When non-convergence occurred, the critical SRF value was reached. Figure 4.6 (right) presents the relationship between the maximum total displacement and FS for the models in Figure 4.2. The part close to the origin of coordinates has been enlarged to better visualize the SFR, as shown in Figure 4.6 (left).

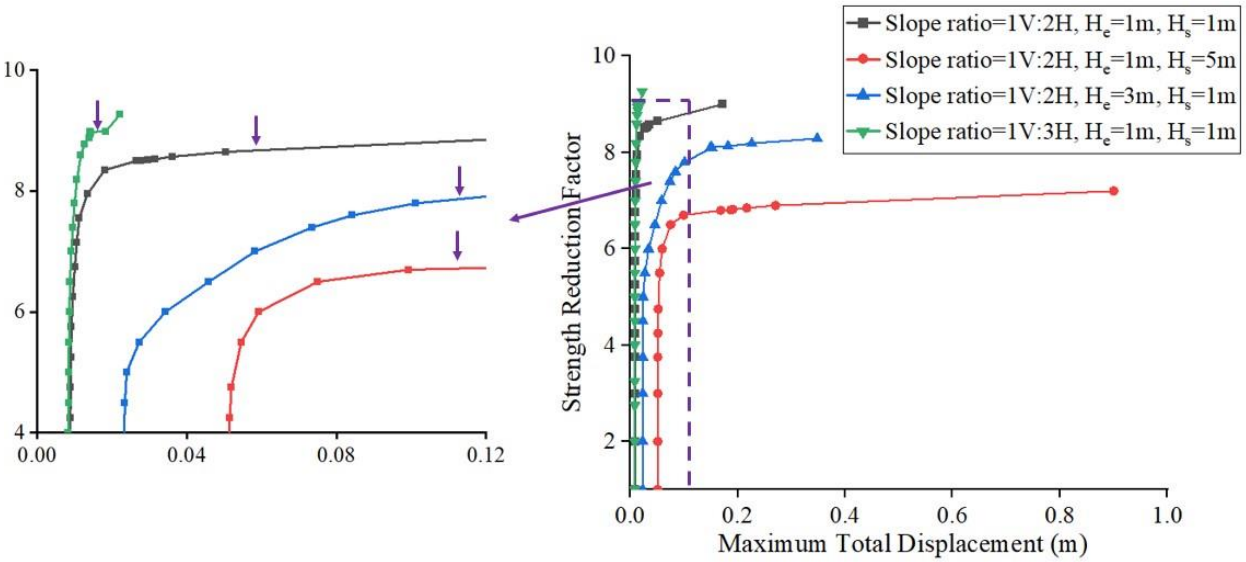

Figure 4.6 Relationship between maximum total displacement (m) and strength reduction factor (FS) for the selected models (right) and the part closer to the origin (left)

Table 4.2 FS value of all the cases in Set I

Groups	Subgroups	FS				
		Natural slope height (m)				
		1	2	3	4	5
Group 1	Subgroup 1	8.52	7.83	7.34	7.02	6.80
	Subgroup 2	7.90	7.45	7.13	6.90	6.72
	Subgroup 3	7.60	7.24	7.01	6.83	6.68
Group 2	Subgroup 4	8.98	8.54	8.04	7.67	7.42
	Subgroup 5	8.55	8.07	7.73	7.48	7.30
	Subgroup 6	8.12	7.78	7.54	7.35	7.21

Table 4.2 demonstrates that the FS generally decreases in higher railway embankments and a greater natural slope height tends to reduce the value of the FS. Meanwhile, FS increases with a flatter embankment. Also, no embankment came close to failure (FS <1.3).

4.2.2 Set II: Models with a Rising Water Level

In Set II, besides the three factors (slope ratio, railway embankment height, and the natural slope height) analyzed in the functioning pipe model (Set I), the rising water level ratio is also included. The rising water ratio is associated with the change in water level or rising depth (L) and the initial total height (H), as shown in Equation (4.1). For example, if H is 1m and L is 0.4m, the corresponding water rising ratio (L/H) is 0.4.

$$rising\ water\ level\ ratio = \frac{L}{H} \tag{4.1}$$

While the drainage time is not considered in undrained conditions, the water rising rate (R) (the increase of water level per unit time) will not be discussed in Set II. The undrained conditions have

the lowest FS values among fully drained and partially drained conditions. So, in Set II, all the models will be simulating in the undrained stage.

In Set II, the rising ratio can take the following values 0.2, 0.4, 0.6, 0.8, and 1.0 and the corresponding rising depth (L) can be calculated by Equation 4.1. Similar to Set I, Figure 4.7 shows all the parameters considered in this set. Table 4.3 summarizes the six groups and 30 subgroups with 150 cases investigated in Set II.

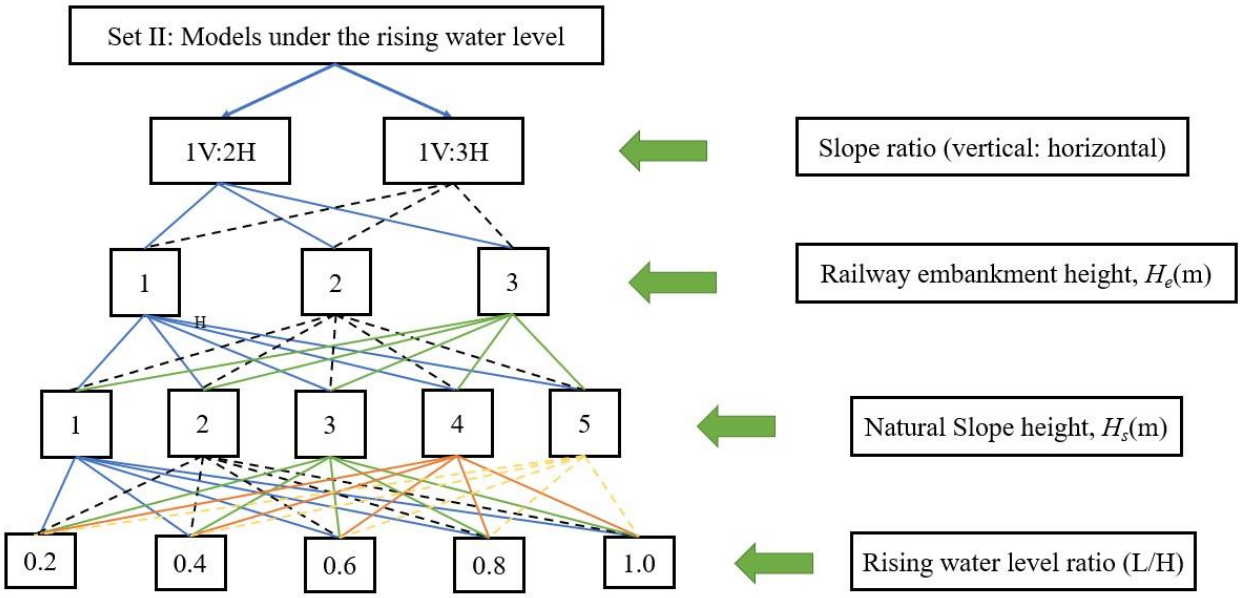

Figure 4.7 Dendrogram of different cases in Set II

Table 4.3 All cases in Set II – models with rising water level conditions

Groups	Subgroups	Slope ratio	H_e (m)	L/H	Number of H_s
Group 3	Subgroup 7	1V:2H	1	0.2	5
	Subgroup 8			0.4	5
	Subgroup 9			0.6	5
	Subgroup 10			0.8	5
	Subgroup 11			1.0	5
Group 4	Subgroup 12		2	0.2	5
	Subgroup 13			0.4	5
	Subgroup 14			0.6	5
	Subgroup 15			0.8	5
	Subgroup 16			1.0	5
Group 5	Subgroup 17		3	0.2	5
	Subgroup 18			0.4	5
	Subgroup 19			0.6	5
	Subgroup 20			0.8	5
	Subgroup 21			1.0	5
Group 6	Subgroup 22	1V:3H	1	0.2	5
	Subgroup 23			0.4	5
	Subgroup 24			0.6	5
	Subgroup 25			0.8	5
	Subgroup 26			1.0	5
Group 7	Subgroup 27		2	0.2	5
	Subgroup 28			0.4	5
	Subgroup 29			0.6	5
	Subgroup 30			0.8	5
	Subgroup 31			1.0	5
Group 8	Subgroup 32		3	0.2	5
	Subgroup 33			0.4	5
	Subgroup 34			0.6	5
	Subgroup 35			0.8	5
	Subgroup 36			1.0	5

When the drain pipe functions well, it is considered to be filled with an idealized high permeability material (the initial k of the pipe is 100 cm/s). In Set II, when ice clogs the pipe, the water level on the left side of the slope rises while it remains unchanged on the right side, i.e., the same level as

the pipe's top, representing a 'no-drainage' condition through the pipe. A material with very low permeability simulates the clogged pipe. In Set II, the k of the clogged pipe is set to $1.0*10^{-13}$ cm/s.

To directly compare the results with Set I (functioning pipe drain model), the model with a 1V:3H slope ratio, 1m-high railway embankment, and 5m-high natural slope is taken as an example. The model's rising water level ratio is varied from 0.2 to 0.4, 0.6, 0.8, and 1.0. The corresponding critical SRFs and the maximum shear strain contours are shown in Figure 4.8 (a)-(e).

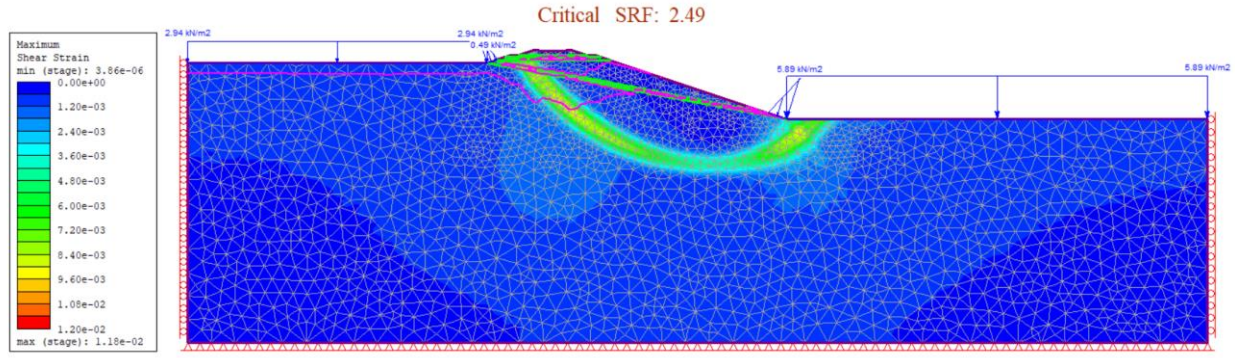

(a) Critical SRF and maximum shear strain contour for the model with slope ratio 1V:3H, H_e=1m, H_s=5m, and L/H=0.2

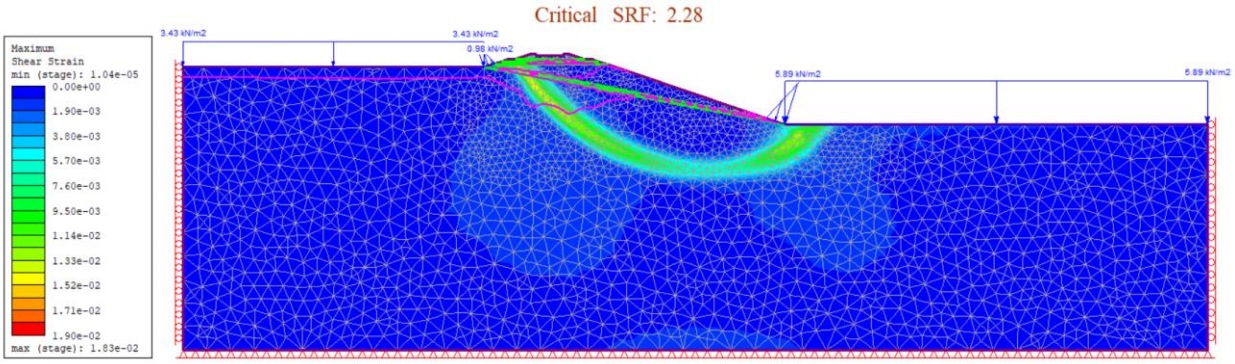

(b) Critical SRF and maximum shear strain contour for the model with slope ratio 1V:3H, H_e=1m, H_s=5m, and L/H=0.4

Figure 4.8 Maximum shear strain contours and critical SRF values for several models in Set II

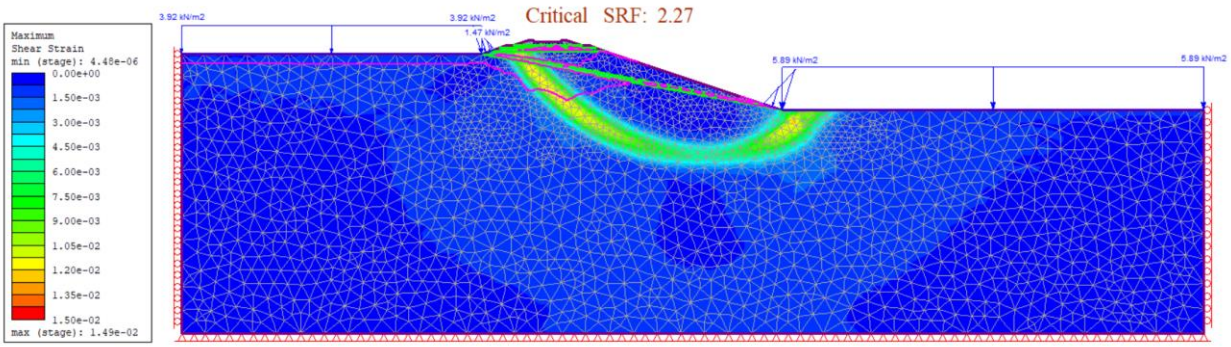

(c) Critical SRF and maximum shear strain contour for the model with slope ratio 1V:3H, H_e=1m, H_s=5m, and L/H=0.6

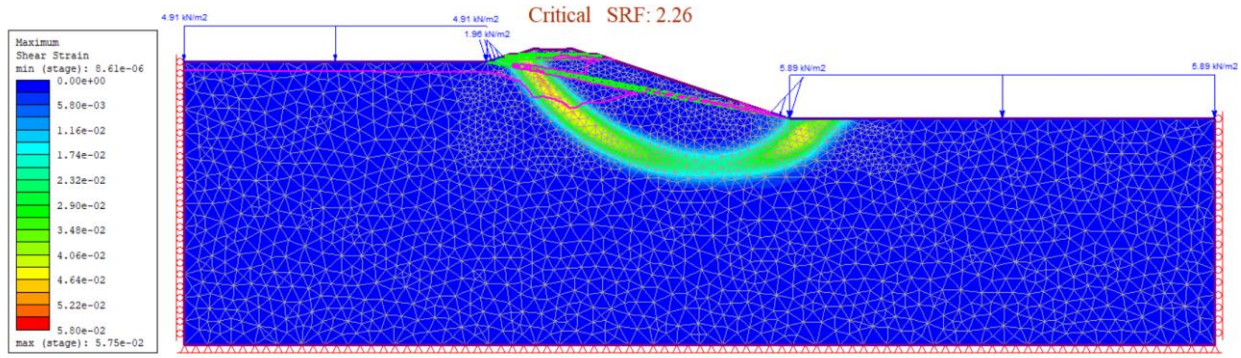

(d) Critical SRF and maximum shear strain contour for the model with slope ratio 1V:3H, H_e=1m, H_s=5m, and L/H=0.8

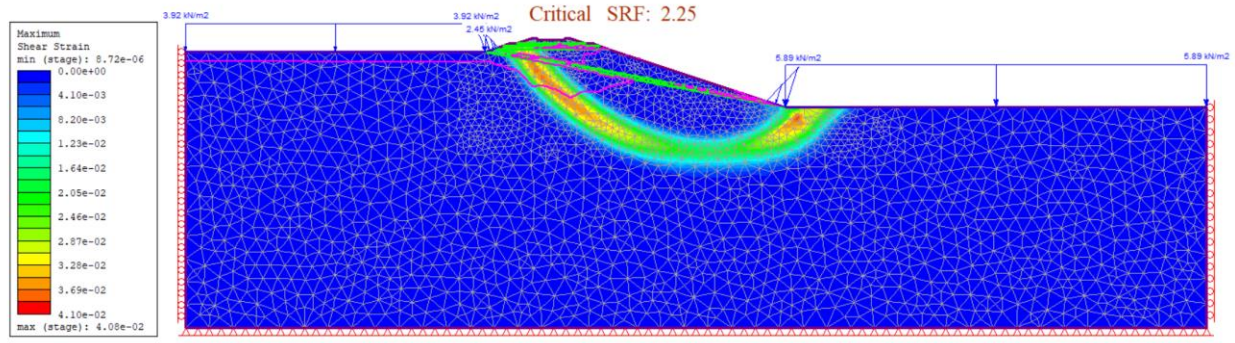

(e) Critical SRF and maximum shear strain contour for the model with slope ratio 1V:3H, H_e=1m, H_s=5m, and L/H=1.0

Figure 4.8 Maximum shear strain contours and critical SRF values for several models in Set II (continued)

The critical SRF decreases with increasing water level ratio. The failure type is still the slope failure with a circular slip surface. FS results for every case in Set II are displayed in Table 4.4. In each Group, a higher water level ratio causes a lower FS. The other trends are similar to the case

of the functioning drain pipe models (Set I), a flatter slope is more stable, and a higher railway embankment has an adverse effect on the slope's FS. In addition, all FS exceed 1.3.

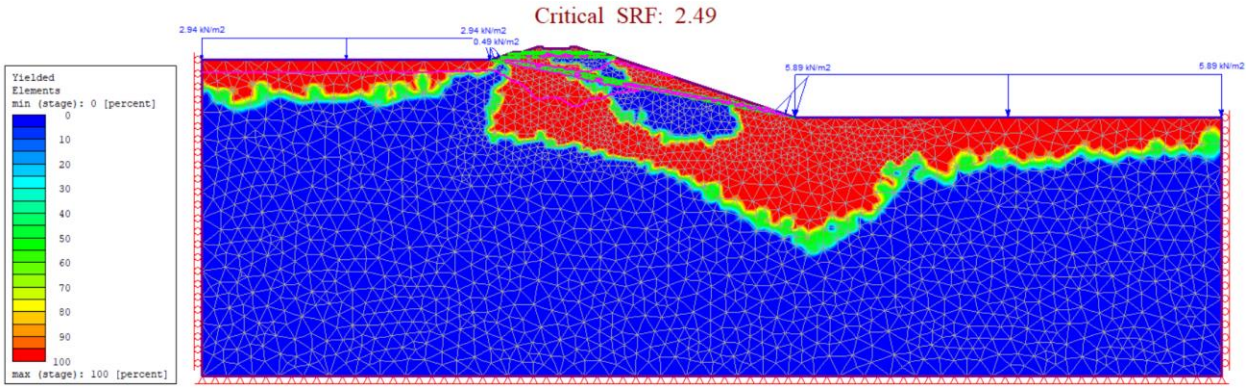

Figure 4.9 Yielded elements contours and critical SRF values for the model with slope ratio 1V:3H, H_e=1m, H_s=5m, and L/H=0.2

The yielding elements of the model (slope ratio 1V:3H, H_e=1m, H_s=5m, and L/H=0.2) in Set II are displayed in Figure 4.9. It shows that yielded elements cover the slip surface, and most parts of the embankment do not yield, similar to models in Set I.

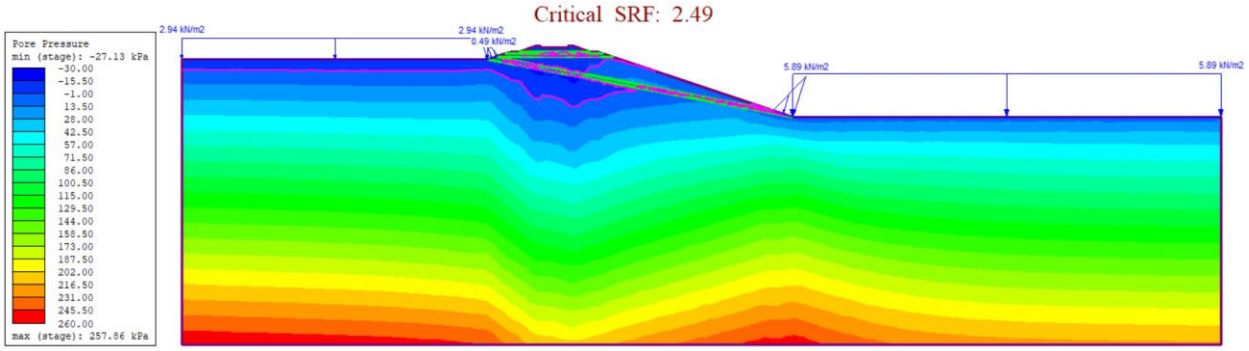

(a) Pore pressure contours and Critical SRF for the model with slope ratio 1V:3H, H_e=1m, H_s=5m, and L/H=0.2

Figure 4.10 Pore pressure contours and Critical SRF for several models in Set II

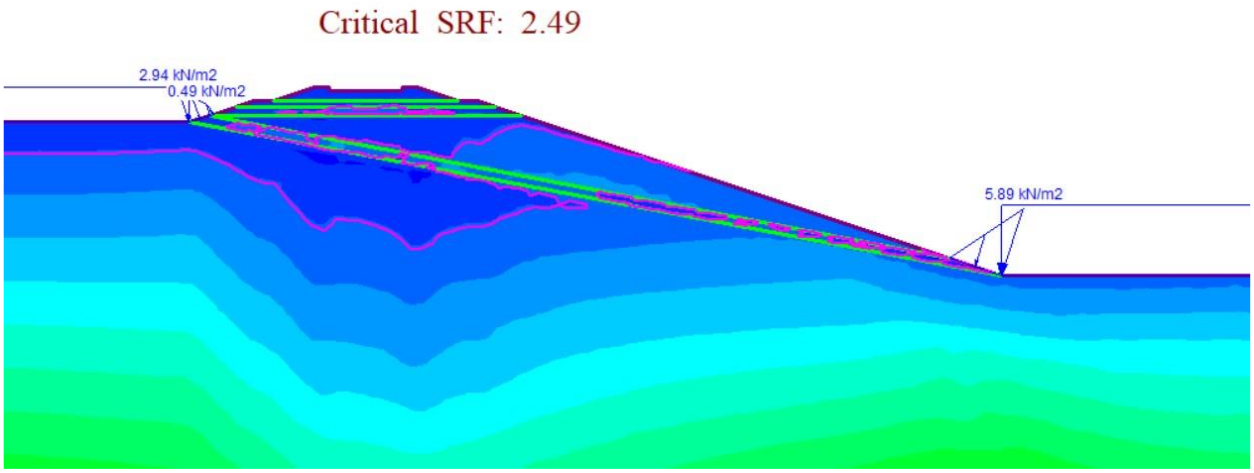

(b) The larger version of railway embankment of Figure 4.10 (a)

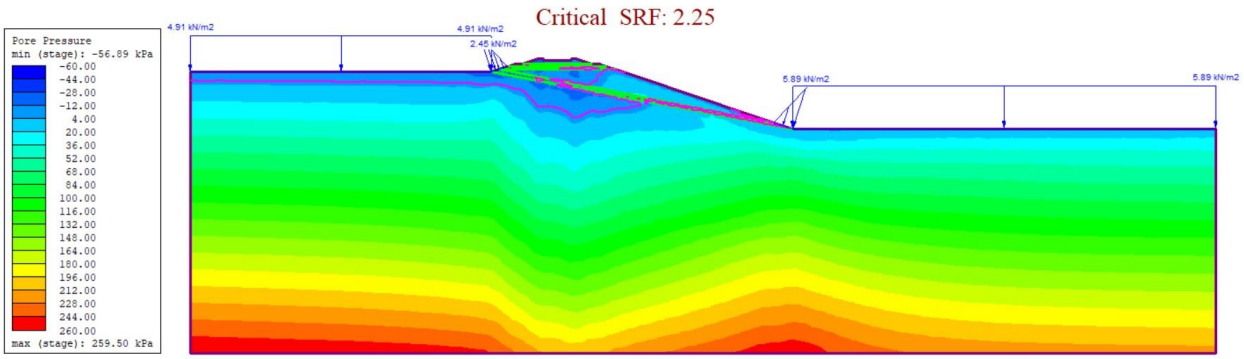

(c) Pore pressure contours and Critical SRF for the model with slope ratio 1V:3H, H_e=1m, H_s=5m, and L/H=1.0

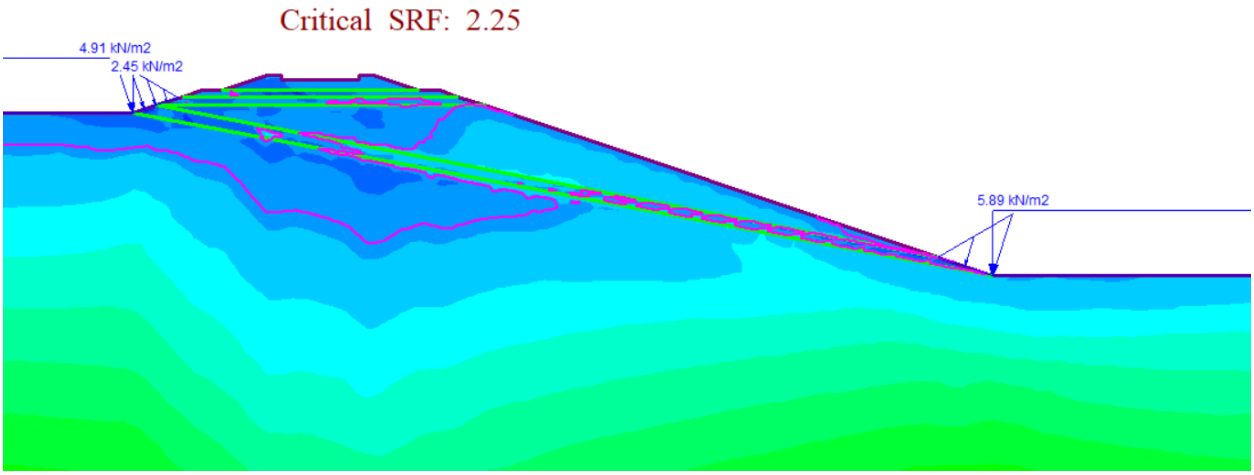

(d) The larger version of railway embankment of Figure 4.10 (c)

Figure 4.10 Pore pressure contours and Critical SRF for several models in Set II (continued)

Figure 4.10 displays pore pressure contours and Critical SRF for the models (slope ratio 1V:3H, H_e=1m, H_s=5m) in different rising water level ratios. When the rising water level ratio grows from 0.2 to 1.0, pore pressure increases considerably in the railway embankment area, especially around the pipe.

Table 4.4 FS of all the cases in Set II

Groups	Subgroups	FS				
		Natural slope height (H_s) (m)				
		1	2	3	4	5
Group 3	Subgroup 7	2.69	2.60	2.59	2.57	2.51
	Subgroup 8	2.46	2.37	2.34	2.32	2.26
	Subgroup 9	2.35	2.25	2.17	2.15	2.14
	Subgroup 10	2.21	2.12	2.11	2.08	2.05
	Subgroup 11	2.13	2.05	2.03	2.01	1.98
Group 4	Subgroup 12	2.39	2.26	2.17	2.09	2.07
	Subgroup 13	2.22	2.17	2.11	2.08	2.04
	Subgroup 14	2.09	2.07	2.04	1.99	1.97
	Subgroup 15	2.04	2.02	1.99	1.89	1.87
	Subgroup 16	1.97	1.96	1.85	1.83	1.82
Group 5	Subgroup 17	2.10	2.09	2.04	2.01	2.00
	Subgroup 18	1.99	1.97	1.96	1.90	1.89
	Subgroup 19	1.95	1.94	1.91	1.90	1.87
	Subgroup 20	1.93	1.86	1.81	1.80	1.79
	Subgroup 21	1.84	1.83	1.80	1.78	1.76
Group 6	Subgroup 22	3.36	3.31	3.24	3.18	3.17
	Subgroup 23	3.03	2.92	2.84	2.83	2.82
	Subgroup 24	2.88	2.85	2.77	2.58	2.56
	Subgroup 25	2.58	2.55	2.52	2.45	2.43
	Subgroup 26	2.49	2.28	2.27	2.26	2.25
Group 7	Subgroup 27	2.66	2.65	2.63	2.57	2.51
	Subgroup 28	2.60	2.58	2.45	2.41	2.39
	Subgroup 29	2.45	2.39	2.29	2.28	2.26
	Subgroup 30	2.37	2.32	2.30	2.25	2.21
	Subgroup 31	2.24	2.20	2.20	2.14	2.1
Group 8	Subgroup 32	2.32	2.26	2.25	2.23	2.22
	Subgroup 33	2.30	2.22	2.19	2.16	2.14
	Subgroup 34	2.25	2.19	2.17	2.15	2.13
	Subgroup 35	2.16	2.11	2.09	2.07	2.05
	Subgroup 36	2.10	2.03	1.93	1.90	1.84

4.2.3 Set III: Model under Rising Water Level and Train Loads Conditions

After simulating all the models in Set I and Set II, the following step is to analyze the models that consider train loads under rising water level conditions.

Figure 4.11 presents the major parameters (slope ratio, railway embankment height, natural slope height, rising water level ratio, and the train speed) considered in Set III. There are a total of 600 cases. The maximum safe train speed ranges from 0 km/h (0 mph) to 120 km/h (75mph). Table 4.5 summarizes all the cases in Set III with six groups (Group 9-14) and 30 subgroups (Subgroup 37-66).

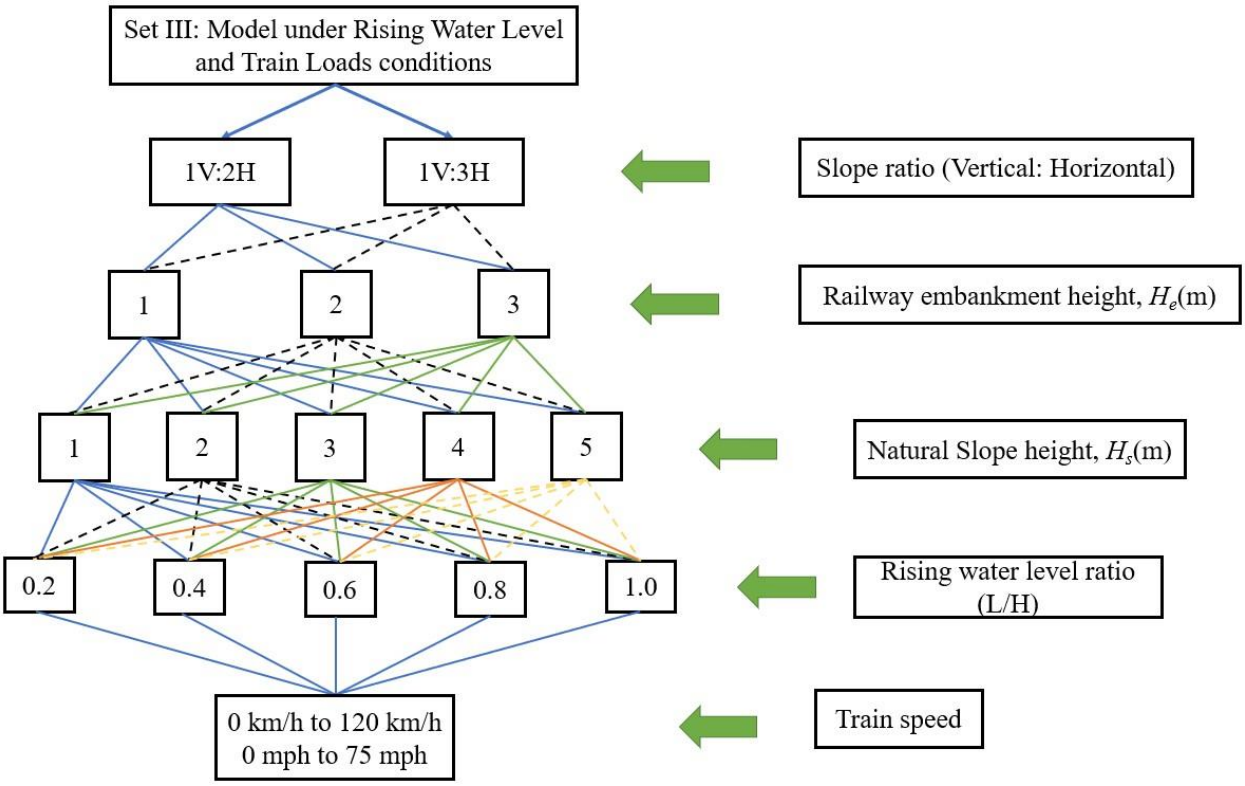

Figure 4.11 Dendrogram of different cases in Set III

Table 4.5 All cases in Set III – model with rising water level conditions and train loads

Groups	Subgroups	Slope ratio	H_e (m)	L/H	Number of H_s	Number of maximum safe train speed
Group 9	Subgroup 37	1V:2H	1	0.2	5	4
	Subgroup 38			0.4	5	4
	Subgroup 39			0.6	5	4
	Subgroup 40			0.8	5	4
	Subgroup 41			1.0	5	4
Group 10	Subgroup 42		2	0.2	5	4
	Subgroup 43			0.4	5	4
	Subgroup 44			0.6	5	4
	Subgroup 15			0.8	5	4
	Subgroup 16			1.0	5	4
Group 11	Subgroup 47		3	0.2	5	4
	Subgroup 48			0.4	5	4
	Subgroup 49			0.6	5	4
	Subgroup 50			0.8	5	4
	Subgroup 51			1.0	5	4
Group 12	Subgroup 52	1V:3H	1	0.2	5	4
	Subgroup 53			0.4	5	4
	Subgroup 54			0.6	5	4
	Subgroup 55			0.8	5	4
	Subgroup 56			1.0	5	4
Group 13	Subgroup 57		2	0.2	5	4
	Subgroup 58			0.4	5	4
	Subgroup 59			0.6	5	4
	Subgroup 60			0.8	5	4
	Subgroup 61			1.0	5	4
Group 14	Subgroup 62		3	0.2	5	4
	Subgroup 33			0.4	5	4
	Subgroup 64			0.6	5	4
	Subgroup 65			0.8	5	4
	Subgroup 66			1.0	5	4

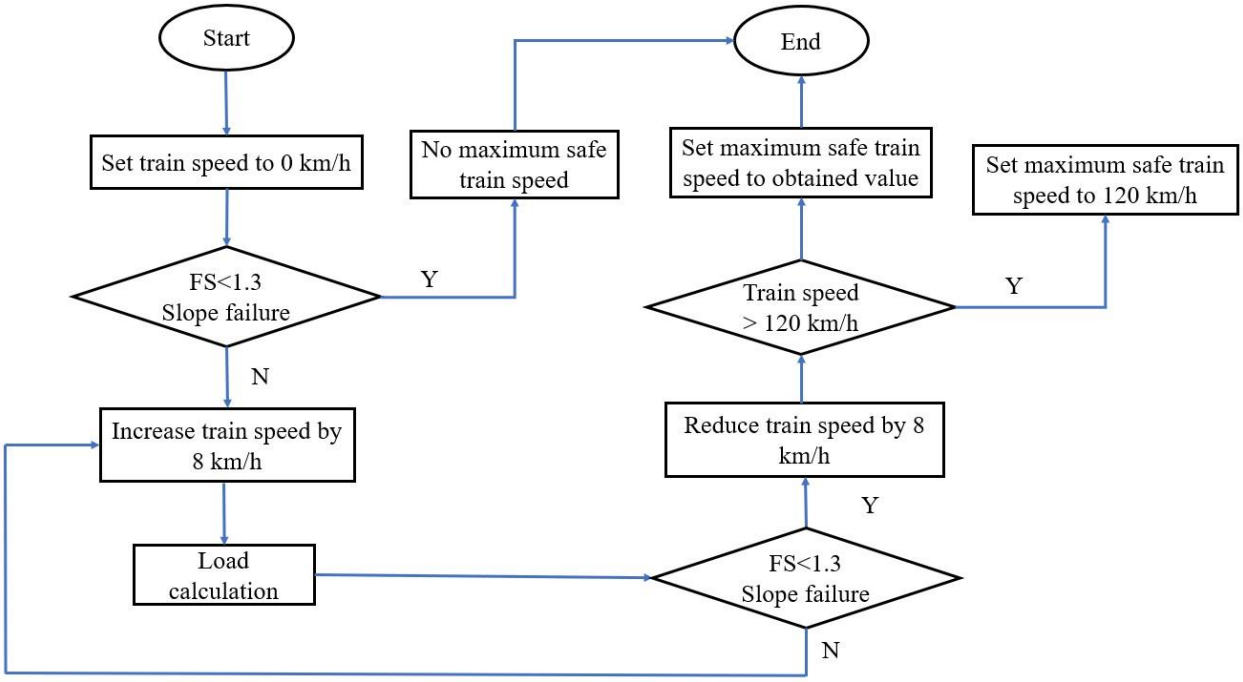

Figure 4.12 The flowchart for obtaining the maximum safe train speed

Figure 4.12 shows the process by which the maximum safe train speed is obtained. All the speeds mentioned in this procedure are calculated manually using the train load in Chapter 3. The analysis begins with an initial train speed of 0 km/h (0 mph) and increases it in increments of 8 km/h (5 mph) to evaluate the slope failure condition (FS < 1.3, refer to the explanation in Section 2.5.5, in Chapter 2). When a slope fails, the speed will be reduced by 5 mph. If the train speed is higher than 120 km/h (75 mph), the maximum safe train speed is set at 120 km/h (75 mph). Otherwise, the obtained value is the maximum safe train speed. Another considered condition is that in which the slope fails when a stationary train is on the track. In this case, there is no maximum safe train speed. The maximum safe train speed with the corresponding applied load can be obtained based on this process.

To better visualize how the FS is affected by rising water levels and train loads, the model with a 1V:3H slope ratio, a 1m-high embankment, and a 5m-high natural slope is selected as an example. This model's rising water level ratio was successively set to 0.2, 0.4, 0.6, 0.8, and 1.0 with a stationary train load. Figure 4.13 (a)-(e) shows the maximum shear strain contour of the selected model with a stationary train.

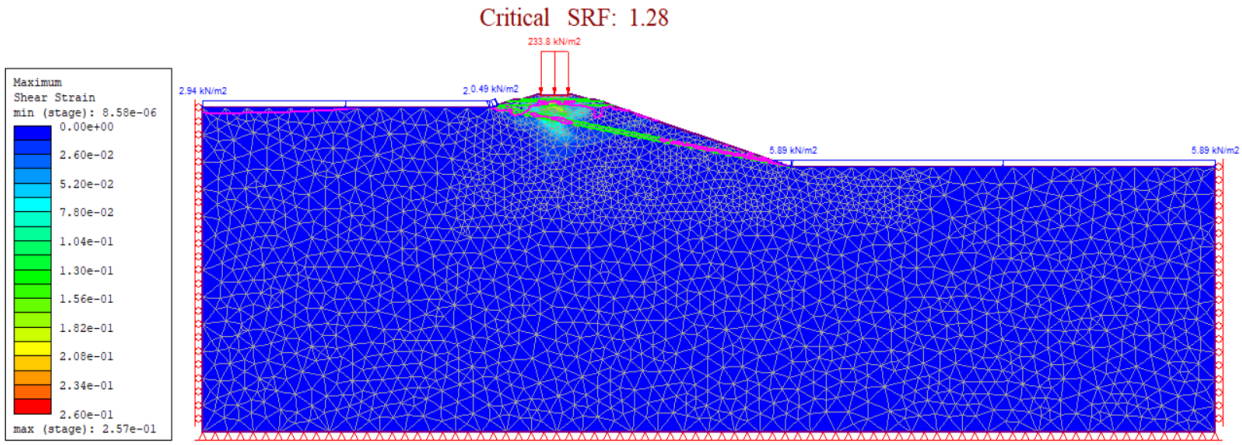

(a) Maximum shear strain contour for the model with 1V:3H slope ratio, H_e=1m, H_s=5m, rising water ratio (L/H) = 0.2, and with a stationary train

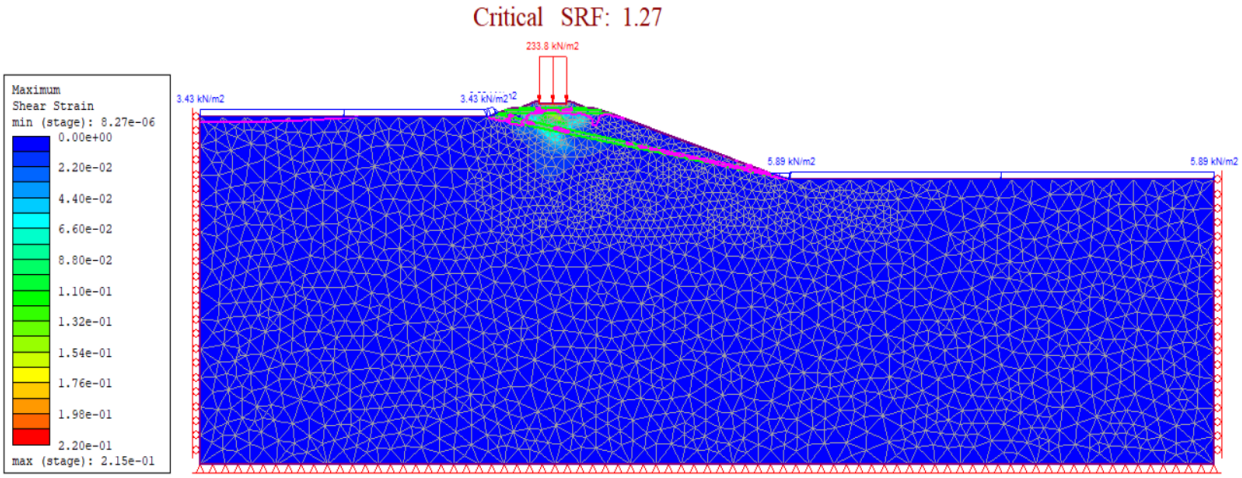

(b) Maximum shear strain contour for the model with 1V:3H slope ratio, H_e=1m, H_s=5m, rising water ratio (L/H) = 0.4, and with a stationary tarin

Figure 4.13 Maximum shear strain contour for several models in Set III

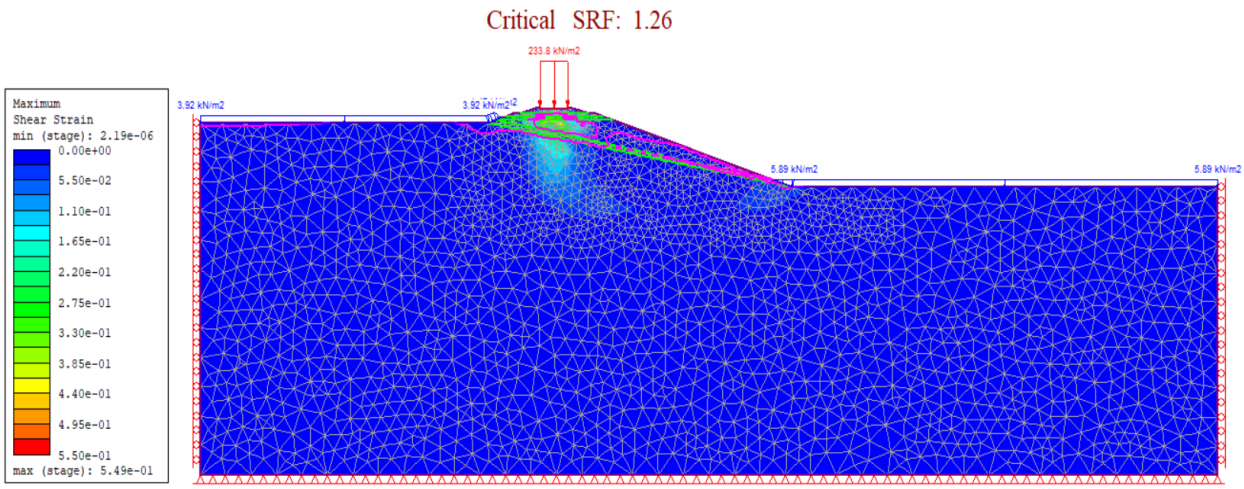

(c) Maximum shear strain contour for the model with 1V:3H slope ratio, H_e=1m, H_s=5m, rising water ratio (L/H) = 0.6, and with a stationary train

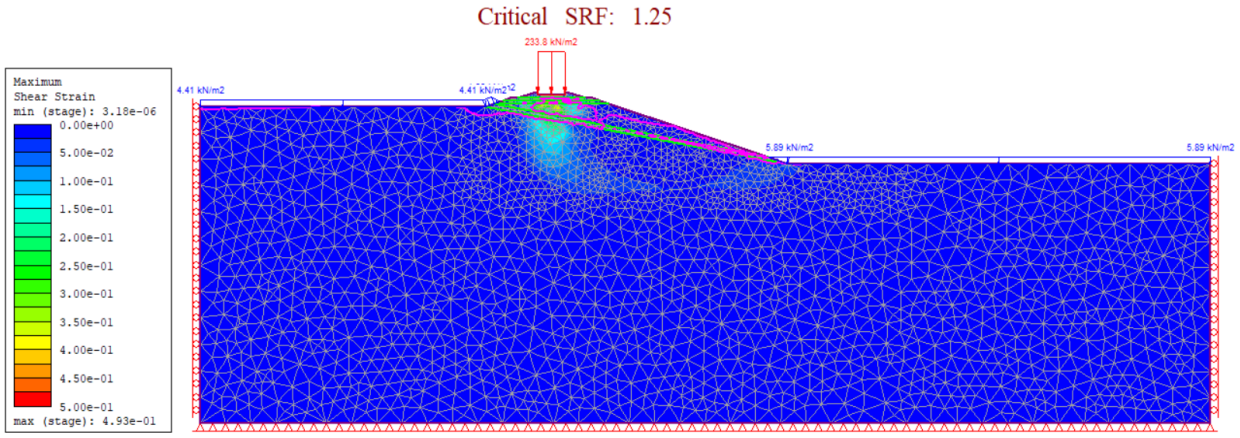

(d) Maximum shear strain contour for the model with 1V:3H slope ratio, H_e=1m, H_s=5m, rising water ratio (L/H) = 0.8, and with a stationary train

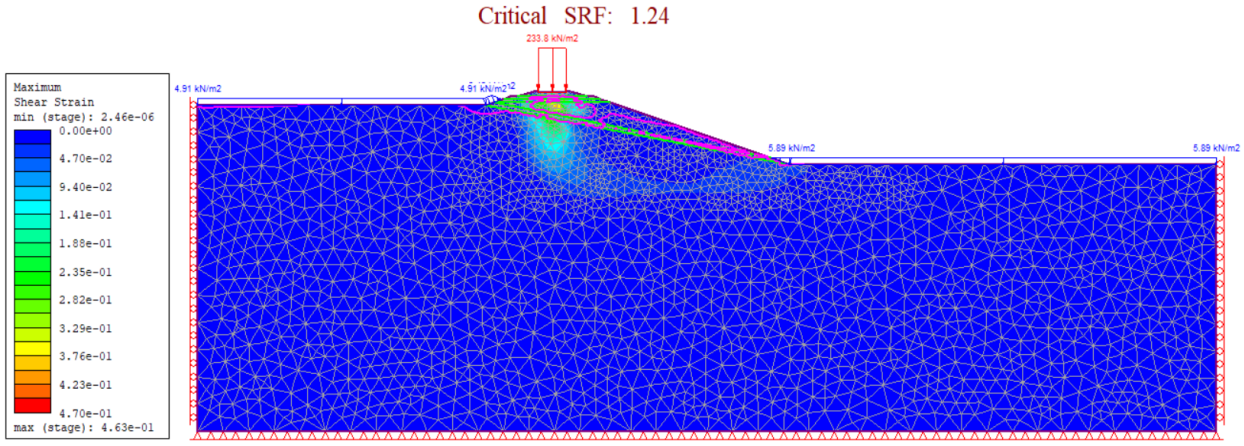

(e) Maximum shear strain contour for the model with 1V:3H slope ratio, H_e=1m, H_s=5m, rising water ratio (L/H) = 1.0, and with a stationary train

Figure 4.13 Maximum shear strain contour for several models in Set III (continued)

All safety factors are lower than 1.3 (the required safety factor for slopes with a rising water level), which means that the train cannot pass through or even park on the area when the rising water level condition occurs or has occurred. In Figure 4.13, when the rising water level ratio are 0.2 and 0.4, the main failure mechanism becomes bearing failure and the majority of the slip surface is concentrated in the embankment. When the rising water level ratio increases, ranging from 0.6 to 1.0, even though the maximum shear strain is in a wedge under the tracks, indicative of bearing type failure, a lobe extending from its bottom towards the free slope is shown in the simulation results, indicating a potential slope failure.

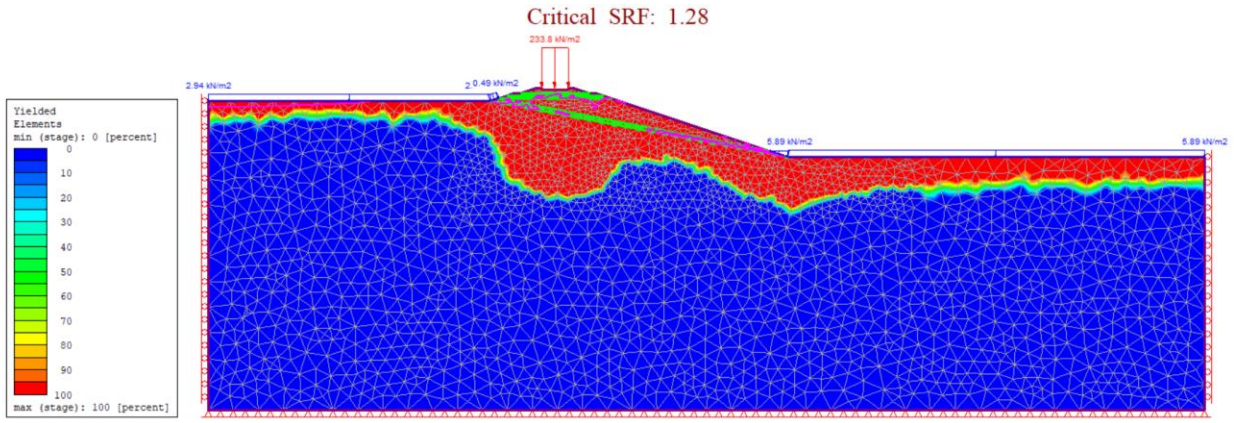

Figure 4.14 Yielded elements contours and critical SRF values for the model with slope ratio 1V:3H, H_e=1m, H_s=5m, and L/H=0.2. and with a stationary train

The yielding elements of the model with slope ratio 1V:3H, H_e=1m, H_s=5m, and L/H=0 and with a stationary train are displayed in Figure 4.14. It shows that yielded element contour covers the whole railway embankment. The yielding area is different from the models in Set I and Set II.

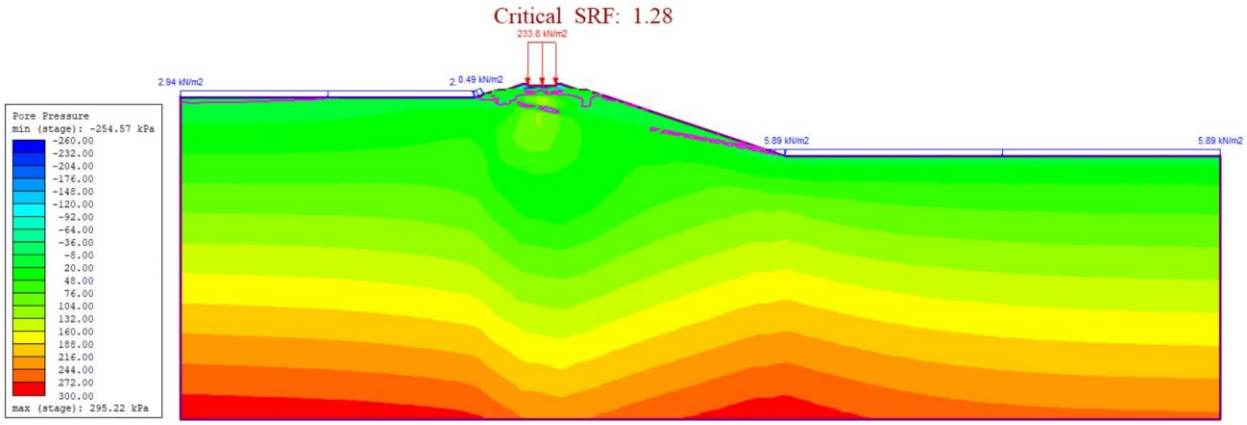

Figure 4.15 Pore pressure contours and Critical SRF for the model with slope ratio 1V:3H, H_e=1m, H_s=5m, and L/H=0.2. and with a stationary train

Figure 4.15 shows pore pressure contours and Critical SRF for the model with slope ratio 1V:3H, H_e=1m, H_s=5m, and L/H=0.2. and with a stationary train. Pore pressure in the railway embankment

significantly increases when the loading is applied on the slope compared with that in Set II (Figure 4.10).

Table 4.6 lists the FS for all the cases in Set III with a stationary train. It can be seen that some models failed (the factors of safety are lower than 1.3), which means those unstable slopes cannot have a maximum safe train speed. The train should avoid parking or passing on the track. Table 4.7 lists the maximum safe train speed for each model in mph (mile/hour) and km/h and the corresponding FS value for every case in Set III (Table 4.5). When the maximum train speed is equal to or greater than 0 km/h (mph), the slope is considered safe whether the train is stationary (maximum safe train speed = 0 km/h) or moving (maximum safe train speed > 0 km/h).

Table 4.6 The FS value of cases with stationary train load (v=0 km/h) in Set III

Groups	Subgroups	FS				
		Natural slope height (H_s) (m)				
		1	2	3	4	5
Group 9	Subgroup 37	1.22	1.21	1.2	1.17	1.17
	Subgroup 38	1.21	1.20	1.19	1.16	1.15
	Subgroup 39	1.20	1.19	1.19	1.16	1.15
	Subgroup 40	1.20	1.18	1.18	1.16	1.14
	Subgroup 41	1.19	1.18	1.17	1.14	1.13
Group 10	Subgroup 42	1.29	1.28	1.28	1.27	1.26
	Subgroup 43	1.28	1.27	1.26	1.25	1.25
	Subgroup 44	1.27	1.27	1.25	1.24	1.23
	Subgroup 15	1.26	1.25	1.24	1.24	1.22
	Subgroup 16	1.26	1.25	1.24	1.23	1.22
Group 11	Subgroup 47	1.41	1.4	1.39	1.39	1.38
	Subgroup 48	1.40	1.38	1.38	1.35	1.35
	Subgroup 49	1.39	1.38	1.36	1.34	1.33
	Subgroup 50	1.37	1.36	1.34	1.33	1.32
	Subgroup 51	1.36	1.34	1.33	1.33	1.32
Group 12	Subgroup 52	1.33	1.32	1.31	1.29	1.28
	Subgroup 53	1.32	1.32	1.30	1.29	1.27
	Subgroup 54	1.32	1.31	1.29	1.28	1.26
	Subgroup 55	1.31	1.30	1.29	1.27	1.25
	Subgroup 56	1.30	1.29	1.28	1.25	1.24
Group 13	Subgroup 57	1.41	1.40	1.38	1.37	1.36
	Subgroup 58	1.40	1.39	1.37	1.37	1.35
	Subgroup 59	1.38	1.37	1.36	1.35	1.34
	Subgroup 60	1.37	1.36	1.34	1.34	1.32
	Subgroup 61	1.37	1.35	1.34	1.33	1.32
Group 14	Subgroup 62	1.53	1.52	1.51	1.49	1.49
	Subgroup 33	1.52	1.51	1.50	1.48	1.47
	Subgroup 64	1.51	1.49	1.48	1.47	1.45
	Subgroup 65	1.49	1.49	1.47	1.47	1.44
	Subgroup 66	1.48	1.47	1.46	1.45	1.43

Table 4.7 The maximum safe train speed and the corresponding FS values of cases in Set III

Groups	Subgroups	Maximum safe train speed										FS values for models with the maximum train speeds					
		mph (miles/h)					km/h										
		Natural slope height (H_s) (m)					Natural slope height (H_s) (m)										
		1	2	3	4	5	1	2	3	4	5	1	2	3	4	5	
Group 9	Subgroup 37	\	\	\	\	\	\	\	\	\	\	\	\	\	\	\	
	Subgroup 38	\	\	\	\	\	\	\	\	\	\	\	\	\	\	\	
	Subgroup 39	\	\	\	\	\	\	\	\	\	\	\	\	\	\	\	
	Subgroup 40	\	\	\	\	\	\	\	\	\	\	\	\	\	\	\	
	Subgroup 41	\	\	\	\	\	\	\	\	\	\	\	\	\	\	\	
Group 10	Subgroup 42	\	\	\	\	\	\	\	\	\	\	\	\	\	\	\	
	Subgroup 43	\	\	\	\	\	\	\	\	\	\	\	\	\	\	\	
	Subgroup 44	\	\	\	\	\	\	\	\	\	\	\	\	\	\	\	
	Subgroup 45	\	\	\	\	\	\	\	\	\	\	\	\	\	\	\	
	Subgroup 46	\	\	\	\	\	\	\	\	\	\	\	\	\	\	\	
Group 11	Subgroup 47	25	25	20	20	20	40	40	32	32	32	1.31	1.30	1.31	1.31	1.30	
	Subgroup 48	25	20	20	10	10	40	32	32	16	16	1.30	1.30	1.30	1.31	1.31	
	Subgroup 49	20	20	15	10	5	32	32	24	16	8	1.31	1.30	1.30	1.30	1.31	
	Subgroup 50	15	15	10	15	5	24	24	16	8	8	1.31	1.30	1.30	1.31	1.30	
	Subgroup 51	15	10	5	5	5	24	16	8	8	8	1.30	1.30	1.31	1.31	1.30	
Group 12	Subgroup 52	5	5	0	\	\	8	8	0	\	\	1.31	1.30	1.31	\	\	
	Subgroup 53	5	5	0	\	\	8	8	0	\	\	1.30	1.30	1.30	\	\	
	Subgroup 54	5	0	\	\	\	8	0	\	\	\	1.30	1.31	\	\	\	
	Subgroup 55	0	0	\	\	\	0	0	\	\	\	1.31	1.30	\	\	\	
	Subgroup 56	0	\	\	\	\	0	\	\	\	\	1.30	\	\	\	\	
Group 13	Subgroup 57	25	25	20	15	15	40	40	32	24	24	1.31	1.30	1.30	1.31	1.30	
	Subgroup 58	25	20	15	15	10	40	32	24	24	16	1.30	1.31	1.31	1.31	1.31	
	Subgroup 59	20	15	15	10	10	32	24	24	16	16	1.30	1.31	1.30	1.31	1.30	
	Subgroup 60	15	15	10	10	5	24	24	16	16	8	1.31	1.30	1.30	1.30	1.30	
	Subgroup 61	15	10	10	5	5	24	16	16	8	8	1.31	1.31	1.30	1.31	1.30	
Group 14	Subgroup 62	55	55	50	45	45	88	88	80	72	72	1.31	1.30	1.31	1.31	1.31	
	Subgroup 63	55	50	50	45	40	88	80	80	72	64	1.30	1.31	1.31	1.30	1.31	
	Subgroup 64	50	45	45	40	35	80	72	72	64	56	1.31	1.31	1.30	1.31	1.31	
	Subgroup 65	45	45	40	40	35	72	72	64	64	56	1.31	1.31	1.31	1.31	1.30	
	Subgroup 66	45	40	40	35	30	72	64	64	56	48	1.30	1.31	1.30	1.31	1.31	

4.3 Discussion of the Results from Set I and Set II

4.3.1 Comparison of Analysis Results for Set I

In Set I, the slope ratio, railway embankment height, and the height of the natural slope are the investigated geometric parameters as shown in Figure 4.1. Figure 4.16 plots the FS results of Group 1 and Group 2 as a function of the natural slope height while also considering the three railway embankment heights (H_e). Both graphs indicate that a higher natural slope height results in a lower FS value and that the height of the railway embankment adversely impacts slope stability. On the other hand, a flatter slope makes the slope safer.

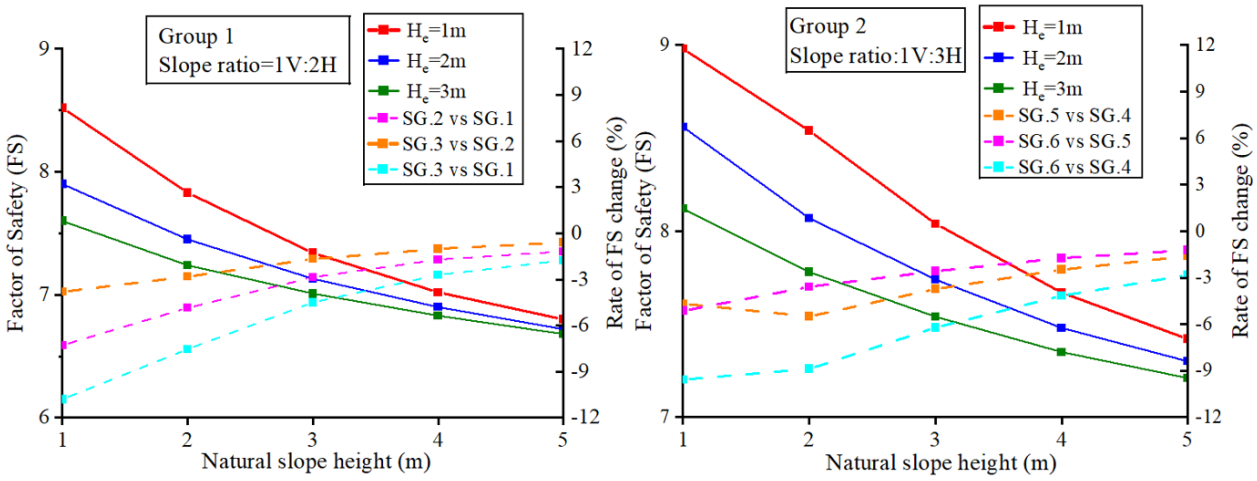

(a) (b)

Figure 4.16 FS results and the change of FS between subgroups versus the natural slope heights (1 -5m) with railway embankment (1,2,3m), slope ratios are (a) 1V:2H and (b) 1V:3H

Figure 4.16 also shows the rate of change of the FS for each Subgroup (SG) in Set I. The rate of change of the FS is calculated by Equation (4.1):

$$R_F = \frac{FS_a n - FS_b n}{FS_b n} \tag{4.1}$$

where R_F is the rate of change of FS, a or b is the Subgroup group number (a, b=1,2,3,4,5,6), and n is the natural slope height (n=1,2,3,4,5).

For example, when the natural slope height is 1m, the FS in Subgroup 2 are compared to those in Subgroup 1, the calculation of the R_F is $\frac{FS_2 1 - FS_1 1}{FS_1 1} = \frac{7.9 - 8.52}{8.52}$ = -7.28%. It means that the FS is reduced by 7.28% for the model with a 1m-high natural slope when the railway embankment height increases from 1m to 2m.

In Figure 4.16, the rate of reduction of FS steadily decreases with an increase in the natural slope height. Meanwhile, the increment increases of the railway embankment height also lowered the reduction rate of FS for each Group.

In Set I, the model in Subgroup 3 with a 5m natural slope has the lowest FS (6.68) which is well beyond the minimal safe criterion of 1.3.

4.3.2 Comparison with the Results for Set II

In Set II, the effects of the railway embankment's height, the natural slope's height, and slope ratio are identical to those in Set I. The slope is safer when it is flatter, with a lower railway embankment, and a natural slope height. In addition to these parameters, the rising water level ratios are set to 0.2, 0.4, 0.6, 0.8, and 1.0.

Figure 4.17 shows the FS values in Group 3-8, and Figure 4.18 illustrates the FS rate of change (%) in Set II subgroups compared with Set I. The trends of the FS in Figure 4.17 are nearly the same with different railway embankment heights when the slope ratio is 1V:2H or 1V:3H. Also, the flatter slopes (slope ratio of 1V:3H) have a higher factor of safety. For each Group, a higher natural slope leads to a lower slope stability, and when the rising water level ratio increases, the FS gradually becomes smaller.

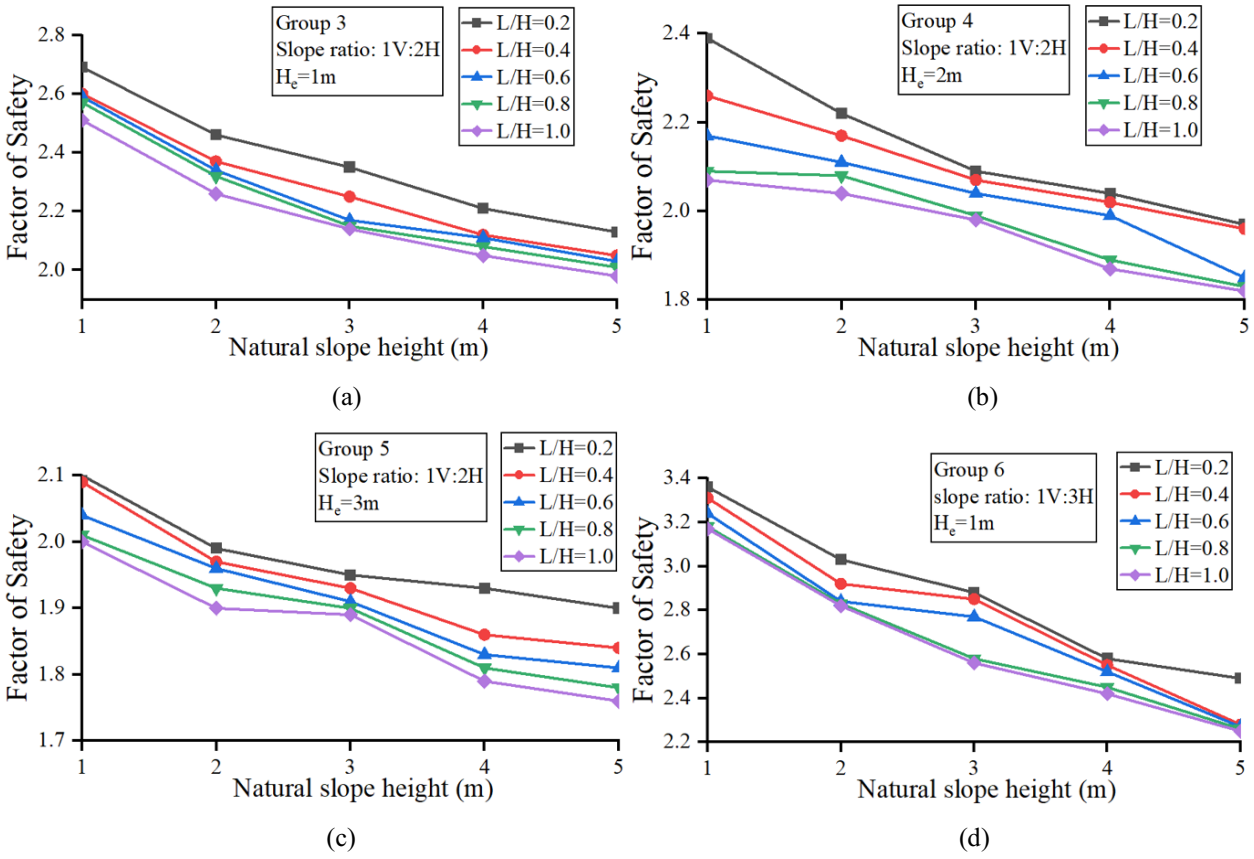

Figure 4.17 FS value versus natural slope height in Group 4-8 in a range of 1 m to 5m with three railway embankment heights (1m, 2m, and 3m), all cases in Set II are divided into (a) Group 3, (b) Group 4, (c) Group 5, (d) Group 6, (e) Group 7, (f) Group 8

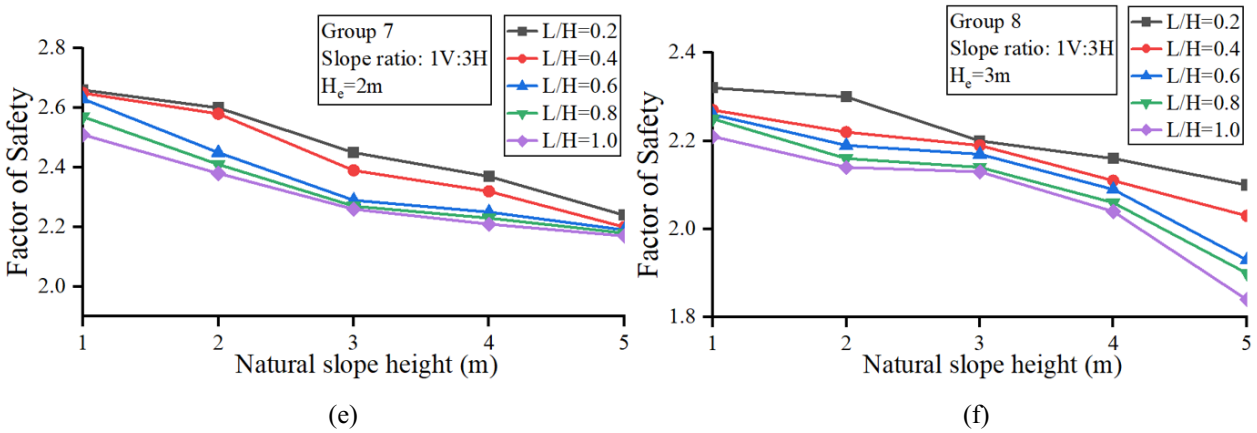

Figure 4.17 FS value versus natural slope height in Group 4-8 in a range of 1 m to 5m with three railway embankment heights (1m, 2m, and 3m), all cases in Set II are divided into (a) Group 3, (b) Group 4, (c) Group 5, (d) Group 6, (e) Group 7, (f) Group 8 (continued)

Figure 4.18 reveals that the FS reduction varied from -62% to -74% compared to the slope with a functioning drain pipe (Subgroup 1-6), indicating that the wet slope dramatically affects the FS. However, with the growth of the rising water level ratio, the FS's rate of change increases by approximately 2% when the rising ratio (L/H) increases by 0.2. When the rising ratio (L/H) is 1.0, the FS's rate of change is more significant than other counterparts in each graph.

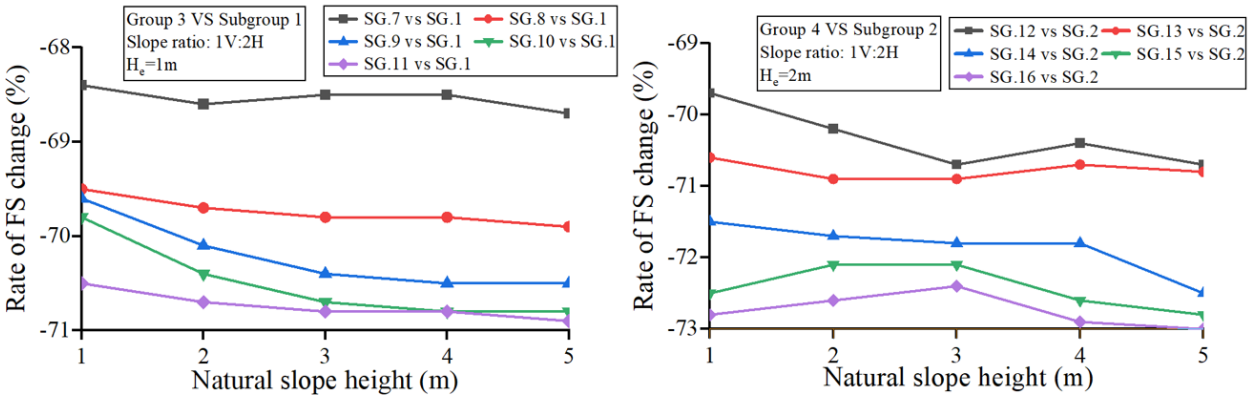

Figure 4.18 Rate of FS change (Set II vs Set I) versus natural slope height in a range of 1 m to 5m with three railway embankment heights (1m, 2m, and 3m), all cases divided into (a) GP. 3 vs SG. 1, (b) GP. 4 vs SG. 2, (c) GP. 5 vs SG. 3, (d) GP. 6 vs SG. 4, (e) GP. 7 vs SG. 5, (f) GP. 8 vs SG. 6

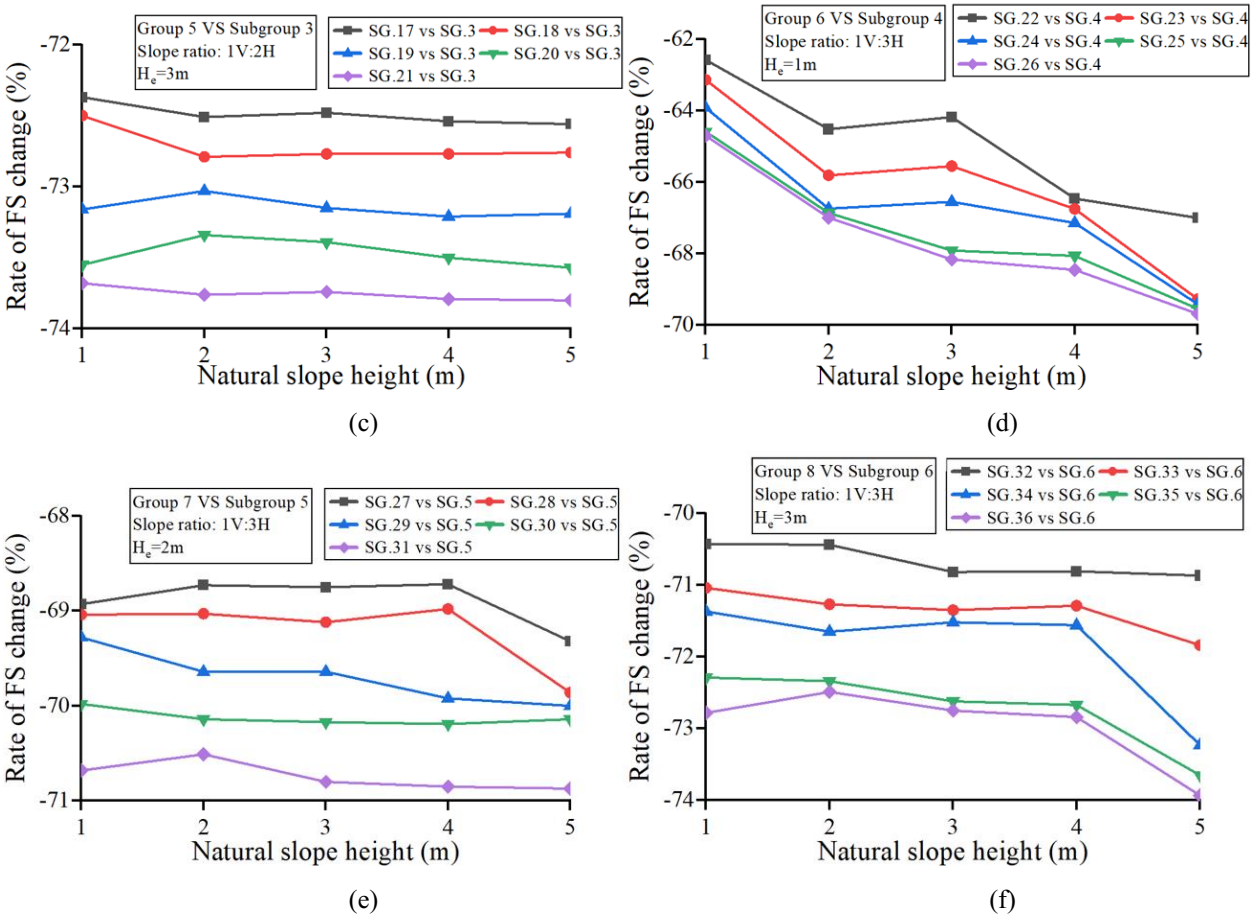

Figure 4.18 Rate of FS change (Set II vs Set I) versus natural slope height in a range of 1 m to 5m with three railway embankment heights (1m, 2m, and 3m), all cases divided into (a) GP. 3 vs SG. 1, (b) GP. 4 vs SG. 2, (c) GP. 5 vs SG. 3, (d) GP. 6 vs SG. 4, (e) GP. 7 vs SG. 5, (f) GP. 8 vs SG. 6 (continued)

In Set II, the lowest FS is 1.76 (3m-high railway embankment, 5m-high natural slope, 1V:2H slope ratio, and a rising water level ratio is 1.0), which is still greater than 1.3. As a result, all models are still stable for the analysis in Set III (rising water level and train load conditions).

4.4 Parameter Study of Models in Set III

4.4.1 Influence of the Slope Geometry for the Model Subjected to Rising Water Levels and Train Loading

Figure 4.19 (a)-(f) shows the FS values for all models in Set III (Group 9-Group 14) with a stationary train load. The simulation parameters the same as those of Set I and Set II: the slope ratio (1V:2H, and 1V:3H), embankment height (1, 2, and 3m), natural slope height (1-5m), and the rising water level ratio (0.2, 0.4, 0.6, 0.8, 1.0). The FS trend is similar to those observed in Set I and Set II with the only difference being that the factor of safety increases with an increasing embankment height. The most stable model is when the embankment height is 3m (Group 14), as presented in Figure 4.19 (f). In addition, the train load added on the track negatively influences the

factor of safety. As such, there are five aspects to discuss regarding the influence of the parameters in Set III:

1. The slope ratio (1V:2H, 1V:3H)
2. The embankment height (H_e= 1, 2, 3m)
3. The natural slope height (H_s= 1, 2, 3, 4, 5m)
4. The rising water level ratio (0.2, 0.4, 0.6, 0.8, 1.0)
5. The train speeds (0 km/h (0 mph) to 120 km/h (75 mph), increased in 8 km/h (5 mph) increments)

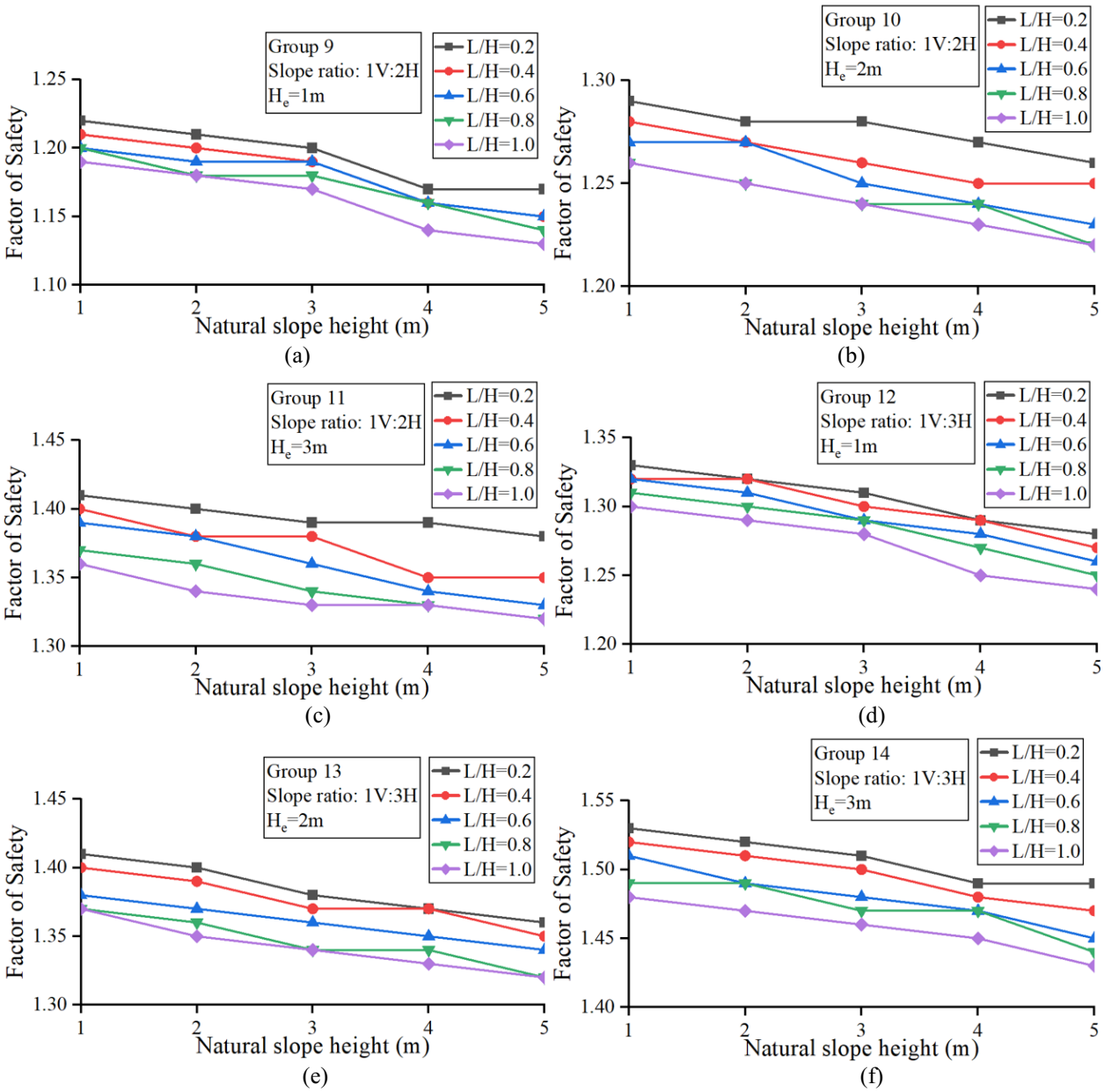

Figure 4.19 FS value with a stationary train on the track versus natural slope height in Group 9-14 in a range of 1m to 5m with three railway embankment heights (1m, 2m, and 3m). (a) Group 9, (b) Group 10, (c) Group 11, (d) Group 12, (d) Group 13, (e) Group 14

1) Influence of the Slope Ratio

Table 4.8 lists all the rates of FS change when the slope ratio increases from 1V:2H to 1V:3H for different railway embankment heights with Group 9 compared to Group 12, Group 10 versus Group 13, and Group 11 compared to Group 14. The rate of change of FS is positive, which indicates that the FS increases when the slope is flatter. However, Figure 4.20 shows that the change in FS does not show a clear trend with the increase of natural slope height. The rate fluctuated from 7% to 10%, and increases in the railway embankment height and rising water level ratio do not significantly affect the rate of change of the FS, with only minor differences being observed. Thus, it is strongly advised to design the slope with a ratio of 1V:3H to achieve optimum stability.

Table 4.8 The FS change rate of models in Group 9 and 12, Group 10 and 13, and Group 11 and 14 (slope ratio of 2H:1V versus 3H:1V)

Embankment height (m)	Group	Subgroup	Rate of FS change (%)				
			Natural slope height (m)				
			1	2	3	4	5
1m	Group 9 VS Group 12	SG37 vs SG52	9.0%	9.1%	9.2%	10.3%	9.4%
		SG38 vs SG53	9.1%	10.0%	10.2%	11.2%	10.4%
		SG39 vs SG54	10.0%	10.1%	10.4%	10.3%	10.6%
		SG40 vs SG55	9.2%	9.5%	9.3%	9.5%	9.6%
		SG41 vs SG56	9.2%	9.3%	9.6%	9.6%	9.7%
2m	Group 10 VS Group 13	SG42 vs SG57	9.3%	9.4%	7.8%	7.8%	7.9%
		SG43 vs SG58	9.4%	9.5%	8.7%	9.6%	8.0%
		SG44 vs SG59	8.7%	7.9%	8.8%	8.9%	8.94%
		SG45 vs SG60	8.7%	8.8%	8.1%	8.1%	8.2%
		SG46 vs SG61	8.7%	8.0%	8.1%	8.1%	8.2%
3m	Group 11 VS Group 14	SG52 vs SG62	8.5%	8.6%	8.6%	8.8%	8.8%
		SG53 vs SG63	8.6%	9.4%	8.0%	9.6%	9.7%
		SG54 vs SG64	8.6%	8.7%	8.8%	9.7%	9.8%
		SG55 vs SG65	8.8%	9.6%	9.7%	10.5%	9.0%
		SG56 vs SG66	8.8%	8.9%	9.0%	9.1%	8.3%

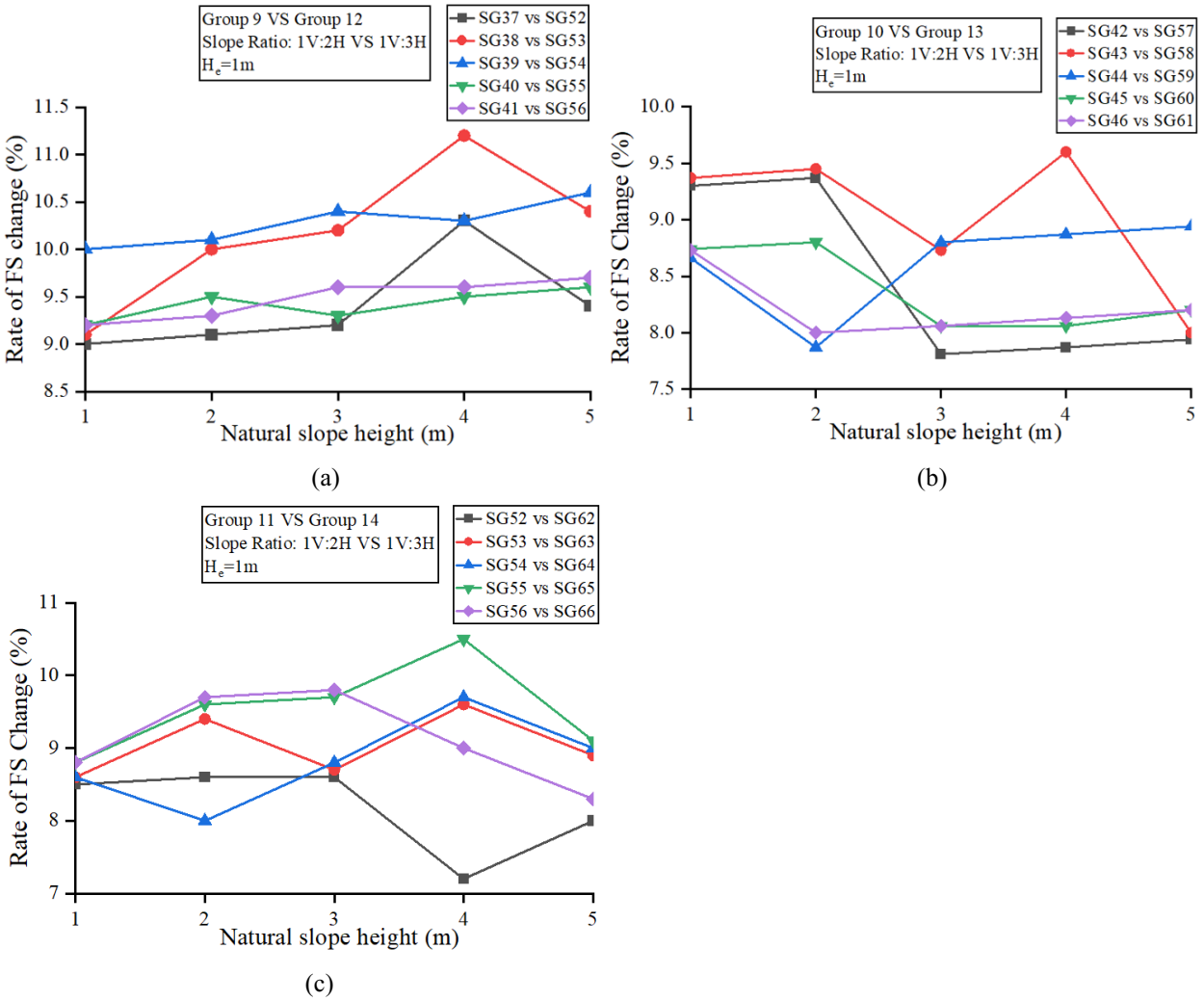

Figure 4.20 Relationship between FS change rate and the natural slope height for models in (a) Group 9 and 12, (b) Group 10 and 13, (a) Group 11 and 14 with a stationary train

2) Influence of the Railway Embankment Height (H_e)

In this thesis, the railway embankment height (H_e) ranges from 1m to 3m. The following two comparisons are discussed in this section: H_e=1m (Group 9 and Group 12) versus H_e=2m (Group 10 and Group 13) with the different slope ratios listed in Table 4.9, and H_e=1m (Group 9 and Group 12) versus H_e=3m (Group 11 and Group 14) listed in Table 4.10.

As shown in Table 4.9, the rate of change of every FS is positive, implying that as the embankment height increases from 1m to 2m, the FS value grows. The FS's rate of change increases slightly as the height of the natural slope increases, with a maximum rate of change of 8%. Furthermore, it can be seen in Figure 4.21 that the rising water level ratio and the slope ratio have no discernible effect on the FS's rate of change.

Table 4.9 FS change rate of models in Group 9, Group 10 and Group 12, Group 13 (railway embankment height of 1m versus 2m) with a stationary locomotive

Embankment height (m)	Slope ratio	Group	Subgroup	Rate of fs change (%)				
				Natural slope height (m)				
				1	2	3	4	5
1m	1V:2H	Group 9 VS Group 10	SG37 vs SG42	5.7%	5.8%	6.7%	8.5%	7.7%
			SG38 vs SG43	5.8%	5.8%	5.9%	7.8%	8.7%
			SG39 vs SG44	5.8%	6.7%	5.0%	6.9%	7.0%
			SG40 vs SG45	5.0%	5.9%	5.1%	6.9%	7.0%
			SG41 vs SG46	5.9%	5.9%	6.0%	7.9%	8.0%
2m	1V:3H	Group 12 VS Group 13	SG52 vs SG57	6.0%	6.1%	5.3%	6.2%	6.3%
			SG53 vs SG58	6.1%	5.3%	5.4%	6.2%	6.3%
			SG54 vs SG59	4.5%	4.6%	5.4%	5.5.%	6.3%
			SG55 vs SG60	4.6%	4.6%	3.9%	5.5%	5.6%
			SG56 vs SG61	5.4%	4.7%	4.7%	6.4%	6.5%

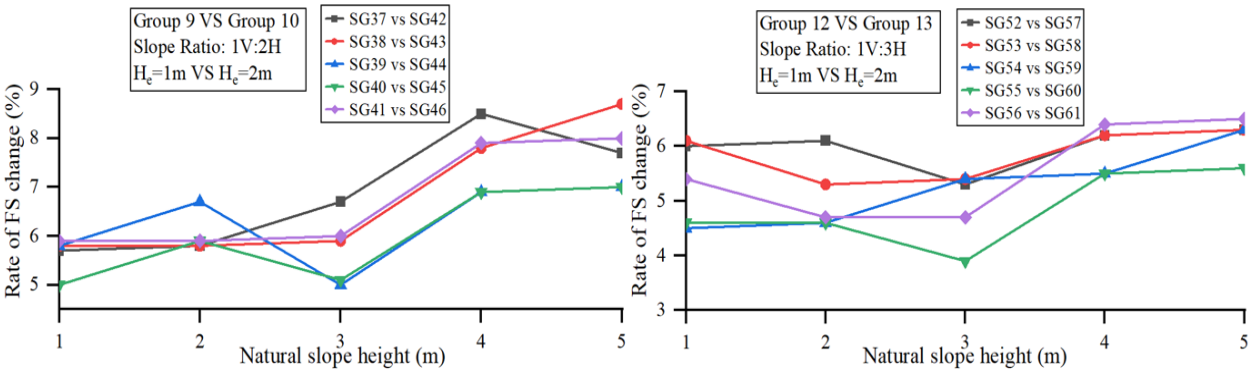

Figure 4.21 Relationship between FS change rate of natural slope height, slope ratio, and railway embankment height (1m to 2m) for the models in Group 9, 10, and Group 12,13 with a stationary locomotive

Table 4.10 shows the FS's rate of change with railway embankment heights ranging from 1m to 3m with different slope ratios. Compared with Table 4.9, all FS rates of change for heights ranging from 1m to 3m are much higher than those for 1m to 2m, but the general trend remains the same whereby the rate of change increases with a larger natural slope height. Similar to Figure 4.21, Figure 4.22 illustrates that the slope ratio and the rising water level ratio have a minor effect on the FS's rate of change. As a result, to build a more stable slope subjected to external static loading, it is preferable to have a 3m-high railway embankment.

Table 4.10 FS change rate of models in Group 9, Group 11 and Group 12, Group 14 (railway embankment height of 1m versus 3m) with a stationary train

Embankment height (m)	Slope ratio	Group	Subgroup	Rate of FS change (%)				
				Natural slope height (m)				
				1	2	3	4	5
1m	1V:2H	Group 9 VS Group 11	SG37 vs SG47	15.6%	15.7%	15.8%	18.8%	17.9%
			SG38 vs SG48	15.7%	15.0%	16.0%	16.4%	17.4%
			SG39 vs SG49	15.8%	16.0%	14.3%	15.5%	15.7%
			SG40 vs SG50	14.2%	15.3%	13.6%	14.7%	15.8%
			SG41 vs SG51	14.3%	13.6%	13.7%	16.7%	16.8%
3m	1V:3H	Group 12 VS Group 14	SG52 vs SG62	15.0%	15.2%	15.3%	15.5%	16.4%
			SG53 vs SG63	15.2%	14.4%	15.4%	14.7%	15.7%
			SG54 vs SG64	14.4%	13.7%	14.7%	14.8%	15.1%
			SG55 vs SG65	13.7%	14.6%	14.0%	15.7%	15.2%
			SG56 vs SG66	13.8%	14.0%	14.1%	16.0%	15.3%

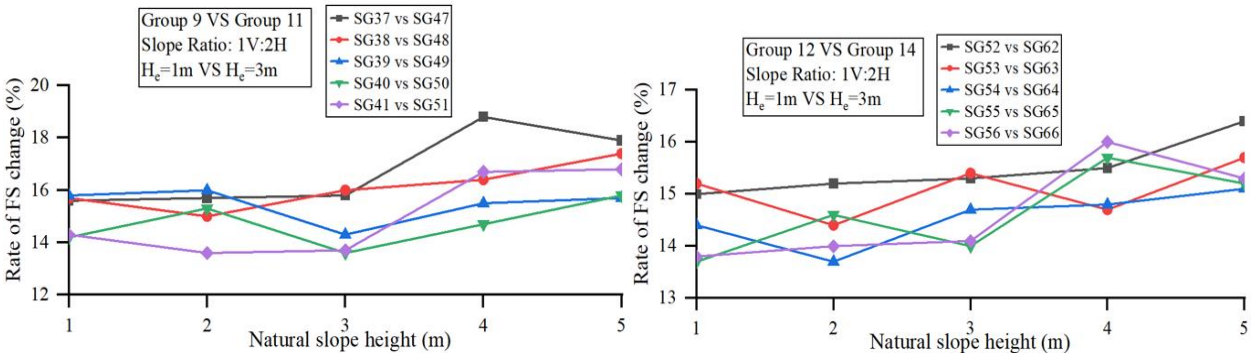

Figure 4.22 Relationship between FS change rate of natural slope height, slope ratio, and railway embankment height (1m to 3m) for the models in Group 9, 11, and Group 12,14 with a stationary train

3) Influence of the Natural Slope Height (H_s)

This section discusses how the natural slope height affects the FS. Three comparisons are made based on different railway embankment heights (H_e=1m, 2m, 3m) to demonstrate the influence of natural slope heights. In each comparison, FS values for a natural slope height greater than 1m are compared to those with 1m slope heights. Table 4.11 shows the rate of FS change for different natural slope heights when H_e=1m with different slope ratios (all the subgroups in Group 9 and Group 12). All the FS change rates are negative, ranging from 0% to -5%, which means that as the natural slope height becomes larger, the FS tends to decrease for any rising water level ratio. Moreover, In Figure 4.23, the reduction in FS continuously increased for greater natural slope heights. However, the FS's rate of change appears to be insensitive to increases in the rising water ratio and slope ratio.

Table 4.11 FS change rate of models in Group 9 and Group 12 in different natural slope heights (when railway embankment height is 1m) with a stationary train

Embankment height (m)	Slope ratio	Group	Subgroup	Rate of fs change (%)				
				Natural slope height (m)				
				1	2	3	4	5
1m	1V:2H	Group 9	SG37	0%	-0.8%	-1.6%	-4.1%	-4.1%
			SG38	0%	-0.8%	-1.7%	-4.1%	-5.0%
			SG39	0%	-0.8%	-0.8%	-3.3%	-4.2%
			SG40	0%	-1.7%	-1.7%	-3.3%	-5.0%
			SG41	0%	-0.8%	-1.7%	-4.2%	-5.0%
	1V:3H	Group 12	SG52	0%	-0.8%	-1.5%	-3.0 %	-3.8%
			SG53	0%	0%	-1.5%	-2.3%	-3.8%
			SG54	0%	-0.8%	-2.3%	-3.0%	-4.5%
			SG55	0%	-0.8%	-1.5%	-3.1%	-4.6%
			SG56	0%	-0.8%	-1.5%	-3.8%	-4.6%

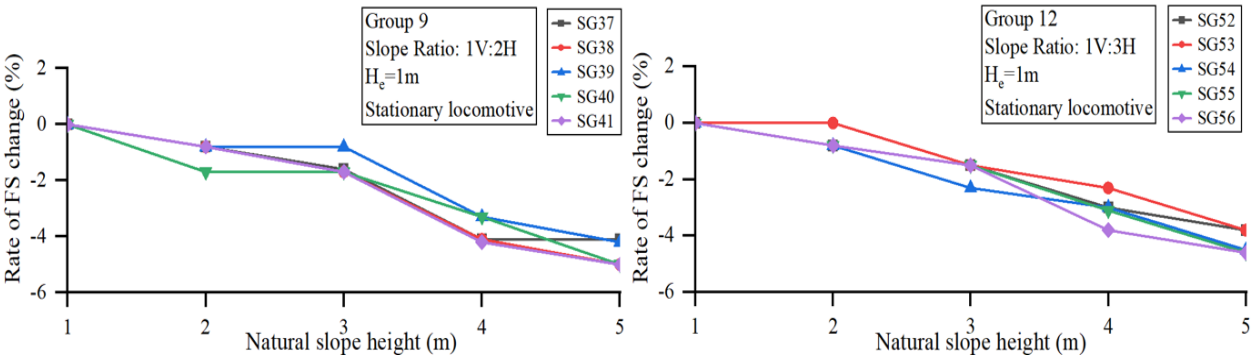

Figure 4.23 Relationship between FS change rate of natural slope height (1m to 5m) with embankment height is 1m for the models in Group 9 and Group 12 with a stationary train

Table 4.12 lists the rate of FS change versus different natural slope heights when H_e=2m with different slope ratios (all the subgroups in Group 10 and Group 13). Compared with Table 4.11, when railway embankment height is 2m, the rate of change of the FS increases but only within a limited range of values.

Table 4.12 FS change rate of models in Group 10 and Group 13 in different natural slope heights (when railway embankment height is 2m) with a stationary train

Embankment height (m)	Slope ratio	Group	Subgroup	Rate of fs change (%)				
				Natural slope height (m)				
				1	2	3	4	5
2m	1V:2H	Group 9	SG37	0%	-0.8%	-1.6%	-4.1%	-4.1%
			SG38	0%	-0.8%	-1.7%	-4.1%	-5.0%
			SG39	0%	-0.8%	-0.8%	-3.3%	-4.2%
			SG40	0%	-1.7%	-1.7%	-3.3%	-5.0%
			SG41	0%	-0.8%	-1.7%	-4.2%	-5.0%
	1V:3H	Group 12	SG52	0%	-0.8%	-1.5%	-3.0 %	-3.8%
			SG53	0%	0%	-1.5%	-2.3%	-3.8%
			SG54	0%	-0.8%	-2.3%	-3.0%	-4.5%
			SG55	0%	-0.8%	-1.5%	-3.1%	-4.6%
			SG56	0%	-0.8%	-1.5%	-3.8%	-4.6%

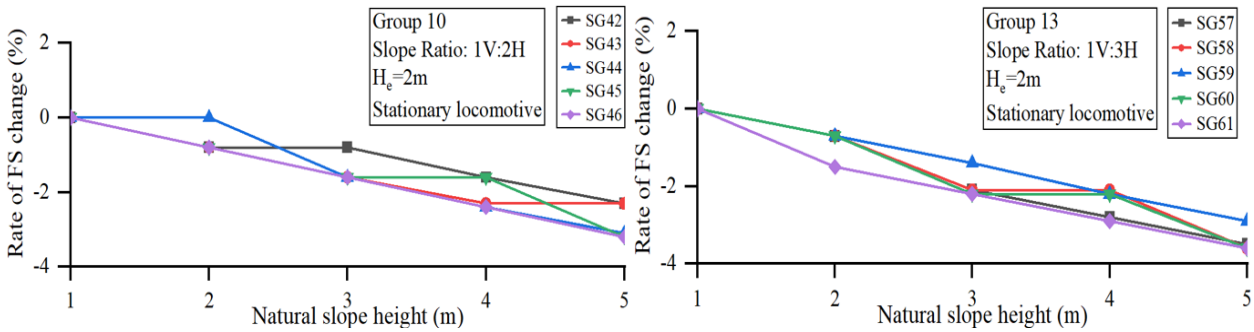

Figure 4.24 Relationship between FS change rate of natural slope height (1m to 5m) with embankment height is 2m for the models in Group 10 and Group 13 with a stationary train

The rate of FS change for different natural slope heights when H_e = 3m is summarized in Table 4.13. In this part, all the trends are similar to the previous parts. The FS's rate of change continuously increases with an increase in the natural slope's height. Additionally, the slope ratio and railway embankment height do not influence the rate of FS change. Based on the analysis, a higher natural slope height is recommended for slope safety.

Table 4.13 FS change rate of models in Group 11 and Group 14 in different natural slope heights (when railway embankment height is 3m) with a stationary train

Embankment height (m)	Slope ratio	Group	Subgroup	Rate of fs change (%)				
				Natural slope height (m)				
				1	2	3	4	5
3m	1V:2H	Group 9	SG37	0%	-0.8%	-1.6%	-4.1%	-4.1%
			SG38	0%	-0.8%	-1.7%	-4.1%	-5.0%
			SG39	0%	-0.8%	-0.8%	-3.3%	-4.2%
			SG40	0%	-1.7%	-1.7%	-3.3%	-5.0%
			SG41	0%	-0.8%	-1.7%	-4.2%	-5.0%
	1V:3H	Group 12	SG52	0%	-0.8%	-1.5%	-3.0 %	-3.8%
			SG53	0%	0%	-1.5%	-2.3%	-3.8%
			SG54	0%	-0.8%	-2.3%	-3.0%	-4.5%
			SG55	0%	-0.8%	-1.5%	-3.1%	-4.6%
			SG56	0%	-0.8%	-1.5%	-3.8%	-4.6%

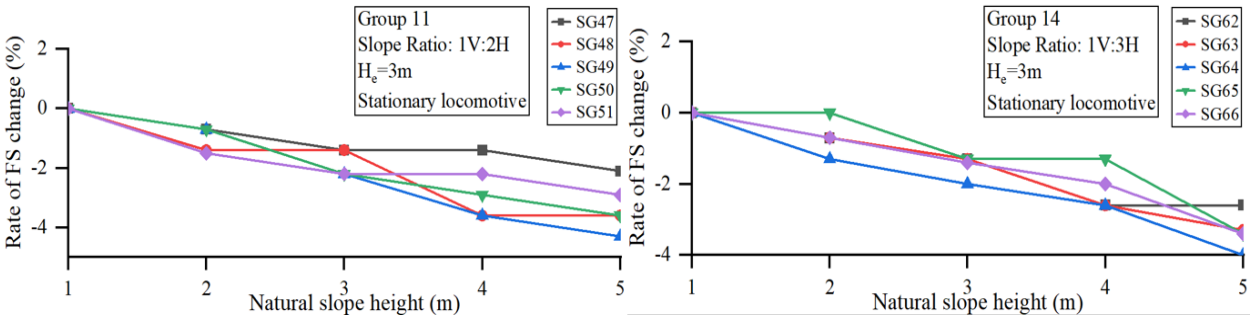

Figure 4.25 Relationship between FS change rate of natural slope height (1m to 5m) with embankment height is 3m for the models in Group 11 and Group 14 with a stationary train

4) Influence of the Rising Water Level Ratio (L/H)

Similar to the analysis of the natural slope height, the study of the water level rising ratio is divided into six batches based on different railway embankment heights and slope ratios. The first three batches as described in Table 4.14, Table 4.15, and Table 4.16, correspond to FS values obtained for rising water level ratios greater than 0.2 and are compared to the case where the rising water level ratio is equal to 0.2. The following three batches, Table 4.17, Table 4.18, and Table 4.19, correspond to FS values for varying rising water level ratios compared to slopes with functioning drain pipes (Subgroup 1 to Subgroup 6). In Table 4.14, all the rates of change of the FS are negative. Thus, the FS declines with an increasing rising water level ratio. It can be observed in Figure 4.26 that the rate of FS change is mildly increasing with the growth of the natural slope height. The slope ratio does not appear to have a direct influence on the FS's rate of change.

Table 4.14 FS change rate of models in Group 9 and Group 12 in different rising water level ratios (railway embankment height is 1m) with a stationary train

Embankment height (m)	Slope ratio	Group	Subgroup	Rate of FS change (%)				
				Natural slope height (m)				
				1	2	3	4	5
1m	1V:2H	Group 9	SG38 vs SG37	-0.8%	-0.8%	-0.8%	-0.9%	-1.7%
			SG39 vs SG37	-1.6%	-1.7%	-0.8%	-0.9%	-1.7%
			SG40 vs SG37	-1.6%	-2.5%	-1.7%	-0.9%	-2.6%
			SG41 vs SG37	-2.5%	-1.7%	-2.5%	-2.6%	-3.4%
	1V:3H	Group 12	SG53 vs SG52	-0.8%	0%	-0.8%	0%	-0.8%
			SG54 vs SG52	-0.8%	-0.8%	-1.5%	-0.8%	-1.6%
			SG55 vs SG52	-1.5%	-1.5%	-1.5%	-1.6%	-2.3%
			SG56 vs SG62	-2.3%	-2.3%	-2.3%	-3.1%	-3.1%

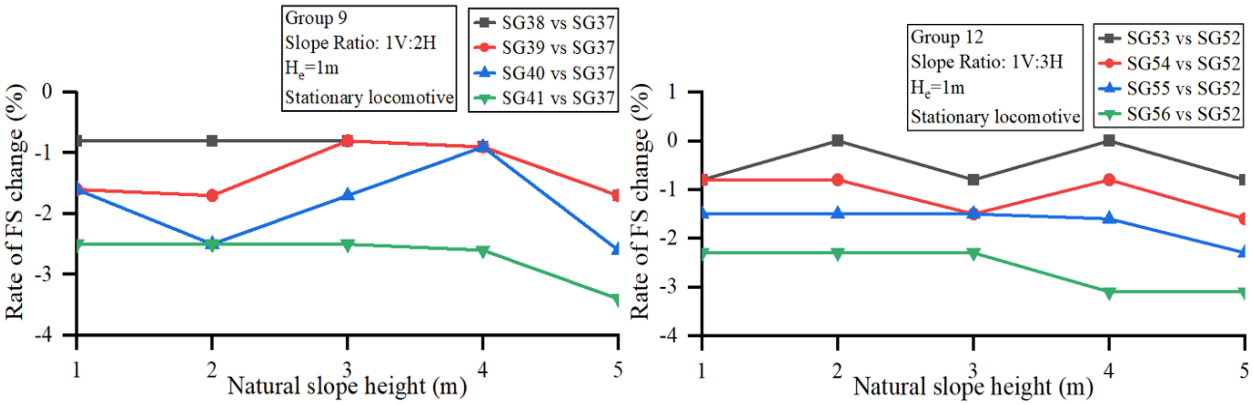

Figure 4.26 Relationship between FS change rate of water level rising ratios (0.2m to 1.0m) versus the natural slope heigh in different slope ratios for the models in Group 9 and Group 12 with a stationary train

When the railway embankment height increases to 2m, the rate of FS change is similar to those observed in the previous batches as shown in Table 4.15. In Figure 4.27, when the slope ratio is 1V:2H, the rate of change of the FS shows a similar trend as that in Figure 4.26. The rate of change increases with an increase in the natural slope height while in Group 13, the rate of change slightly decreases in response to an increase in natural slope height.

Table 4.15 FS change rate of models in Group 10 and Group 13 in different water level rising ratios (railway embankment height is 2m) with a stationary train

Embankment height (m)	Slope ratio	Group	Subgroup	Rate of FS change (%)				
				Natural slope height (m)				
				1	2	3	4	5
2m	1V:2H	Group 10	SG43 vs SG42	-0.8%	-0.8%	-1.6%	-1.6%	-0.8%
			SG44 vs SG42	-1.6%	-0.8%	-2.3%	-2.4%	-2.4%
			SG45 vs SG42	-2.3%	-2.3%	-3.1%	-2.4%	-3.2%
			SG46 vs SG42	-2.3%	-2.3%	-3.1%	-3.1%	-3.2%
	1V:3H	Group 13	SG58 vs SG57	-0.7%	-0.7%	-0.7%	0%	-0.8%
			SG59 vs SG57	-2.1%	-2.1%	-1.4%	-0.8%	-1.6%
			SG60 vs SG57	-2.8%	-2.9%	-2.9%	-1.6%	-2.3%
			SG61 vs SG57	-2.8%	-3.6%	-2.3%	-3.1%	-3.1%

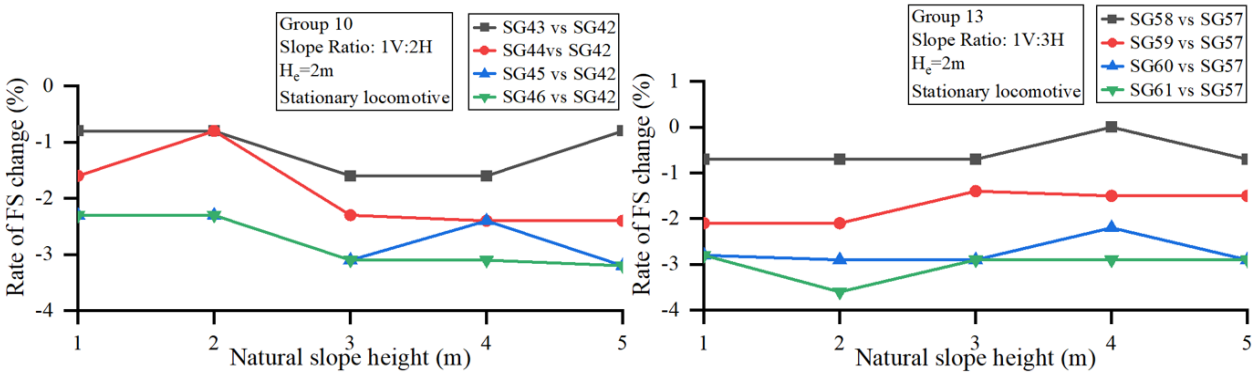

Figure 4.27 Relationship between FS change rate of water level rising ratios (0.2m to 1.0m) versus the natural slope heigh in different slope ratios for the models in Group 10 and Group 13 with a stationary train

For models with a 3-m railway embankment height, Table 4.16 and Figure 4.28 shows all the FS change rates and the trends. Like the first batch (H_e=1m), all the FS change rates show an increasing tendency with the growing natural slope height and rising water level ratio.

Table 4.16 FS change rate of models in Group 11 and Group 14 in different water level rising ratios (railway embankment height is 3m) with a stationary train

Embankment height (m)	Slope ratio	Group	Subgroup	Rate of FS change (%)				
				Natural slope height (m)				
				1	2	3	4	5
3m	1V:2H	Group 10	SG43 vs SG42	-0.8%	-0.8%	-1.6%	-1.6%	-0.8%
			SG44 vs SG42	-1.6%	-0.8%	-2.3%	-2.4%	-2.4%
			SG45 vs SG42	-2.3%	-2.3%	-3.1%	-2.4%	-3.2%
			SG46 vs SG42	-2.3%	-2.3%	-3.1%	-3.1%	-3.2%
	1V:3H	Group 13	SG58 vs SG57	-0.7%	-0.7%	-0.7%	0%	-0.8%
			SG59 vs SG57	-2.1%	-2.1%	-1.4%	-0.8%	-1.6%
			SG60 vs SG57	-2.8%	-2.9%	-2.9%	-1.6%	-2.3%
			SG61 vs SG57	-2.8%	-3.6%	-2.3%	-3.1%	-3.1%

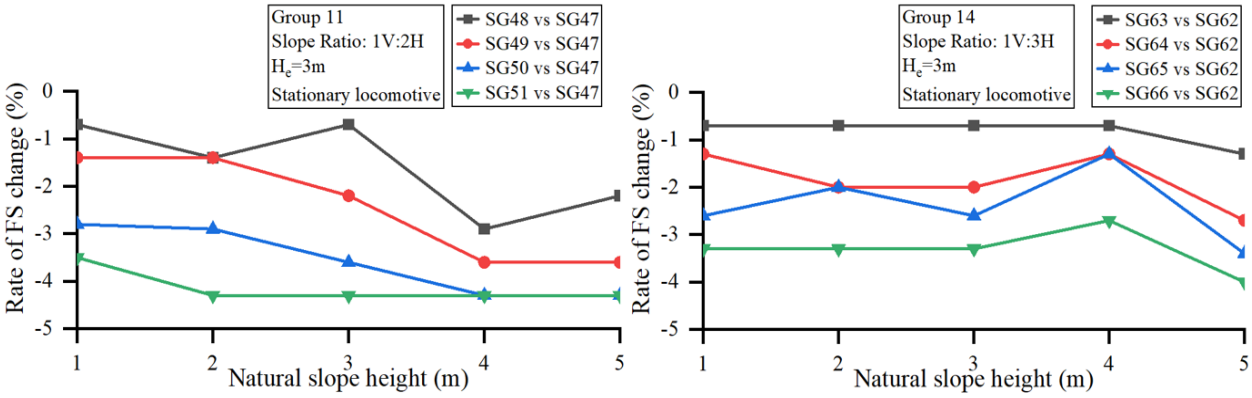

Figure 4.28 Relationship between FS change rate of water level rising ratios (0.2m to 1.0m) versus the natural slope heigh in different slope ratios for the models in Group 11 and Group 14 with a stationary train

The subsequent three batches, Table 4.17, Table 4.18, and Table 4.19 are a slope with rising water level compared to a slope with a functioning pipe. Similar to the above three batches, Table 4.17 and Figure 4.29 list the FS rates of change and their trends. All the rates of FS change are negative and range from -83% to -85%, which indicates that the rising water level plays an essential role in reducing the FS. Moreover, when the natural slope height increases, every FS rate of change decreases in a quasi-linear fashion. At the same time, the different slope ratios do not affect the rates.

Table 4.17 FS change rate of models in Group 9 and Group 12 in different water level rising ratios compared with dry slope (Subgroup 1 and Subgroup 4) (H_e=1m) with a stationary train

Embankment height (m)	Slope ratio	Group	Subgroup	Rate of FS change (%)				
				Natural slope height (m)				
				1	2	3	4	5
1m	1V:2H	Group 9	SG37 vs SG1	-85.8%	-84.5%	-83.7%	-83.3%	-82.8%
			SG38 vs SG1	-85.7%	-84.7%	-83.8%	-83.5%	-83.1%
			SG39 vs SG1	-85.9%	-84.8%	-83.8%	-83.5%	-83.1%
			SG40 vs SG1	-85.9%	-84.9%	-83.9%	-83.5%	-83.2%
			SG41 vs SG1	-86.0%	-84.9%	-84.1%	-83.8%	-83.4%
	1V:3H	Group 12	SG52 vs SG4	-85.2%	-84.5%	-83.7%	-83.2%	-82.7%
			SG53 vs SG4	-85.3%	-84.5%	-83.8%	-83.2%	-82.9%
			SG54 vs SG4	-85.3%	-84.7%	-84.0%	-83.3%	-83.0%
			SG55 vs SG4	-85.4%	-84.8%	-84.0%	-83.4%	-83.2%
			SG56 vs SG4	-85.5%	-84.9%	-84.1%	-83.7%	-83.3%

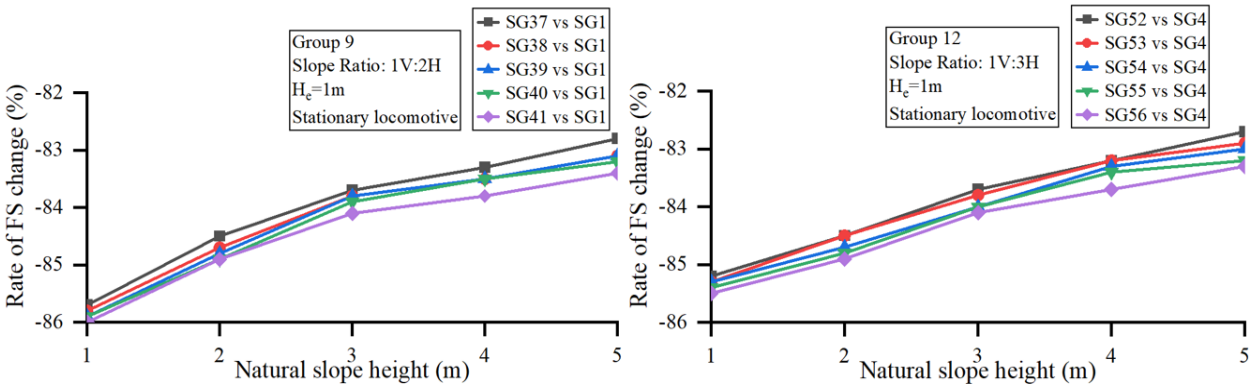

Figure 4.29 Relationship between FS change rate of dry slope to different rising water level ratios versus the natural slope heigh in different slope ratios for the models in Group 9 and Group 12 with a stationary train

Figure 4.30 indicates that the FS rate of change for a 2m-high railway embankment follows the same trend as the railway embankments with a height of 1m, where it decreases when the natural slope height increases. However, the rates are slightly lower than those shown in Table 4.18 which range from -81% to -84%.

Table 4.18 FS change rate of models in Group 10 and Group 13 in different water level rising ratios compared with dry slope (Subgroup 2 and Subgroup 5) (H_e=2m) with a stationary train

Embankment height (m)	Slope ratio	Group	Subgroup	Rate of FS change (%)				
				Natural slope height (m)				
				1	2	3	4	5
2m	1V:2H	Group 10	SG37 vs SG1	-85.8%	-84.5%	-83.7%	-83.3%	-82.8%
			SG38 vs SG1	-85.7%	-84.7%	-83.8%	-83.5%	-83.1%
			SG39 vs SG1	-85.9%	-84.8%	-83.8%	-83.5%	-83.1%
			SG40 vs SG1	-85.9%	-84.9%	-83.9%	-83.5%	-83.2%
			SG41 vs SG1	-86.0%	-84.9%	-84.1%	-83.8%	-83.4%
	1V:3H	Group 13	SG52 vs SG4	-85.2%	-84.5%	-83.7%	-83.2%	-82.7%
			SG53 vs SG4	-85.3%	-84.5%	-83.8%	-83.2%	-82.9%
			SG54 vs SG4	-85.3%	-84.7%	-84.0%	-83.3%	-83.0%
			SG55 vs SG4	-85.4%	-84.8%	-84.0%	-83.4%	-83.2%
			SG56 vs SG4	-85.5%	-84.9%	-84.1%	-83.7%	-83.3%

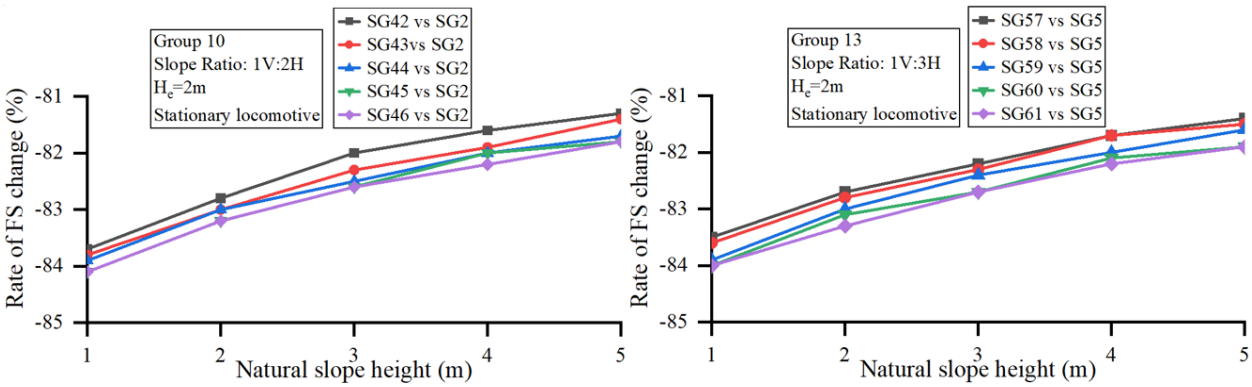

Figure 4.30 Relationship between FS change rate of dry slope to different water level rising ratios versus the natural slope heigh in different slope ratios for the models in Group 10 and Group 13 with a stationary train

When the embankment is 3m-high, the FS change rates decline slightly further, ranging from -79% to -81%, but still share the same trend when the height of the natural slope increases.

Table 4.19 FS change rate of models in Group 11 and Group 14 in different water level rising ratios compared with dry slope (Subgroup 3 and Subgroup 6) (H_e=3m) with a stationary train

Embankment height (m)	Slope ratio	Group	Subgroup	Rate of FS change (%)				
				Natural slope height (m)				
				1	2	3	4	5
3m	1V:2H	Group 11	SG37 vs SG1	-85.8%	-84.5%	-83.7%	-83.3%	-82.8%
			SG38 vs SG1	-85.7%	-84.7%	-83.8%	-83.5%	-83.1%
			SG39 vs SG1	-85.9%	-84.8%	-83.8%	-83.5%	-83.1%
			SG40 vs SG1	-85.9%	-84.9%	-83.9%	-83.5%	-83.2%
			SG41 vs SG1	-86.0%	-84.9%	-84.1%	-83.8%	-83.4%
	1V:3H	Group 14	SG52 vs SG4	-85.2%	-84.5%	-83.7%	-83.2%	-82.7%
			SG53 vs SG4	-85.3%	-84.5%	-83.8%	-83.2%	-82.9%
			SG54 vs SG4	-85.3%	-84.7%	-84.0%	-83.3%	-83.0%
			SG55 vs SG4	-85.4%	-84.8%	-84.0%	-83.4%	-83.2%
			SG56 vs SG4	-85.5%	-84.9%	-84.1%	-83.7%	-83.3%

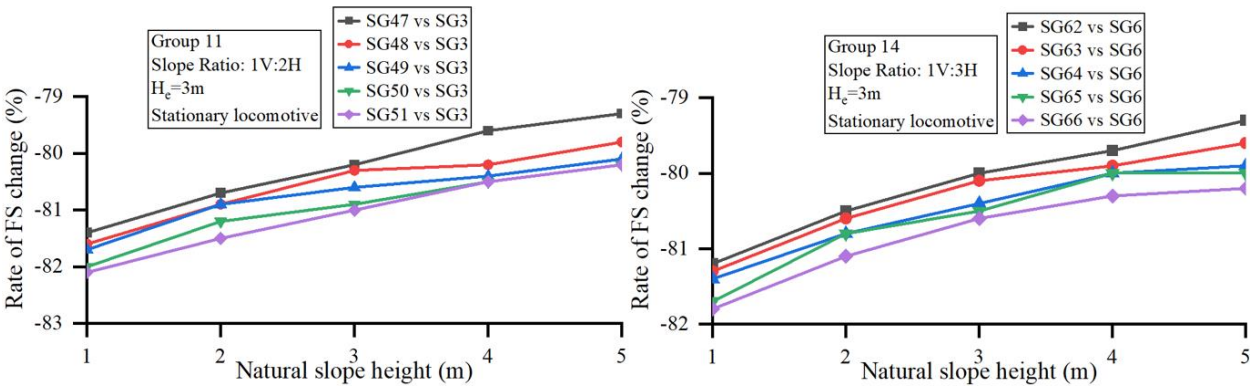

Figure 4.31 Relationship between FS change rate of dry slope to different water level rising ratios versus the natural slope heigh in different slope ratios for the models in Group 11 and Group 14 with a stationary train

5) Influence of the Train Speed

This part deals with the models with a moving train on the tracks, a 1m-high railway embankment, a slope ratio is 1V:3H, and a rising water level ratio ranging from 0.2 to 1.0 (Group 12). The train speed ranges from 0 km/h (0 mph) to 120 km/h (75 mph) and is increased in 8 km/h (5 mph) increments. Table 4.20 lists all the corresponding FS values for Group 12 with various train speeds and a rising water level ratio ranging from 0.2 to 1.0. The FS decreases with increasing train speed.

Figure 4.32 shows the FS in Subgroup 52 to Subgroup 56. Each chart indicates the relationship between the FS, the height of the natural slope, and the train speed. The color scale is the same for

every graph with a minimum of 1.00 and a maximum of 1.33. The FS value is larger with a lower train speed and a smaller natural slope height.

Table 4.20 FS values of models in Group 12 under different train speeds with water level rising ratio of 0.2 to 1.0

Groups	Subgroups	Train speed (km/h)	Train speed (mph)	FS				
				Natural slope height (Hs) (m)				
				1	2	3	4	5
Group 12	Subgroup 52	0	0	1.33	1.32	1.31	1.29	1.28
		8	5	1.31	1.30	1.29	1.27	1.28
		16	10	1.29	1.28	1.27	1.25	1.26
		24	15	1.28	1.27	1.26	1.25	1.24
		32	20	1.27	1.26	1.25	1.23	1.23
		40	25	1.26	1.24	1.24	1.22	1.21
		48	30	1.24	1.23	1.22	1.21	1.20
		56	35	1.23	1.22	1.21	1.20	1.20
		64	40	1.22	1.21	1.19	1.18	1.19
		72	45	1.20	1.29	1.18	1.17	1.18
		80	50	1.19	1.18	1.16	1.15	1.17
		88	55	1.19	1.17	1.15	1.13	1.15
		96	60	1.18	1.17	1.14	1.13	1.12
		104	65	1.16	1.14	1.14	1.12	1.11
		112	70	1.15	1.13	1.12	1.11	1.09
		120	75	1.13	1.11	1.10	1.09	1.08
	Subgroup 53	0	0	1.32	1.32	1.3	1.29	1.27
		8	5	1.30	1.30	1.28	1.27	1.25
		16	10	1.28	1.28	1.26	1.25	1.23
		24	15	1.27	1.27	1.25	1.25	1.22
		32	20	1.26	1.26	1.25	1.23	1.21
		40	25	1.24	1.24	1.23	1.22	1.20
		48	30	1.23	1.22	1.21	1.21	1.19
		56	35	1.22	1.21	1.20	1.20	1.18
		64	40	1.20	1.19	1.18	1.17	1.16
		72	45	1.19	1.18	1.16	1.15	1.14
		80	50	1.18	1.17	1.16	1.14	1.13
		88	55	1.17	1.16	1.15	1.13	1.12

Table 4.20 FS values of models in Group 12 under different train speeds with water level rising ratio of 0.2 to 1.0 (continued)

Groups	Subgroups	Train speed (km/h)	Train speed (mph)	FS				
				Natural slope height (Hs) (m)				
				1	2	3	4	5
		96	60	1.15	1.13	1.13	1.10	1.09
		104	65	1.14	1.13	1.11	1.10	1.09
		112	70	1.13	1.11	1.100	1.09	1.08
		120	75	1.12	1.10	1.09	1.08	1.07
	Subgroup 54	0	0	1.32	1.31	1.29	1.28	1.26
		8	5	1.30	1.29	1.27	1.26	1.24
		16	10	1.28	1.27	1.25	1.24	1.22
		24	15	1.27	1.26	1.24	1.23	1.21
		32	20	1.26	1.25	1.23	1.22	1.20
		40	25	1.24	1.23	1.21	1.2	1.19
		48	30	1.23	1.22	1.21	1.19	1.18
		56	35	1.22	1.21	1.19	1.18	1.16
		64	40	1.2	1.19	1.18	1.16	1.15
		72	45	1.19	1.18	1.16	1.15	1.15
		80	50	1.19	1.17	1.15	1.14	1.13
		88	55	1.18	1.15	1.14	1.12	1.11
		96	60	1.16	1.14	1.13	1.11	1.10
		104	65	1.15	1.14	1.12	1.11	1.09
		112	70	1.13	1.12	1.11	1.10	1.09
		120	75	1.12	1.100	1.09	1.09	1.08
	Subgroup 55	0	0	1.31	1.30	1.29	1.27	1.25
		8	5	1.29	1.28	1.27	1.25	1.23
		16	10	1.27	1.26	1.25	1.23	1.22
		24	15	1.26	1.25	1.24	1.22	1.21
		32	20	1.25	1.24	1.23	1.21	1.20
		40	25	1.23	1.21	1.21	1.20	1.18
		48	30	1.22	1.21	1.20	1.18	1.17
		56	35	1.21	1.20	1.19	1.17	1.16
		64	40	1.19	1.18	1.17	1.16	1.14
		72	45	1.18	1.18	1.16	1.15	1.14

Table 4.20 FS values of models in Group 12 under different train speeds with water level rising ratio of 0.2 to 1.0 (continued)

Groups	Subgroups	Train speed (km/h)	Train speed (mph)	FS				
				Natural slope height (*Hs*) (m)				
				1	2	3	4	5
		80	50	1.17	1.16	1.15	1.14	1.12
		88	55	1.15	1.14	1.13	1.12	1.11
		96	60	1.14	1.13	1.12	1.11	1.09
		104	65	1.14	1.12	1.11	1.1	1.08
		112	70	1.12	1.10	1.09	1.08	1.06
		120	75	1.10	1.09	1.07	1.07	1.06
	Subgroup 56	0	0	1.31	1.30	1.29	1.27	1.25
		8	5	1.29	1.28	1.27	1.25	1.23
		16	10	1.27	1.26	1.25	1.23	1.22
		24	15	1.26	1.25	1.24	1.22	1.21
		32	20	1.25	1.24	1.23	1.21	1.20
		40	25	1.23	1.21	1.21	1.20	1.18
		48	30	1.22	1.21	1.2	1.18	1.17
		56	35	1.21	1.20	1.19	1.17	1.16
		64	40	1.19	1.18	1.17	1.16	1.14
		72	45	1.18	1.18	1.16	1.15	1.14
		80	50	1.17	1.16	1.15	1.14	1.12
		88	55	1.15	1.14	1.13	1.12	1.11
		96	60	1.14	1.13	1.12	1.11	1.09
		104	65	1.14	1.12	1.11	1.10	1.08
		112	70	1.12	1.10	1.09	1.08	1.06
		120	75	1.10	1.09	1.07	1.07	1.06

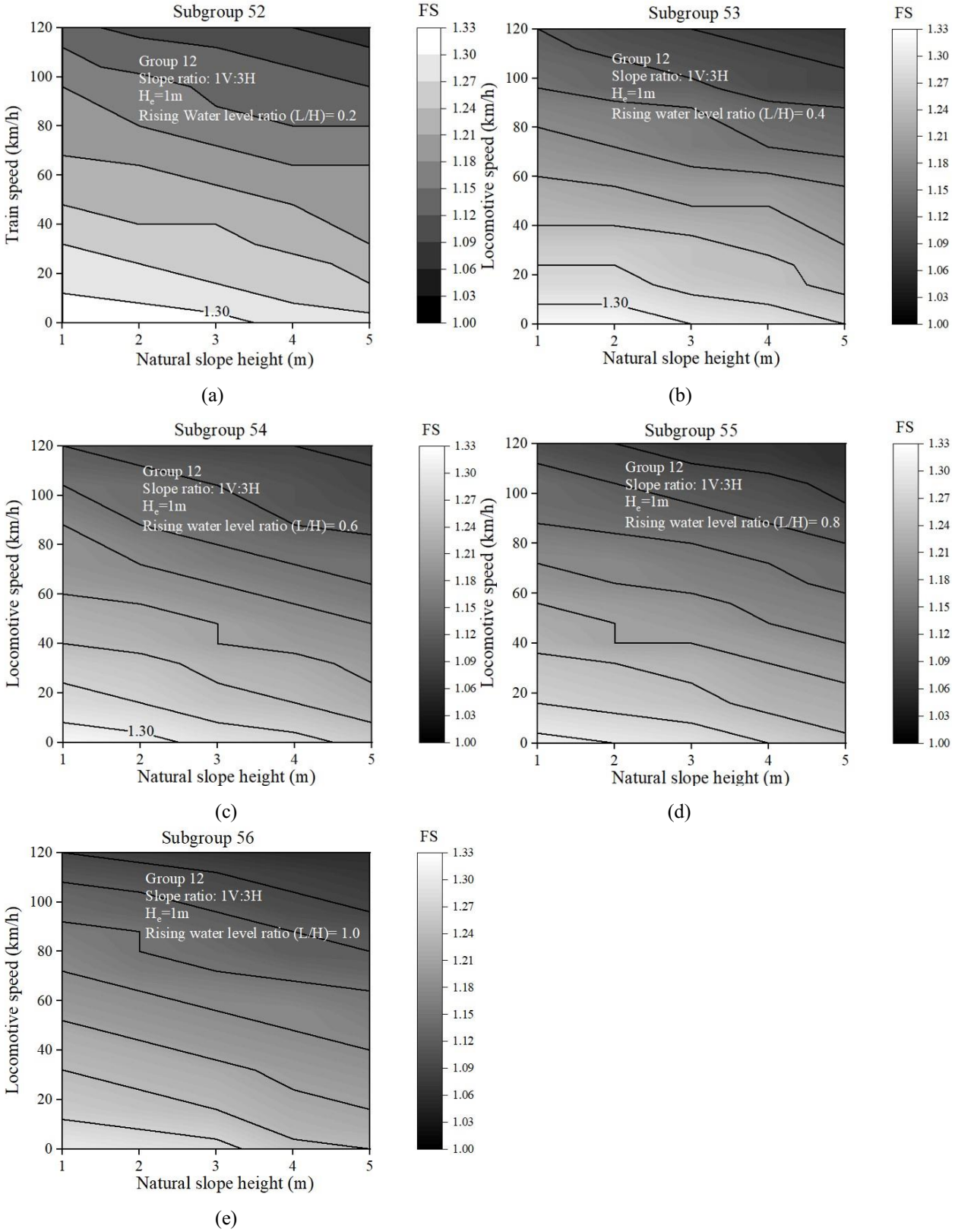

Figure 4.32 Pseudo color graphs of FS values for subgroup 52 to 56. (a) slope ratio 0.2; (b) 0.4; (c) 0.6; (d) 0.8; and (e) 1.0. The grayscale with a min of 1.00 and a max of 1.33 for each

4.4.2 General Stability Trends of Under Rising Water Level and Train Loads Conditions

Figure 4.33 shows the FS trends observed in models belonging to Set I, Set II, and Set III. Those graphs show that the rising water level ratio of the models in Set II and Set III is 1.0. In Set III, the train is considered a stationary train (ABP= 237.8 kPa) while the slope ratio may be 1V:2H or 1V:3H. The y-axis represents the rate of change of the FS between models in different sets.

It can be seen that the slope stability decreases significantly by at least 70% when the rising water level ratio is 1.0 (Set II versus Set I). Moreover, FS values decrease by at least 80% when a stationary train is present on the tracks. When Set II is compared to Set I, the FS's rate of change increases by -70% to -74% when the railway embankment height (H_e) increases. For Set III versus Set II, when the external load is applied on the tacks, the largest reduction in the FS is observed with a corresponding decrease ranging -84% to -80% when the natural slope height becomes higher. However, the slope ratio is insensitive to the FS change.

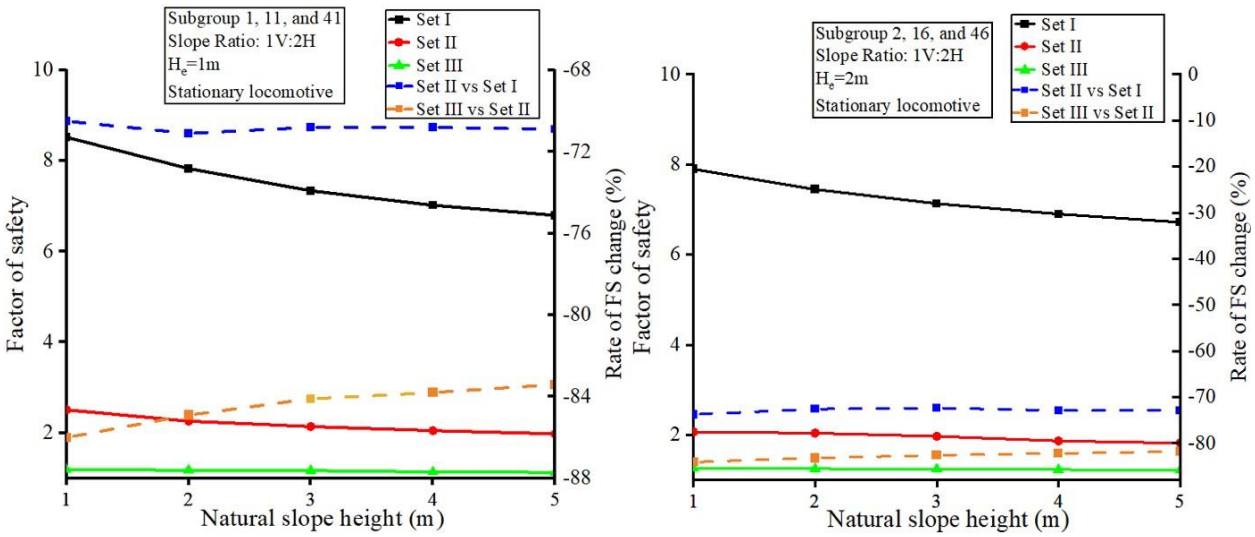

(a) (b)

Figure 4.33 Relationships between the FS values and FS change rate under different Sets versus the natural slope height for models in (a) Subgroup 1, 11, and 41, (b) Subgroup 2, 16, and 46. (c) Subgroup 3, 21, and 51, (d) Subgroup 4, 26, and 56, (e) Subgroup 5, 31, and 61, (f) Subgroup 6, 36, and 66

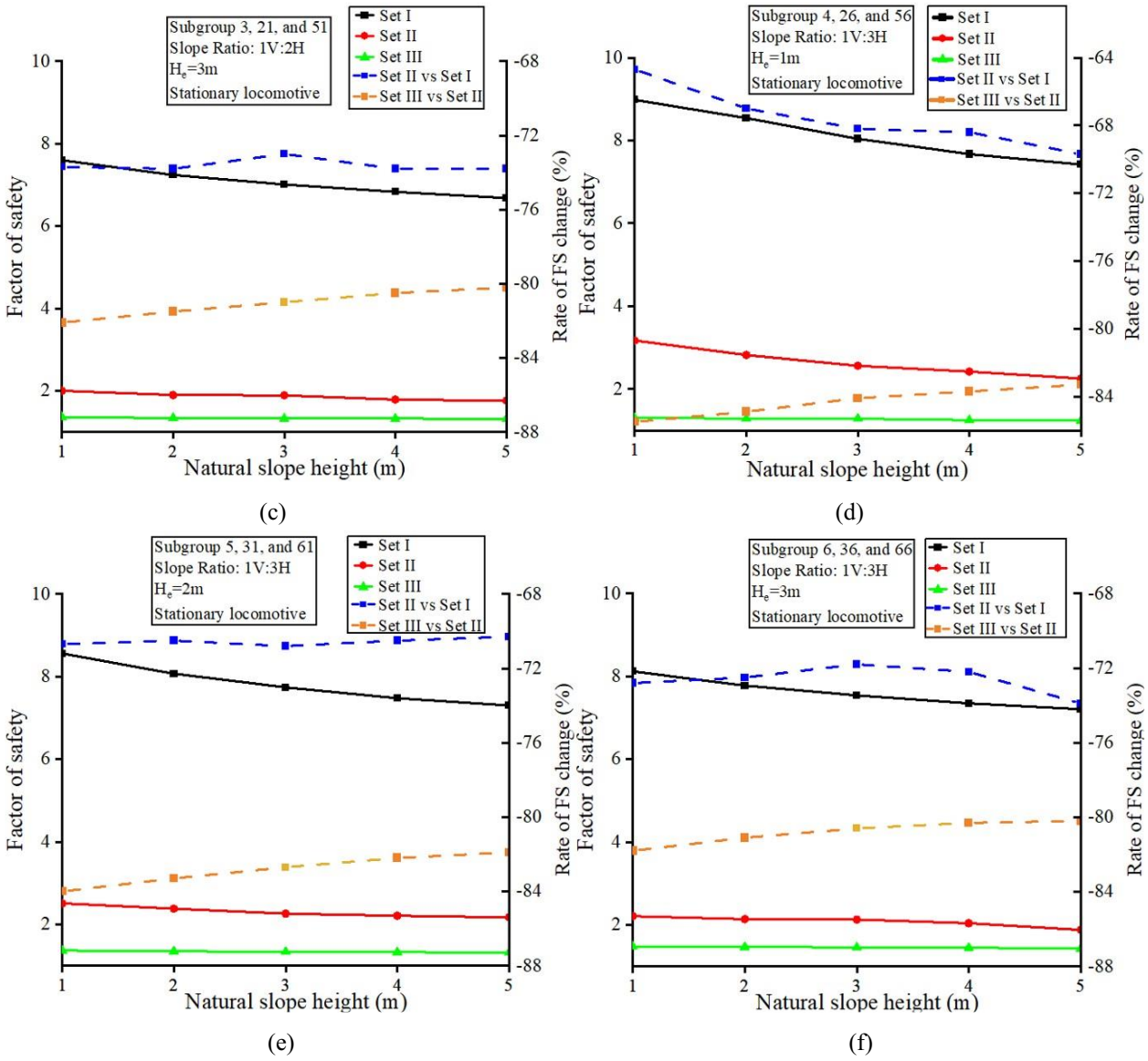

Figure 4.33 Relationships between the FS values and FS change rate under different Sets versus the natural slope height for models in (a) Subgroup 1, 11, and 41, (b) Subgroup 2, 16, and 46. (c) Subgroup 3, 21, and 51 , (d) Subgroup 4, 26, and 56, (e) Subgroup 5, 31, and 61, (f) Subgroup 6, 36, and 66 (continued)

4.4.3 Recommendation for the Safe Maximum Train Speed

Table 4.21 presents the maximum safe train speeds given various geometries of the slopes and the embankments as well as different rising water level ratios.

Table 4.21 The relationship between the maximum train speed and slope's geometry and the rising water level condition

Slope ratio	Embankment height (H_e) (m)	Rising water level (L/H)	Maximum train speed (km/h) Natural slope height (H_s) (m)					mph (miles/h) Natural slope height (H_s) (m)				
			1	2	3	4	5	1	2	3	4	5
1V:2H	1	0.2	\	\	\	\	\	\	\	\	\	\
		0.4	\	\	\	\	\	\	\	\	\	\
		0.6	\	\	\	\	\	\	\	\	\	\
		0.8	\	\	\	\	\	\	\	\	\	\
		1.0	\	\	\	\	\	\	\	\	\	\
	2	0.2	\	\	\	\	\	\	\	\	\	\
		0.4	\	\	\	\	\	\	\	\	\	\
		0.6	\	\	\	\	\	\	\	\	\	\
		0.8	\	\	\	\	\	\	\	\	\	\
		1.0	\	\	\	\	\	\	\	\	\	\
	3	0.2	40	40	32	32	32	25	25	20	20	20
		0.4	40	32	32	16	16	25	20	20	10	10
		0.6	32	32	24	16	8	20	20	15	10	5
		0.8	24	24	16	8	8	15	15	10	15	5
		1.0	24	16	8	8	8	15	10	5	5	5
1V:3H	1	0.2	8	8	0	\	\	5	5	0	\	\
		0.4	8	8	0	\	\	5	5	0	\	\
		0.6	8	0	\	\	\	5	0	\	\	\
		0.8	0	0	\	\	\	0	0	\	\	\
		1.0	0	\	\	\	\	0	\	\	\	\
	2	0.2	40	40	32	24	24	25	25	20	15	15
		0.4	40	32	24	24	16	25	20	15	15	10
		0.6	32	24	24	16	16	20	15	15	10	10
		0.8	24	24	16	16	8	15	15	10	10	5
		1.0	24	16	16	8	8	15	10	10	5	5
	3	0.2	88	88	80	72	72	55	55	50	45	45
		0.4	88	80	80	72	64	55	50	50	45	40
		0.6	80	72	72	64	56	50	45	45	40	35
		0.8	72	72	64	64	56	45	45	40	40	35
		1.0	72	64	64	56	48	45	40	40	35	30

Figure 4.34 visualizes the maximum safe train speed for all the cases listed in Table 4.21. It should be noted that a color with a negative value (-8 km/h) represents a train that does not have a safe maximum speed meaning that the slope is unable to support even a stationary train.

Based on Table 4.21 and Figure 4.34, the relationship between the maximum safe train speed and the geometry of the slope and the embankment as well as rising water level ratio is analyzed as follow:

- In Figure 4.34 (a) and (b), all grayscales are negative, which indicates that when the slope ratio is 1V:2H, H_e=1m, and 2m, the model is unsafe and cannot support external loads.
- In Figure 4.34 (c), with H_e increased to 3m, the maximum safe speed ranges from 8 km/h (5mph) to 40 km/h (25 mph). An increase in the height of the natural slope and in the rising water level ratio results in a reduction of the safe train speed.
- By contrast, when the slope ratio is set to 1V:3H and the embankment height (H_e) is 1m, the models can support a train under specific conditions, as shown in Figure 4.34 (d). When the rising water level ratio ranges from 0.2 to 0.6, the train can slowly go through the track at 8 km/h (5 mph) if the natural slope height is 1m.
- When H_e=2m, as presented in Figure 4.34 (e), all the conditions are almost the same as Figure 4.34 (c) (H_e=3m, 1V:2H), indicating that the slope is stable enough to support a train traveling at a maximum safe speed of 40 km/h (25 mph).
- The model with a 1V:3H slope ratio and 3m-high railway embankment (H_e=3m) results in the highest maximum safe speed, as shown in Figure 4.34 (f). The maximum safe speed reaches 88km/h (55 mph) when the rising water level ratio ranging from 0.2 to 0.4, and the natural slope height is 1m.

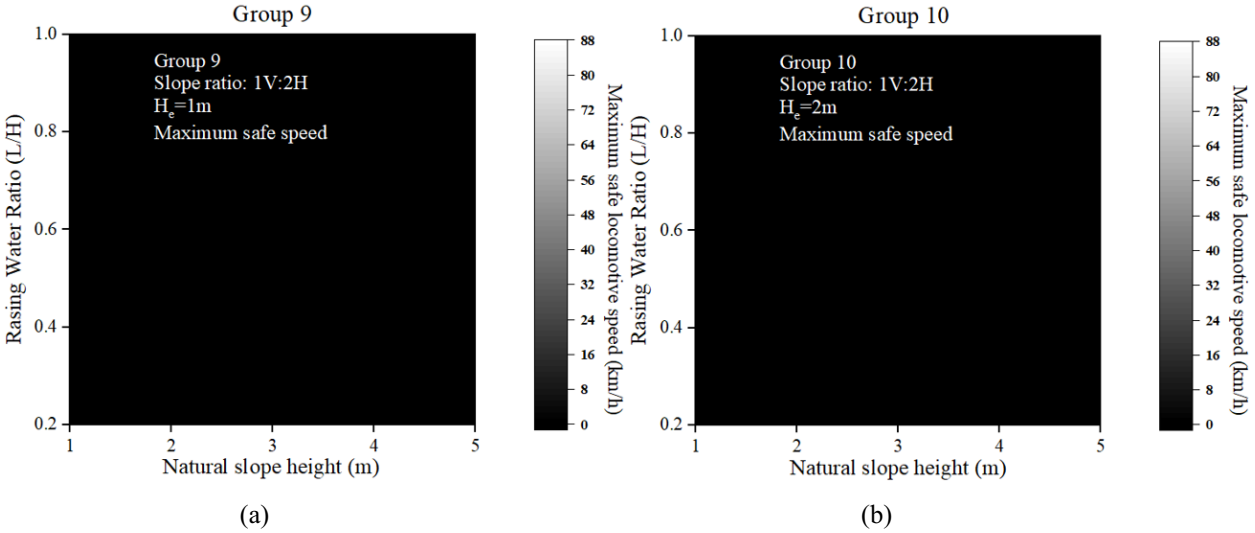

(a) (b)

Figure 4.34 Pseudo color graphs of maximum safe train speed for cases listed in Table 4.7. (a)1V:2H, H_e=1 m, (b) 1V:2H, H_e=2 m, (c) 1V:2H, H_e=3 m, (d) 1V:3H, H_e=1 m, (e) 1V:3H, H_e=2 m, (f) 1V:2H, H_e=3 m

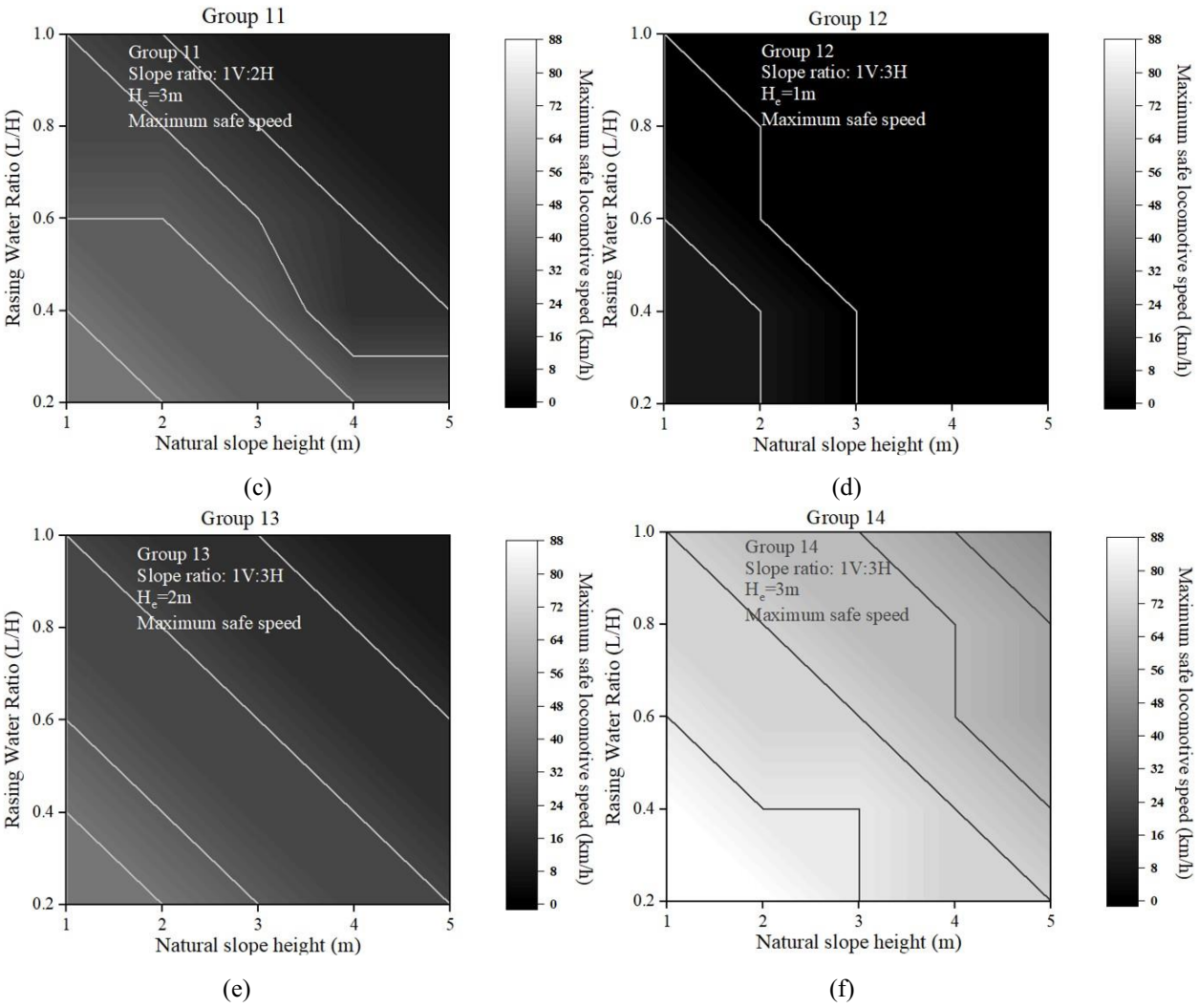

Figure 4.34 Pseudo color graphs of maximum safe train speed for cases listed in Table 4.7. (a)1V:2H, H_e=1 m, (b) 1V:2H, H_e=2 m, (c) 1V:2H, H_e=3 m, (d) 1V:3H, H_e=1 m, (e) 1V:3H, H_e=2 m, (f) 1V:2H, H_e=3 m (continued)

To achieve a maximum safe train speed, it is recommended to construct an embankment with a 1V:3H slope, a 1m-high natural slope, and a 3m-high embankment. According to the analysis, such an embankment can support a train running at a speed ranging from 72km/h (45mph) to 88km/h (55mph) even when the water level rises.

Given the geometrical parameters of the slope and railway embankment as well as the rising water level ratio, the maximum safe train speeds can be quickly identified using Table 4.21, enabling the rail operators to use.

4.5 Summary

In this chapter, the following three Sets of models were developed:

- Set I: models with functioning pipe drains
- Set II: models with rising water levels

- Set III: models with rising water level and train loading

The three sets were developed to study increasingly complex phenomena. The control variable method has been used in this parametric study. The parametric study of Set I and Set II was used to lay a foundation for Set III. The study of Set III begins by looking into the special case where a stationary train is parked on the tracks following which the maximum safe train speed for different embankment geometries and water levels is investigated.

The results of the parametric study indicate that slope stability is maximized by building a flatter slope with a slope ratio of 1V:3H since a smaller slope translates into improved slope stability. As far as the railway embankment is concerned, the analysis indicates that a 3m-high embankment has a greater factor of safety than 1m and 2m-high embankments. Figure 4.28 shows that the maximum safe train speed is greater for a 1V:3H slope that for a 1V:2H slope.

In general, it is recommended to build a 3m-high embankment with a 1V:3H slope and a 1m-high natural slope to obtain a higher FS and a greater maximum safe train speed. Additionally, this study demonstrates that compromised drainage conditions leading to rising water levels can significantly decrease the factor of safety even if optimal geometrical parameters are selected. Also, a table is developed to easily identify problematic scenarios, enabling railways to act more rapidly.

Chapter 5 Conclusion and Future Work

5.1 Introduction

This chapter summarizes the main findings and contributions of this research endeavor and outlines possible future research avenues related to this study. This chapter is composed of four sections:

- Section 5.2: review of the project's objectives and methodology
- Section 5.3: concluding remarks about the analysis and the simulation results
- Section 5.4 and 5.5: overview of the limitations of this research work and suggestions for future work

5.2 Thesis Summary

The aim of this thesis is to identify the factors affecting the stability of railway embankments subjected to unusual groundwater conditions caused by inadequate drainage by developing two-dimensional FEM models. Chapter 2 consists of a literature review that provides detailed information on the common railway embankment construction practices, including the geometrical parameters considered in the parametric study, as well as on the numerical methods used in geomechanics. Chapter 3 describes how the three model sets are developed and presents the results of the mesh converge study and model validation that are performed to validate the accuracy of the FE models used in this study. Finally, Chapter 4 discusses the results of the parametric study and identifies the individual effect of every parameter on the slope stability of railway embankments. The control variable method is used in the parametric study. In this thesis, models are developed to evaluate the influence of compromised drainage on the stability of a railway embankment subjected to either stationary or moving train loading. Additionally, the relationship between the geometry of the railway embankment and the maximum safe train speed is established and is considered critical when inadequate drainage occurs.

5.3 Conclusion

This thesis aims to determine the maximum train speed for a given set of parameters (slope geometry and rising water level conditions). The main findings of the analysis are summarized as follows:

- A flatter slope is safer: A slope with a slope ratio of 1V:3H is inherently more stable than a 1V:2H slope. Therefore, a larger slope ratio is an efficient way of improving slope stability.
- A smaller natural slope height is safer: A 1m-high natural slope has a larger factor of safety and can support trains traveling at a greater maximum speed.
- Optimum railway embankment height: Slope stability decreases when the height of the railway embankment increases for both the dry and rising water level conditions. When the slope is exposed to compromised drainage and train loading, a 3m-high

embankment resulted in a greater factor of safety and maximum safe train speed. Thus, an optimum railway embankment height may exist in each model.

- Compromised drainage leading to a rising water level can dramatically weaken slope stability and reduce the maximum safe train speed.

5.4 Limitations

While important parameters are considered in this research work, one must bear in mind the following limitations:

- Train loads are calculated using a simplified procedure. The railway tracks are assumed to be a smooth straight line with an ideal contact. This may not adequately represent curved tracks which generated centrifugal forces on the rail that translate into unequal forces acting on the two rails.
- Environmental factors (e.g., wind) are not taken into account. According to Indraratna et al. (2011), environmental factors affect the friction between the wheel and the rail, rendering the calculation of the train load more complicated.
- The natural ground is assumed to be a homogeneous sandy clay. However, in real world conditions, the natural ground may consist of multiple soil layers, specific to a geographic location.

5.5 Future Work

Suggestions for future research work in the area include:

- Consider practical track conditions (curved, uneven track) when calculating the train load to model more realistic situations.
- Consider environmental factors.

References

1. Abramson, L. W., T. S. Lee, S. Sharma, and G. M. Boyce. 2001. *Slope Stability and Stabilization Methods*. Hoboken, USA: John Wiley & Sons.
2. Albers, B., S. A. Savidis, H. E. Taşan, O. von Estorff, and M. Gehlken. 2012. "BEM and FEM Results of Displacements in a Poroelastic Column." *International Journal of Applied Mathematics and Computer Science*. 22(4): 883-896. http://dx.doi.org/10.2478/v10006-012-0065-y.
3. American Railway Engineering and Maintenance-of-Way Association (AREMA). 2010. *AREMA Manual for Railway Engineering*. Landover, USA.
4. American Railway Engineering and Maintenance-of-Way Association (AREMA). 2013. *AREMA Manual for Railway Engineering*. Landover, USA.
5. Atalla, N., R. Panneton, and P. Deberque. 1997. "A Mixed Displacement-Pressure Formulation for Poroelastic Materials." *Journal of Acoustical Society of America*. 104: 1444-1452. http://dx.doi.org/10.1121/1.424355.
6. Baqersad, M., A. E. Haghighat, M. Rowshanzamir, and H. M. Bak. 2016. "Comparison of Coupled and Uncoupled Consolidation Equations Using Finite Element Method in Plane-Strain Condition." *Civil Engineering Journal*. 2(8): 375-388. http://dx.doi.org/10.28991/cej-2016-00000042.
7. Bear, J. 2012. *Hydraulics of Groundwater*. New York, USA: Courier Corporation.
8. Bertram, A., and R. Gluge. 2013. *Solid mechanics: Theory, Modeling, and Problems.* Switzerland: Springer.
9. Biot, M. A. 1941. "General Theory of Three-Dimensional Consolidation." *Journal of Applied Physics*. 12(2): 155-164. https://doi.org/10.1063/1.1712886.
10. Bishop, A. W. 1955. "The Use of The Slip Circle in the Stability Analysis of Earth Slope." *Geotechnique*. 5(1): 7-17. https://doi.org/10.1680/geot.1955.5.1.7.
11. Bobet, A. 2010. "Numerical Methods in Geomechanics." *The Arabian Journal for Science and Engineering*. 35(1B): 27-48.
12. Budhu, M. 2010. *Soil Mechanics and Foundations*. Hoboken, USA: John Wiley & Sons Inc.
13. Calamak, M., and A. Yanmaz. 2016. "Seepage Characteristics in Embankments Subject to Variable Water Storages on Both Sides." *Proc., 4th IAHR Europe Congress*. 551-556. http://dx.doi.org/10.13140/RG.2.1.3944.2168.
14. Cedergren, H.R. 1989. *Seepage, Drainage and Flow Nets*. New York, USA: John Wiley and Sons.
15. Chakeri, H., and B. Ünver. 2014. "A New Equation for Estimating the Maximum Surface Settlement above Tunnels Excavated in Soft Ground." *Environmental Earth Sciences*.71(7): 3195-3210. http://dx.doi.org/10.1007/s12665-013-2707-2.
16. Chen, R. and J. Chameau. 1983. "Three-dimensional Limit Equilibrium Analysis of Slopes." *Geotechnique*. 32(1): 31-40. https://doi.org/10.1680/geot.1983.33.1.31.

17. Chen, W.F., and Mizuno, E. 1990. *Nonlinear Analysis in Soil Mechanics*. Amsterdam, Netherlands: Elsevier.

18. Cheng, Y. M., T. Lansivaara, and W. B. Wei. 2007. "Two-dimensional Slope Stability Analysis by Limit Equilibrium and Strength Reduction Methods." *Computers and Geotechnics*. 34(3): 137-150. https://doi.org/10.1016/j.compgeo.2006.10.011.

19. Cheng, Y., and C. Lau. 2014. *Slope Stability Analysis and Stabilization: New Methods and Insight*. London, UK: CRC Press.

20. Clough, R. W. 1960. "The Finite Element Method in Plane Stress Analysis." *2nd ASCE Conference on Electronic Computation*. 345-378.

21. Collins, B. D., and D. Znidarcic. 2004. "Stability Analyses of Rainfall Induced Landslides." *Journal of Geotechnical and Geoenvironmental Engineering*. 130(4): 362-372. http://dx.doi.org/10.1061/(ASCE)1090-0241(2004)130:4(362).

22. Cook, R. D. 2007. *Concepts and Applications of Finite Element Analysis*. Hoboken, USA: John Wiley & Sons.

23. Costabel, M. 1987. "Principles of Boundary Element Methods." *Computer Physics Reports*. 6(1-6): 243-274. https://doi.org/10.1016/0167-7977(87)90014-1.

24. Cundall, P. A., and O. D. Strack. 1979. "A Discrete Numerical Model for Granular Assemblies." *Geotechnique*. 29(1): 47-65. https://doi.org/10.1680/geot.1979.29.1.47.

25. Cundall, P. A., and R. D. Hart. (1992). "Numerical Modelling of Discontinua." *Engineering Computations*. 9(2): 101-113. https://doi.org/10.1108/eb023851.

26. Dawson, E., W. Roth, and A. Drescher. 1999. "Slope Stability Analysis by Strength Reduction." *Geotechnique*. 49(6): 835-840. https://doi.org/10.1680/geot.1999.49.6.835

27. Desai, C. S., and J. T. Christian. 1979. *Numerical Methods in Geotechnical Engineering*. New York, USA: McGraw-Hill.

28. Dick, S. M., D. E. Otter, and R. J. Connor. 2011. "Comparison of Railcar and Bridge Design Loadings for Development of a Railroad Bridge Fatigue Loading." *AREMA 2011 Annual Conference*.

29. Donald, I., and S. Giam. 1988. "Application of the Nodal Displacement Method to Slope Stability Analysis." *Australia-New Zealand Conference on Geomechanics*. 22-23.

30. Duncan, J. M. 1996. "State of the Art: Limit Equilibrium and Finite-Element Analysis of Slopes." *Journal of Geotechnical Engineering*. 122(7): 577-596. https://doi.org/10.1061/(ASCE)0733-9410(1996)122:7(577).

31. Duncan, J. M., and P. Dunlop. 1969. "Slopes in Stiff-Fissured Clays and Shales." *Journal of the Soil Mechanics and Foundations Division*. 95(2): 467-492. https://doi.org/10.1061/JSFEAQ.0001261.

32. Duncan, J. M., S. G. Wright, and T. L. Brandon. 2014. *Soil Strength and Slope Stability*. New York, USA: John Wiley & Sons.

33. Egeli, I., H. Usun. 2012. "Designing High-Speed Train Railway Embankments Using Finite Element Analysis." *Arabian Journal for Science and Engineering*. 37(8): 2127–2136. https://doi.org/10.1007/s13369-012-0302-6.

34. Ercelebi, S. G., H. Copur, and I. Ocak. 2011. "Surface Settlement Predictions for Istanbul Metro Tunnels Excavated by EPB-TBM." *Environmental Earth Sciences*. 62(2): 357-365. http://dx.doi.org/10.1007/s12665-010-0530-6.

35. Esveld, C. 2001. *Modern Railway Track*. Zaltbommel, Netherlands: MRT-Productions.

36. Farias, M., and D. J. Naylor. 1998. "Safety Analysis Using Finite Elements." *Computers and Geotechnics*. 22(2): 165-181. https://doi.org/10.1016/S0266-352X(98)00005-6.

37. Fellenius, W. 1922. "Statens Jarnvagars Geotekniska Kommission: Slutbetankande." *Tech. Rep*.

38. Fellenius, W. 1927. *Erdstatish Berechnungen Mit Reibung und Kohäsion*. Berlin, Germany: W. Ernst & Sohn.

39. Fredlund, D. G., and J. Krahn. 1977. "Comparison of Slope Stability Methods of Analysis." *Canadian Geotechnical Journal*. 14(3): 429-439. https://doi.org/10.1139/t77-045.

40. Gitirana Jr., G.D.F.N. 2005. "Weather-Related Geo-Hazard Assessment Model for Railway Embankment Stability." Ph.D. thesis, Dept. of Civil and Geological Engineering, University of Saskatchewan.

41. Griffiths, D. V. 1994. *Coupled Analyses in Geomechanics*. New York, USA: Springer.

42. Griffiths, D. V., and P. Lane. 1999. "Slope Stability Analysis by Finite Elements." *Geotechnique*. 49(3), 387-403. https://doi.org/10.1680/geot.1999.49.3.387.

43. Hall, W. S. 1994. *Boundary Element Method*. Dordrecht, Netherlands: Springer Science & Business Media.

44. Hammah, R. E., T. E. Yacoub, and J. H. Curran. 2007b. "Serviceability-Based Slope Factor of Safety Using the Shear Strength Reduction (SSR) Method." *11th ISRM Cong., International Society for Rock Mechanics*.1137-1140.

45. Hammah, R. E., T. E. Yacoub, B. Corkum, and J. H. Curran. 2005a. "A Comparison of Finite Element Slope Stability Analysis with Conventional Limit-Equilibrium Investigation." *The 58th Canadian Geotechnical and 6th Joint IAH-CNC and CGS Groundwater Specialty Conferences–GeoSask 2005*.

46. Hammah, R. E., T. E. Yacoub, B. Corkum, and J. H. Curran. 2005b. "The Shear Strength Reduction Method for the Generalized Hoek-Brown Criterion." *Alaska Rocks 2005, The 40th US Symposium on Rock Mechanics (USRMS)*. (1): 234-239.

47. Hammah, R. E., T. E. Yacoub, B. Corkum, and J. H. Curran. 2007a. "Analysis of Blocky Rock Slopes with Finite Element Shear Strength Reduction Analysis." *1st Canada-US Rock Mechanics Symposium*. 329-334.

48. Hoek, E. 2007. "Practical Rock Engineering." Accessed April 2, 2020. https://www.rocscience.com/assets/resources/learning/hoek/Practical-Rock-Engineering-Full-Text.pdf.

49. Indraratna, B., W. Salim, and C. Rujikiatkamjorn. 2011. *Advanced Rail Geotechnology Ballasted Track*. London, UK: CRC Press.

50. Janbu, N. 1954. "Application of Composite Slip Surface for Stability Analysis" *European Conference on Stability of Earth Slopes*. (3): 43-49.

51. Jiang, H., X. Bian, J. Jiang, and Y. Chen. 2016. "Dynamic Performance of High-Speed Railway Formation with the Rise of Water Table." *Engineering Geology*. 206: 18-32. https://doi.org/10.1016/j.enggeo.2016.03.002.

52. Johansson, A. 2006. "Out-of-Round Railway Wheels—Assessment of Wheel Tread Irregularities in Train Traffic." *Journal of Sound and Vibration*. 293(3): 795-806. http://dx.doi.org/10.1016/j.jsv.2005.08.048.

53. Kainthola, A., D. Verma, R. Thareja, and T. N. Singh. 2013. "A Review on Numerical Slope Stability Analysis." *International Journal of Science, Engineering and Technology Research (IJSETR)*. 2(6): 1315-1320.

54. Kitano, T., S. Fujita, H. Ogura, and A. Suganuma. 2017. "Numerical Studies of the Effect of Slope Failure on a Buried Pipeline by a Hybrid Analysis Using SPH and FEM." *16th World Conference on Earthquake*. 614.

55. Krahn, J. 2003. "The 2001 RM Hardy Lecture: The Limits of Limit Equilibrium Analyses." *Canadian Geotechnical Journal*. 40(3): 643-660. https://doi.org/10.1139/t03-024.

56. Lam, L., D. Fredlund, and S. Barbour. 1987. "Transient Seepage Model for Saturated–Unsaturated Soil Systems: A Geotechnical Engineering Approach." *Canadian Geotechnical Journal*. 24(4): 565-580. https://doi.org/10.1139/t87-071.

57. Li, D., J. Hyslip, T. Sussmann, and S. Chrismer. 2002. *Railway Geotechnic.* London, UK: CRC Press.

58. Li, D., J. P. Hyslip, T. R. Sussmann, and S. M. Chrismer. 2016. *Railway Geotechnics*. London, UK: Taylor & Francis Group.

59. Li, G. C., and C. S. Desai. 1983. "Stress and Seepage Analysis of Earth Dams." *Journal of Geotechnical Engineering*. 109(7): 946-960. https://doi.org/10.1061/(ASCE)0733-9410(1983)109:7(946).

60. Li, G. X. 2004. *Advanced Soil Mechanics*. Beijing, China: Tsinghua University Press.

61. Lichtberger, B. 2005. *Track Compendium: Formation, Permanent Way, Maintenance*. Berlin, German: Economics.

62. Matsui, T., and K. C. San. 1988. "Finite Element Stability Analysis Method for Reinforced Slope Cutting." *International Geotechnical Symposium on Theory and Practice of Earth Reinforcement*. 317-322. http://worldcat.org/isbn/9061918200.

63. Matsui, T., and K. C. San. 1992. "Finite Element Slope Stability Analysis by Shear Strength Reduction Technique." *Soils and Foundations*. 32(1): 59-70. https://doi.org/10.3208/sandf1972.32.59.

64. Matthews, C., Z. Farook, and P, Helm. 2014. "Slope Stability Analysis–Limit Equilibrium or the Finite Element Method." *Ground Engineering.* 48(5), 22-28.

65. Morgenstern, N. U., and V. E. Price. 1965. "The Analysis of the Stability of General Slip Surfaces." *Geotechnique*. 15(1): 79-93. https://doi.org/10.1680/geot.1965.15.1.79.

66. Munjiza, A. 2004. *The Combined Finite-Discrete Element Method*. London, UK: John Wiley & Sons.

67. Naylor, D. J. 1982. *Finite Elements and Slope Stability*. New York, USA: Springer.

68. Nikolić, M., T. Roje-Bonacci, and A. Ibrahimbegović. 2016. "Overview of the Numerical Methods for the Modelling of Rock Mechanics Problems." *Tehnicki vjesnik/Technical Gazette.* 23(2): 627-637. https://doi.org/10.17559/TV-20140521084228.

69. Palin, E. J., I. Stipanovic Oslakovic, K. Gavin, and A. Quinn. 2021. "Implications of Climate Change for Railway Infrastructure." *Wiley Interdisciplinary Reviews: Climate Change*. 12(5): e728. https://doi.org/10.1002/wcc.728.

70. Pietruszczak, S. 2010. *Fundamentals of Plasticity in Geomechanics.* Boca Raton, USA: CRC Press.

71. Pinyol, N. M., E. E. Alonso, and S. Olivella. 2008. "Rapid Drawdown in Slopes and Embankments." *Water Resources Research*. 44(5). http://dx.doi.org/10.1029/2007WR006525.

72. Potts, D. M., and L. Zdravković. 1999. *Finite Element Analysis in Geotechnical Engineering: Theory*. London, UK: Thomas Telford.

73. Profillidis, V. A. 2014. *Railway Management and Engineering.* Burlington, USA: Ashgate Publishing Company.

74. Punmia, B. C., A. K. Jain. 2005. *Soil Mechanics and Foundations*. New Delhi, India: Laxmi Publications.

75. Putu Tantri, K. S., and Y. Lastiasih. 2015. "Slope Stability Evaluation Using Limit Equilibrium Method (LEM) and Finite Element Method (FEM) for Indonesia Soft Soil." *The 3rd Bali International Seminar on Science and Technology (BISSTECH)*. (1).

76. Read, D. and D. Li. 1995. *Subballast Considerations for Heavy Axle Load Trackage*. Pueblo: USA: Transportation Technology Center.

77. Rendulic, L. 1936. "Porenziffer und Porenwasserdruck in Tonen." *Der Bauingenieur*. 17: 559-564.

78. Rocscience Inc. 2019. "Convergence Criteria." Accessed December 20, 2019. https://www.rocscience.com/help/rs2/pdf_files/theory/Convergence_Criteria.pdf.

79. Rowe, R. K. 2012. *Geotechnical and Geoenvironmental Engineering Handbook*. Berlin, Germany: Springer Science & Business Media.

80. Sadeghi, J., and P. Barati. 2010. "Evaluation of Conventional Methods in Analysis and Design of Railway Track System." *International Journal of Civil Engineering*. 8(1): 44-56.

81. Sazzad, M. M., F. I.Rahman, and M. A. Mamun. 2016. "Effects of Water Level Variation on the Stability of Slope by LEM and FEM." *3rd International Conference on Civil Engineering for Sustainable Development (ICCESD 2016).* 953-959.

82. Selig g, E. T., and J. M. Waters. 1994. *Track Geotechnology and Substructure Management*. London, UK: Thomas Telford.

83. Smith, I. M., D. V. Griffiths, and L. Margetts. 2013. *Programming the Finite Element Method*. Chichester, UK: John Wiley & Sons.

84. Snitbhan, N., and W. F. Chen. 1976. "Elastic-Plastic Large Deformation Analysis of Soil Slopes." *Computers & Structures*. 9(6): 567-577. https://doi.org/10.1016/0045-7949(78)90006-8.

85. Song, E. 1997. “Finite Element Analysis of Safety Factor for Soil Structures.” *Chi. J. Geotech. Eng.* 19(2):1-7. https://doi.org/10.6052/j.issn.1000-4750.2014.12.1024.

86. Spencer, E. 1967. “A Method of Analysis of the Stability of Embankments Assuming Parallel Inter-Slice Forces.” *Geotechnique*. 17(1): 11-26. https://doi.org/10.1680/geot.1967.17.1.11.

87. Terzaghi, K. 1925. “Principles of Soil Mechanics, IV—Settlement and Consolidation of Clay.” *Engineering News-Record*. 95(3): 874-878.

88. Terzaghi, K. 1951. *Theoretical Soil Mechanics*. London, UK: Chapman and Hall.

89. Timoshenko, S. P., and J. N. Goodier. 1982. *Theory of Elasticity*. New York, USA: McGraw-Hill.

90. Transport Canada. 2018. “Transportation in Canada 2018.” Accessed December 21, 2019. https://tc.canada.ca/sites/default/files/migrated/transportation_in_canada_2018.pdf.

91. Transport Canada. 2019. "Transportation in Canada 2019." Accessed December 21, 2019. https://tc.canada.ca/en/corporate-services/transparency/corporate-management-reporting/transportation-canada-annual-reports/transportation-canada-2019.

92. Transportation Safety Board (TSB) (2013). “Railway Investigation Report.” Rep. No. R13W0124, Togo, Saskatchewan, Canada.

93. Ugai, K., and D. O. V. Leshchinsky. 1995. “Three-Dimensional Limit Equilibrium and Finite Element Analyses: A Comparison of Results.” *Soils and Foundations*. 35(4): 1-7. https://doi.org/10.3208/sandf.35.4_1.

94. Wong, R., P. Thomson, and E. Choi. 2006. “In Situ Pore Pressure Responses of Native Peat and Soil under Train Load: A Case Study.” *Journal of Geotechnical and Geoenvironmental Engineering.* 132(10): 360-1369. https://doi.org/10.1061/(ASCE)1090-0241(2006)132:10(1360).

95. Wright, S. G., F. H. Kulhawy, and J. M. Duncan. 1973. “Accuracy of Equilibrium Slope Stability Analysis.” *Journal of the Soil Mechanics and Foundations Division*. 99(10): 783-791. https://doi.org/10.1061/JSFEAQ.0001933.

96. Xie, X., Y. Yang, and M. Ji. 2016. “Analysis of Ground Surface Settlement Induced by the Construction of a Large-Diameter Shield-Driven Tunnel in Shanghai, China.” *Tunneling and Underground Space Technology*. (51): 120-132. http://dx.doi.org/10.1016/j.tust.2015.10.008.

97. Xu, S., and A. M. Zsáki. 2021. “Maximum Safe Freight Train Speed on Railway Embankments under Rapid Drawdown Conditions Based on Coupled Stress-Seepage Slope Stability Analysis.” *Transportation Geotechnics*. (27): 100486. https://doi.org/10.1016/j.trgeo.2020.100486.

98. Zhang, H.J., Q. Gong, and H. G. Di. 2014. “Numerical Analysis of Shield Tunnel Driving underneath an Existing Railway and Related Reinforcement Effects on Subsidence Control.” *International Conference on Pipelines and Trenchless Technology 2014*. 828-835. http://dx.doi.org/10.1061/9780784413821.089.

99. Zhang, T. W., Y. J. Cui, F. Lamas-Lopez, N. Calon, and S. C. D’Aguiar. 2016. “Modelling Stress Distribution in Substructure of French Conventional Railway Tracks.” *Construction and Building Materials*. 116: 326-334. https://doi.org/10.1016/j.conbuildmat.2016.04.137.

100. Zheng, Y. R., S. Y. Zhao, W. X. Kong, and C. J. Deng. 2005. "Geotechnical Engineering Limit Analysis Using Finite Element Method." *Yantu Lixue (Rock Soil Mech*). 26(1): 163-168.

101. Zienkiewicz, O. C., C. Humpheson, and R. W. Lewis. 1975. "Associated and Non-Associated Visco-Plasticity in Soils Mechanics." *Geotechnique*. 25(5): 671-689. https://doi.org/10.1680/geot.1975.25.4.671.

102. Zienkiewicz, O. C., R. L. Taylor, P. Nithiarasu, and J. Zhu. 1977. *The Finite Element Method*. London, UK: McGraw-Hill.

103. Zienkiewicz, O.C. and T. Shiomi. 1984. "Dynamic Behaviour of Saturated Porous Media; The Generalized Biot Formulation and its Numerical Solution." *International Journal for Numerical and Analytical Methods in Geomechanics*. 8: 71-96. https://doi.org/10.1002/nag.1610080106.